

ALMA MATER STUDIORUM · UNIVERSITÀ DI BOLOGNA

---

Scuola di Scienze  
Dipartimento di Fisica e Astronomia  
Corso di Laurea Magistrale in Fisica

**The  $^{16}\text{O}+^{12}\text{C}$  reaction at 90.5, 110 and 130  
MeV beam energy**

**Relatore:**  
Prof. Mauro Bruno

**Presentata da:**  
Catalin Frosin

**Correlatore:**  
Dott. Luca Morelli

**Sessione III**  
**Anno Accademico 2015/2016**



# Contents

<b>Abstract</b>	<b>1</b>
<b>Introduction</b>	<b>3</b>
<b>1 The Physics Case</b>	<b>4</b>
1.1 Introduction to Heavy Ion Collisions . . . . .	4
1.1.1 Peripheral and Direct Reaction . . . . .	6
1.1.2 Central Collisions and Compound Nucleus . . . . .	7
1.2 Statistical Decay . . . . .	11
1.3 Structure and Clustering Effects . . . . .	14
1.3.1 The $^{16}\text{O}$ nucleus . . . . .	17
1.4 The $^{16}\text{O}+^{12}\text{C}$ Reaction . . . . .	17
<b>2 The Experimental Apparatus</b>	<b>20</b>
2.1 GARFIELD Apparatus . . . . .	20
2.1.1 Drift Chamber and Microstrip . . . . .	23
2.1.2 CsI(Tl) Crystals . . . . .	24
2.2 Ring Counter . . . . .	26
2.3 Electronics . . . . .	28
2.3.1 Triggers and Acquisition . . . . .	29
<b>3 The Experimental Measurement and Energy Calibration</b>	<b>32</b>
3.1 The Measurement . . . . .	32
3.2 Data Reconstruction and Particle Identification Methods . . . . .	35
3.2.1 $\Delta E-E$ . . . . .	35
3.2.2 Pulse Shape Analysis . . . . .	37
3.2.3 Energy vs Rise-Time . . . . .	38
3.2.4 Identification Procedures . . . . .	39
3.3 Energy Calibration . . . . .	43
3.4 Experimental Observables and Data Reduction . . . . .	46

<b>4</b>	<b>The Hauser-Feshbach Statistical Decay Code</b>	<b>49</b>
4.1	Monte-Carlo Implementation of the Decay Model . . . . .	49
4.2	The Level Density Model . . . . .	51
4.3	Treatment of the Angular Momentum . . . . .	54
4.4	Correlation Function . . . . .	55
<b>5</b>	<b>Data Analysis and Results</b>	<b>58</b>
5.1	Quasi-Complete Charge Detection Condition . . . . .	60
5.1.1	Charge Distribution and Multiplicities . . . . .	61
5.1.2	Angular and Energy Distributions . . . . .	62
5.1.3	Complete Charge Detection Condition . . . . .	64
5.2	Evaporation Residue Selection . . . . .	67
5.2.1	Energy Distributions . . . . .	68
5.2.2	Angular Distributions . . . . .	73
5.3	Excitation Energy Dependence and Clustering Effects . . . . .	75
5.3.1	Branching Ratio . . . . .	76
5.3.2	Q-value Distributions . . . . .	78
5.3.3	Indication of clustering effects . . . . .	82
	<b>Conclusions and Perspectives</b>	<b>87</b>
	<b>Bibliography</b>	<b>91</b>

# Abstract

Questo lavoro di tesi è inserito in uno studio, nell'ambito della collaborazione NUCL-EX, delle collisioni tra ioni pesanti per indagare le proprietà statistiche e la struttura della materia nucleare per sistemi con massa  $A < 40$ . In particolare è stata studiata la reazione  $^{16}\text{O} + ^{12}\text{C}$ , ad energie di fascio di 90.5 MeV, 110 MeV e 130 MeV. Lo scopo della misura è quello di studiare il meccanismo di fusione-evaporazione e le possibili deviazioni da un decadimento puramente statistico del nucleo composto ( $^{28}\text{Si}^*$ ) che si viene a formare. Il confronto tra i dati sperimentali e quelli ottenuti da una previsione basata sul modello statistico Hauser-Feschbach, ottimizzato per lo studio di nuclei leggeri (HF $\ell$ ), è in grado di fornire indicazioni su effetti di struttura come già evidenziato in passato dalla collaborazione in reazioni analoghe. Questi sono principalmente legati nel nostro caso alla possibile struttura a cluster di particelle  $\alpha$  che persistono oltre le soglie di emissione di particella. La misura è stata effettuata presso i Laboratori Nazionali di Legnaro sfruttando il fascio fornito da un acceleratore Tandem XTU e l'apparato sperimentale formato dai rivelatori GARFIELD e Ring Counter (RCo). L'analisi si è concentrata sia sullo studio di osservabili inclusivi come le distribuzioni energetiche e angolari delle particelle emesse che di osservabili esclusivi come la probabilità di decadimento in canali specifici. Questi risultati preliminari ottenuti per la reazione  $^{16}\text{O} + ^{12}\text{C}$  hanno in effetti evidenziato la presenza di effetti di struttura legate all'emissione di cluster- $\alpha$ , in particolare quando il residuo è un nucleo di carica pari. Si discute anche della dipendenza dall'energia incidente, e quindi dall'energia di eccitazione del  $^{28}\text{Si}^*$ , di questi effetti. In conclusione si indicano gli aspetti da investigare con maggior dettaglio per ottenere risultati più consolidati e cercare di definire le cause di queste deviazioni dal modello statistico.

# Introduction

The nuclear force at the nucleon scale is still one of the most active area of research in nuclear physics and many theoretical models have been developed throughout the years trying to reproduce at best the experimental data. In this framework, nuclear reactions with heavy ions are one of the main tools for investigating the structure and features of nuclear matter. They allow to access the excitation spectrum of the nuclei and to study their behavior in extreme conditions (temperature and/or density) far from their ground state. Furthermore, these states are of great interest for nuclear astrophysics studies as for example, stellar nucleosynthesis.

The NUCL-EX [1] collaboration in particular, has focused its attention on the study of the properties of light nuclei with atomic mass  $A < 40$  at low energies (below 20 A MeV). Both statistical decay of hot nuclei and nuclear clustering, as a deviation from the former mechanism, were investigated during the past experimental campaigns. A statistical decay code [2] developed by the collaboration (HF $\ell$ ), especially designed for light nuclei and containing the details of all the excited levels, has been used. The compound nucleus decay for fusion-evaporation reactions can be detailed and at the same time the parameters of the HF $\ell$  can be further constrained. The comparison between the model and experimental data, could evidence nuclear structure effects. Indeed, some excited states of even- $Z$  nuclei in this mass region are known to present pronounced  $\alpha$ -cluster effects even at high excitation energies. In this thesis, we want to study this physics case for the  $^{16}\text{O} + ^{12}\text{C}$  reaction performed at three different beam energies (90.5, 110 and 130 MeV). In the case of complete fusion, this reaction, which employs  $\alpha$ -cluster stable nuclei in the entrance channel, leads to the formation of a  $^{28}\text{Si}^*$  system at respectively 55, 63 and 72 MeV excitation energy. From previous measurements on the decay of excited  $^{24}\text{Mg}$  [3], cluster correlations are expected to persist also in the  $^{28}\text{Si}$  heavier system. Moreover, the three energies can point out how the cluster degree of freedom evolves varying the excitation energy of the system and leading to different decay patterns. In this cases, the observables of the reaction will show deviations from a statistical fusion-evaporation model. For example, one can study both global variables such as energy distributions or more exclusive ones as the Branching Ratio of particular decay channels.

To detect and identify the reaction products the GARFIELD and Ring Counter (RCo) apparatus, described in detail in Chapter 2, were used. The two detectors coupled

---

together cover about 80% of the solid angle allowing to reconstruct on an event by event basis the single decay channels of the fused system when the whole charge of the reaction partners is collected. Both detectors employ the  $\Delta E - E$  method and Pulse Shape Analysis (PSA) for identifying and measuring the energy of the incident particles. The results are then compared to the prediction of a HF $\ell$  Monte-Carlo simulation.

This thesis is organized as follows. In Chapter 1 the general physics case of nuclear reactions will be introduced with particular attention to the complete fusion mechanism. For this type of reaction both the formation and statistical decay model will be described more in detail. In the last section, the cluster degree of freedom is presented along with a brief introduction to the previous results obtained by the NUCL-EX collaboration. Chapter 2 is dedicated to the characterization of the experimental apparatus which was employed for the current measurements, *i.e.* the GARFIELD+RCo detectors. In Chapter 3, we present the details of the reaction measurements and the main identification and calibration techniques for the decay products detected. As mentioned before, the results are compared to the HF $\ell$  Monte-Carlo simulation which is summarised in Chapter 4. A more detailed description can be found in [2]. In Chapter 5 the first preliminary results for this reaction are shown and compared to the statistical model of the previous chapter. The observed deviations from the statistical model will be underlined and discussed in relation to clustering effects. Finally, conclusions and perspectives are drawn.

# Chapter 1

## The Physics Case

Nuclei are finite quantum system and as such, they are characterized by their ground state and their excitation spectrum. The latter can be accessed by means of nuclear reactions. This implies that researches aiming at understanding the physics of excited nuclei heavily rely on the study of the reaction mechanisms themselves. These reactions allow observing the time evolution of the collision from a highly-out-of equilibrium situation (two cold colliding nuclei ) towards a possible thermalized system with high excitation energy and angular momentum. The stronger the nuclear excitation the larger becomes the number of quantum mechanical states which can be explored and consequently more nuclear properties far from the ground state can be studied.

Moreover, heavy ion collision can produce exotic and unstable new species (unusual neutron/proton ratio or superheavy elements) not found in nature, which can be further investigated.

In conclusion, the study of heavy-ion collisions is a powerful tool to investigate the physics of nuclear matter in extreme conditions of temperature and density. In this chapter, we describe the general physics framework related to the experiment described in this thesis, consisting of both a theoretical and an experimental introduction to the study and the decay of light nuclear systems.

### 1.1 Introduction to Heavy Ion Collisions

Heavy ion collisions can be classified according to some global "topological" feature in order to separate and identify the "sources" of the particles emitted and detected. These features are generally the impact parameter of the collision and the kinetic energy associated with the relative motion between the two partners of the collision. The former is defined as the distance between the asymptotic trajectory of the projectile and its parallel line passing through the centre of the target. The latter is the available centre-of-mass kinetic energy, transformed partially or entirely into excitation energy during

the interaction between the two colliding nuclei.

This dissipation process can be better understood by comparing the reduced relative wavelength of the initial partners in the reaction with the mean nucleon-nucleon distance in a nucleus ( $\sim 1.2$  fm). The first parameter is given by:

$$\lambda = \frac{\hbar}{mv_{aa}} \quad (1.1)$$

where  $m$  is the nucleon mass and  $v_{aa}$  is the relative velocity between the projectile and target. If  $\lambda$  exceeds the mean nucleon-nucleon distance, then a collective behaviour of the nucleons during the collision can be assumed. In other words, the interaction between nucleons inside the hot nuclear matter can be described via a mean field potential (one-body interaction). On the other hand, if  $\lambda$  is smaller than 1.2 fm a two body interaction (nucleon-nucleon scattering) is used to explain the dissipation process. Therefore, according to eq. 1.1, the mean field effects prevail in the low-energy domain below 15 MeV/u incident energy, whereas two-body interaction start to become relevant above this value.

The different reaction mechanisms can also be easily classified using the impact parameter "b", or alternatively the angular momentum "l" (Figure 1.1). In fact, in a semiclassical approach they are related by:

$$b = l\lambda \quad (1.2)$$

Unlike the incident energy or the nuclei involved in the reaction, it is not possible to experimentally choose a priori the impact parameter. Estimates of "b" are obtained by measuring variables monotonically correlated with it. An important value of "b" is the one called the "grazing" impact parameter ( $b_{gr}$ ); it represents the minimum value of "b" at which nuclear forces are negligible with respect to Coulomb interaction.

Based on the before-mentioned notions, we can identify four regions of different interaction mechanisms:

- for  $l > l_{gr}$  the projectile and the target nuclei interact only by means of the Coulomb force. Therefore, the main processes are those of elastic or inelastic scattering.
- for  $l_{DIC} < l < l_{gr}$  the kinematics of the two nuclei is just slightly perturbed as the nuclear force starts to grow. In this region (quasi-elastic) only external nucleons can interact while internal ones are not affected. These types of reaction are called *Direct Reactions* and it is possible to have few nucleons transfer between the projectile and the target.
- for  $l_{crit} < l < l_{DIC}$  (*Deep Inelastic Scattering*) the two partners re-separate after a contact phase during which matter, angular momentum and significant amounts of energy are exchanged.

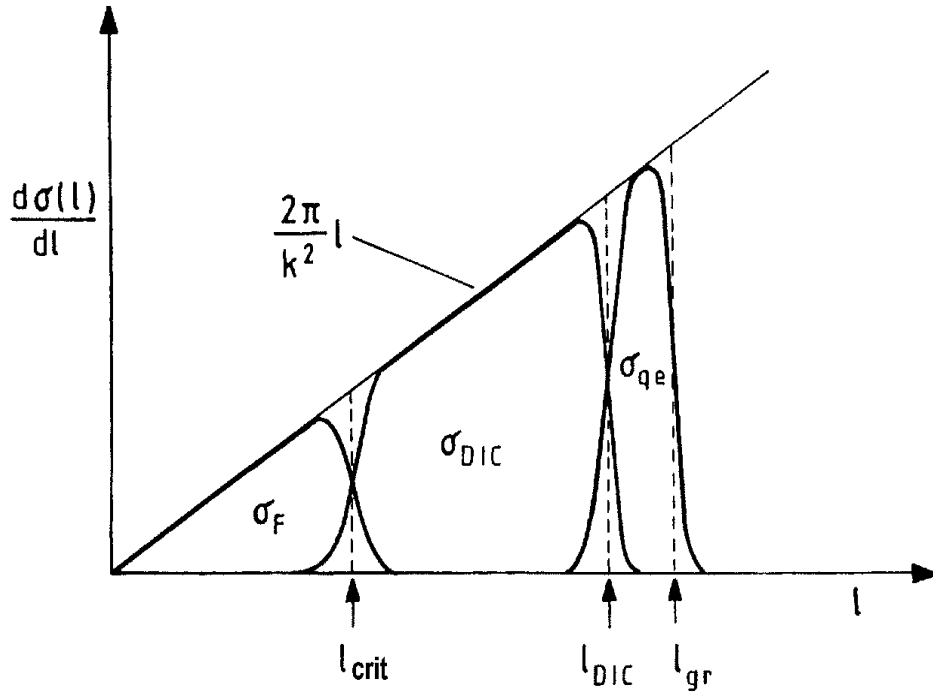


Figure 1.1: Contribution to the differential cross section from the different reaction mechanisms as a function of the angular momentum.

- for  $l < l_{crit}$  we are in the region of central collisions, where the dominant process is the complete fusion of the reaction partners and the formation of a compound nucleus (CN). In Figure 1.1 the contributions of the various mechanisms to the cross section are shown. As it can be easily seen in some region different mechanisms overlap. The line  $\frac{d\sigma(l)}{dl} = \frac{2\pi l}{k^2}$  shows the geometrical cross section.

In the following two subsections, we examine in more depth the various mechanisms and in particular we will focus on the formation of a compound nucleus.

### 1.1.1 Peripheral and Direct Reaction

Above and around the grazing value the main reaction mechanisms are elastic scattering or Direct and DIC collisions. In the first case, there is the possibility of having Coulomb excitation (or *Coulex*). The Coulex mechanism is the transfer of energy to the target nucleus in the electromagnetic field of the projectile or viceversa. The excited nucleus then decays to its ground state by emitting  $\gamma$ -rays or few nucleons if it is excited above particle emission threshold. This process has been used for decades to obtain information related to low lying nuclear states [4, 5].

In the second case, as we recall from the general description of nuclear reactions, a direct reaction occurs if one of the participants in the initial two-body interaction is transferred from one nucleus to the other. Generally speaking, these reactions are divided into two classes, the *stripping reactions* in which part of the incident projectile is transferred to the target nucleus and the *pickup reactions* in which the outgoing projectile-like particle is a combination of the incident nucleus and a few target nucleons. Typical stripping reactions are (d, p), ( $\alpha$ , t) or ( $\alpha$ , d) while common pickup reactions are (p, d), (p, t) and ( $\alpha$ ,  ${}^6\text{Li}$ ).

Going towards less peripheral collisions, the reacting nuclei acquire larger excitations and the nucleon exchange between them becomes more relevant. In fact, in deep elastic scattering, the colliding nuclei partially amalgamate (similar to a di-molecular state), exchange energy and mass and then re-separate under their mutual Coulomb repulsion. Therefore, in the exit channel, one normally detects a quasi-projectile fragment (QP) and a quasi-target (QT) with characteristics (mass and charge) that resemble the ones of the initial reaction partners. For semiperipheral collisions, DIC mechanism starts to compete with the formation of a compound nucleus.

### 1.1.2 Central Collisions and Compound Nucleus

Central collisions usually lead to the fusion of projectile and target nuclei. It is clear from Figure 1.1 that there is a critical angular momentum that separates fusion from the DIC region, even though this transition is not sharp but rather smooth with a small overlap around  $l_{crit}$  between the two distributions. Its value is governed by the interaction potential between the interacting nuclei which consists of several terms:

- the Coulomb term that evolves as the inverse of the relative distance.
- the nuclear force term which is negligible for large distances but becomes attractive when the relative distance is close to the sum of the nuclear radii. This contribution turns gradually into a repulsive force when the densities of the two nuclei significantly overlap.
- the rotational contribution at finite impact parameter. This term is due to the combined effects of the angular momentum and moment of inertia of the system.

In Figure 1.2 an example of the interaction potential evolution as a function of the relative distance is shown. To summarize, for  $l < l_{crit}$  a potential pocket exists which traps the system inside due to the nuclear friction. In contrast, for angular momentum exceeding  $l_{crit}$ , the system is never trapped and the two partners separate after a contact phase thus preventing the formation of a fused nucleus (CN).

The reaction process, in the case of fusion leading to a compound nucleus, can be divided into two steps well separated in time. The first step is the collision stage where

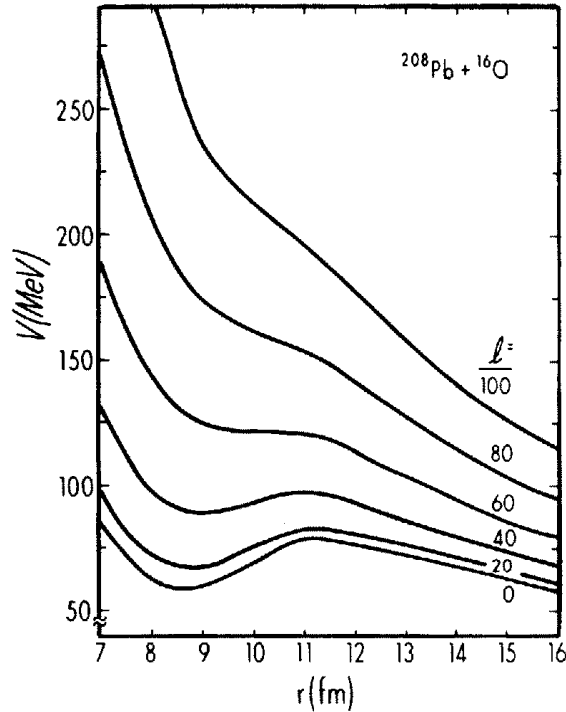


Figure 1.2: The total interaction potential is shown for various values of  $l$ . The critical angular momentum corresponds to the  $l$  for which the pocket of the potential curve disappears [6].

the two nuclei merge and form a fully equilibrated excited nucleus on a time scale (about  $10^{-21}$ s) shorter than the following decay (from  $10^{-19}$  to  $10^{-16}$ s). In fact, once the compound nucleus is created, it forgets the initial dynamics which has led to its formation except for the incident energy and angular momentum. This is called the *Bohr's independence hypothesis* [7] and the cross section for the reaction:



can be written as the product of two independent terms. The first one is the probability of forming the compound nucleus in the entrance channel "i" ( $a+A$ ) while the second is the probability that the CN decays in a given channel "f" ( $b+B$ ), also called the Branching Ratio (BR):

$$\sigma_{i \rightarrow f}^{E, J, \pi(CN)} = \sigma_F^{CN}(i) BR^{CN}(f) \quad (1.4)$$

To estimate the fusion cross section one can use, in a first approximation, a classical picture of the nuclear reaction [8]. In this simple picture, we can adopt the value " $b_F$ " as a cut-off value which will determine if the projectile is absorbed and fused with the

target ( $b < b_F$ ). Therefore, the total absorption cross section is simply given by:

$$\sigma_F = \int_0^{b_F} 2\pi b db = \pi b_F^2 \quad (1.5)$$

Substituting in 1.5 the value of  $b_{gr}$  we find the explicit energy dependence of the fusion cross section:

$$\sigma_F(\epsilon) = \pi R^2 \left(1 - \frac{B}{\epsilon_i}\right) \quad (1.6)$$

where  $R$  and  $B$  are the radius and the corresponding value of the interaction potential barrier, whereas  $\epsilon_i$  is the relative kinetic energy between projectile and target in the centre-of-mass frame. An equivalent expression can be obtained in terms of the orbital angular momentum, given eq. 1.2, where we attribute successive contribution to  $\sigma_F$  to successive values of  $l$ . The cross section for a determined  $l$  can be thought as the area between circles with radii  $b = l\lambda$  and  $b = (l + 1)\lambda$ , as shown in Figure 1.3.

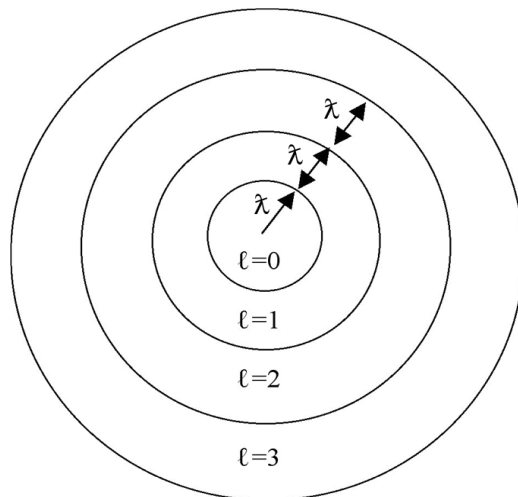


Figure 1.3: The geometrical picture of the cross section for different given  $l$  values.

As a result, the total absorption cross section  $\sigma_F$  can be written in terms of a sum over angular momentum:

$$\sigma_F = \pi\lambda \sum_{l=0}^{l_{crit}} (2l + 1) = \pi\lambda (l_{crit} + 1)^2 \quad (1.7)$$

A more efficient quantum extension of this classical formula for  $\sigma_F$ , can be derived considering that, for some values of  $l$ , there will be finite probabilities for both scattering and absorption from the elastic channel. To account for these probabilities, we define a transmission coefficient  $T_l$  as the probability that a given partial wave  $l$  is absorbed. At

this point, one can write instead of eq. 1.7 the following expression:

$$\sigma_F = \pi\lambda \sum_{l=0}^{l_{crit}} (2l+1)T_l \quad (1.8)$$

where now the simplification of a sharp cut-off, introduced at the beginning, is defined by:

$$T_l = 1 \quad \text{for} \quad l < l_{crit} \quad (1.9)$$

$$T_l = 0 \quad \text{for} \quad l > l_{crit} \quad (1.10)$$

Obviously, this picture is far from being complete since the formation of the CN can also be limited by many other conditions, such as the competition of non-compound processes accompanying fusion in the entrance channel. Nevertheless, eq. 1.8 provides a starting point which is needed in the derivation of the decay widths. Its general form will require additional consideration of the spin degree of freedom in the reaction and of the transmission coefficients  $T_l$ . Further details will be discussed with regard to the Monte-Carlo implementation of the statistical model in chapter 4. In addition, as shown in Figure 1.1 and stressed in the beginning of this section, the transition at  $l_{crit}$  is not sharp and therefore what is generally done is to consider a diffuseness around  $l_{crit}$  ( $b_F$ ), to be taken into account in eq. 1.5, 1.7 and 1.8.

Concluding, we want to specify one last aspect on the compound nucleus formation cross section. The transmission coefficients introduced previously in eq. 1.8 are energy and momentum dependent, and thus related to the probability of creating the CN in a specific (discrete) state "C". As a consequence of this, resonances in the fusion cross section may appear. For a particular case of spinless projectile and target, the resonant CN formation cross section is given by:

$$\sigma_F^C(\epsilon_i) = \pi\lambda^2(2l+1) \frac{\Gamma^i\Gamma}{(\epsilon_i - \epsilon_{iR})^2 + \frac{\Gamma^2}{4}} \quad (1.11)$$

where  $\Gamma$  and  $\Gamma^i$  are the total and the entrance channel "i" decay widths, whereas  $\epsilon_i$  is the relative kinetic energy between the collision partners in the entrance channel.

After the CN formation, the system can decay either via evaporation or fission. For the reaction considered in this thesis ( $^{16}O+^{12}C$ ), the former is the dominant decay process while fission becomes relevant for heavier or highly deformed systems. Evaporation means that the compound nucleus loses its excitation energy by emitting light charged particles (LCP) like p, d, t,  $^3He$ ,  $\alpha$ ,  $^6,7Li$ ,  $^8Be$  and neutrons. The remaining nuclear fragment, at the end of the decay chain, is called an *Evaporation Residue* (ER). The importance of resonances described earlier, in the decay of the CN source, is due to the fact that discrete levels can indeed be populated in daughter nuclei, which can further

decay in products that keep memory of their "resonant" origin. Decaying discrete states can then be reconstructed through particular techniques as correlation function in the relative momentum of coincident measured yields.

From an experimental point of view, the reaction mechanism is well understood if we are able to measure and identify the emitted particles, namely LCP and ER. However, one has to bear in mind that the final inclusive yields represent an integrated contribution over the whole time evolution of the decay chain. Because of that, the information they provide on specific energy regions of the different nuclei explored after the reaction may be model dependent. The challenge for an experimental measurement is to perform highly exclusive and complete detection of the decay products, in order to reconstruct their origin.

## 1.2 Statistical Decay

A compound nuclear system, even at the lowest incident energy at which fusion occurs, can explore many different configurations and decay in many different ways. This complexity is one of the justification for the use of a statistical model to describe the CN decay channels. In Section 1.1.2, we have described central collisions and in particular the formation of a compound nucleus. Hereafter, we will consider its decay and the statistical model used to explain the properties of the particles detected. This model is based on the assumption that all decay channel are equally likely and are governed by factors such as the density of the final state and barrier penetration factors.

The statistical model was first introduced and developed by several authors [7, 9, 10, 11], starting from late '30s. A few years afterwards, Hauser and Feshbach [12] included a more extensive treatment of total angular momentum and this extended model became the foundation of the statistical decay models in use nowadays.

Considering a complete fusion, due to Bohr's hypothesis, one can completely characterize the CN in terms of the charge  $Z_{CN}$ , mass  $A_{CN}$  and excitation energy  $E^*$ . These values are simply given by charge/mass and energy conservation laws, related to  $Z_p/Z_t$  and  $A_p/A_t$  of the reaction partners:

$$A_{CN} = A_p + A_t \quad (1.12)$$

$$Z_{CN} = Z_p + Z_t \quad (1.13)$$

$$E^* = \epsilon_{CM} + Q \quad (1.14)$$

where  $\epsilon_{CM}$  is the total kinetic energy of the system in the centre-of-mass frame and  $Q$  is the Q-value of the reaction. For simplicity, in the following discussion, we will drop the subscript "CN". Therefore, given an excited nucleus of mass  $A$ , excitation energy  $E^*$ , charge  $Z$  and angular momentum  $J$ , we are interested in calculating the branching ratio ( $BR^{CN}(f)$  from eq. 1.4) of the different channels in which the system can decay. To do

so, we need to evaluate the transition probability from an initial state "i" to a final state "f" given by Fermi's Golden Rule [6]:

$$\frac{dN_{i \rightarrow f}}{dt} \propto |M_{i \rightarrow f}|^2 \rho_f \quad (1.15)$$

where  $M_{i \rightarrow f}$  represents the transition matrix and  $\rho_f$  is the final states density. As already mentioned, the basic assumption of the statistical model is to consider that all transition matrix elements are equal so that only the density of the final states governs the transition probability. When applied to the case where the final state "f" corresponds to the emission by a parent nucleus "B" of a particle "b" of spin "s", having a kinetic energy between  $\epsilon$  and  $d\epsilon$ , the evaporation probability per unit time for the process  $i \rightarrow b + B$  becomes:

$$P_b(\epsilon)d\epsilon = C_0 \rho_f(E_f^*) dE_f^* (2s + 1) \frac{4\pi p^2 dpV}{h^3} \quad (1.16)$$

This quantity is expressed as the product of three terms. The first one ( $C_0$ ) is a normalization constant which is obtained from the detailed balance principle<sup>1</sup>:

$$P_b \rho_i(E^*) = P_{fus} \rho_f(E_f^*) \quad (1.17)$$

This means that the decay probability is linked to the reverse fusion reaction rate:

$$P_{fus} = \frac{v \sigma_F}{V} \quad (1.18)$$

where  $\sigma_F$  is the fusion cross section of the particle "b" with the final nucleus "B" and  $v$  is its velocity. The second term  $\rho_f(E_f^*) dE_f^*$  is the number of states available for the excited daughter nucleus and lastly,  $\frac{4\pi p^2 dpV}{h^3}$  indicates the number of states of the emitted particle with linear momentum between  $p$  and  $p + dp$ . When evaluating these three terms of eq. 1.16, one finally obtains:

$$P_b(\epsilon)d\epsilon = \frac{\rho_f(E_f^*)}{\rho_i(E^*)} (2s + 1) \frac{4\pi p^2}{h^3} \sigma_F(\epsilon) d\epsilon \quad (1.19)$$

As a consequence of eq. 1.19, a de-excitation channel will be more favourite if the number of accessible states ( $\rho_f$ ) is large, emphasizing the role played by the density of states.

For a more detailed understanding of the emitted particle energy distribution, it is necessary to express the ingredients of this equation. In particular, we have to specify the densities of states for a nucleus with excitation energy between  $E^*$  and  $(E^* + \Delta E^*)$

---

<sup>1</sup>the detailed balance principle assumes that microscopic phenomena are time reversal invariant. Therefore, the transition probability of a system from state "i" to "f" is related to the probability of the inverse transition.

and the fusion cross section. The former can be related, in a microcanonical approach [6], to the entropy<sup>2</sup>  $S$  of the system and to its temperature:

$$S = \ln(\rho(E^*)\Delta E^*) \quad (1.20)$$

$$\frac{1}{T} = \frac{dS}{dE^*} \approx \frac{\Delta \ln \rho(E^*)}{\Delta E^*} \quad (1.21)$$

Hence, the density of states exhibits an exponential evolution with the excitation energy:

$$\rho(E^*) \propto e^{E^*/T} \quad (1.22)$$

This exponential increase in  $\rho(E^*)$  means that for high enough energies the different states form a continuum in which is impossible to separate one level from another, validating once more the use of a statistical approach. The fusion cross section instead may be written by means of eq. 1.6 as it follows:

$$\sigma_F(\epsilon) = \pi R^2 \left( 1 - \frac{B_b^{Coul}}{\epsilon} \right) \quad (1.23)$$

for  $\epsilon \geq B_b^{Coul}$  and zero otherwise. Here  $B_b^{Coul}$  stands for the Coulomb barrier associated with the emission of a particle "b". All these set of equations previously described lead to the final form for the emission probability  $P_b(\epsilon)$  (normalized to unity):

$$P_b(\epsilon) = \frac{\epsilon - B_b^{Coul}}{T^2} e^{-(\epsilon - B_b^{Coul})/T} \quad (1.24)$$

where the excitation energy  $E_f^*$  is expressed as a function of the kinetic energy  $\epsilon$ :  $E_f^* = E_{fmax}^* - \epsilon$ . The temperature "T" in eq. 1.24 is the temperature of the final nucleus. From eq. 1.24, one can notice that the emission  $P_b(\epsilon)$ , thus also the energy distribution, follows a Maxwellian distribution typical of the decay of an equilibrated nucleus.

The previous discussion can be extended to include the whole decay chain of a CN, *i.e.* one can picture the decay to the final state as a sequence of single particle emissions. In this case, "T" represents the mean temperature as every evaporated particle leaves the CN in a new state with an excitation energy less than the initial nucleus. Therefore, the final Maxwellian spectrum is given by the sum of the single evaporation steps. At the end of the evaporation chain, when the daughter's excitation energy is below the particle emission threshold, the ER de-excites by  $\gamma$ -rays emission. An illustrative picture of a fusion-evaporation chain is shown in Figure 1.4. The competition between various channels, *i.e.* the emission probability for different particles may be obtained from the integration of eq. 1.24 before normalization. Without going into the details of this

---

<sup>2</sup>Here we have assumed the Boltzmann constant ( $k_B$ ) equal to 1.

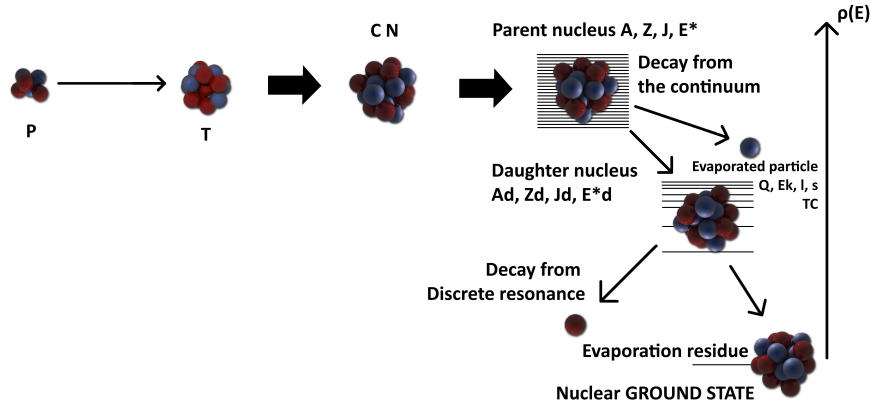


Figure 1.4: Picture of a fusion-evaporation reaction and the following compound nucleus decay.[2].

derivation, the total emission probability for a given particle "b" is mainly influenced by the final state of the daughter nucleus:

$$P_b \propto \rho_f(E_f^* - Q - B_b^{Coul}) \quad (1.25)$$

The statistical model of Hauser-Feshbach, as stated at the beginning, extends this simple model by including a summation over the total angular momentum in the integration of the emission probability. The complete formula for the decay probability used to calculate the branching ratio, will be shown and discussed later on in chapter 4.

The Monte-Carlo implementation (HFI) of the Hauser-Feshbach statistical decay model, was developed within the NUCL-EX collaboration and a detailed description of it is given in ref.[2]. This model in particular was adapted for low mass nuclei ( $A < 40$ ) and all the experimental results obtained are compared with the simulated data filtered with the detector response. In this way we can account for the detector's geometry and angular resolution, as well as the energy thresholds and resolution of the individual detectors.

### 1.3 Structure and Clustering Effects

One of the goals of nuclear reactions is to infer the nuclear structure of the systems formed in the collisions by detecting their decay products. Therefore, one tries to understand the behaviour of protons and neutrons in the nucleus and the force that governs their interaction. Historically, from a theoretical point of view, the first successful model which was introduced was the *shell model*, which was able to define particular stable nuclei configurations based only on an independent particle approximation. This model

explained many important properties of the nucleus such as the binding energy in the ground state, the proton and neutron separation energy and the so called "magic numbers", i.e. the closed shell of neutrons and protons, respectively [13]. Unfortunately, this model could not explain the existence of many other nuclear levels experimentally seen in nuclear collisions. The aforementioned levels were attributed to a correlation between nucleons and to collective excitations of the nuclear system. In order to take these effects into account, new and more complex models were developed, namely the "rotational" and "vibrational" models.

Besides the interest in nucleon-nucleon correlation, another great challenge is the understanding of cluster-cluster (for example  $\alpha$ -clustering) correlation, especially in light nuclei with  $N=Z$ . These new degrees of freedom, therefore, are now included in the new models predicting the nuclear structure. In the last decades, this arguments become of great appeal from both experimental and theoretical perspectives as indicated by the work of many authors [14, 15, 16, 17, 18]. As a result, starting from the '60s, a campaign of measurements began to search for resonant structure in the excitation function for various combinations of light  $N=Z$  nuclei in the energy regime from the Coulomb barrier up to regions with excitation energies of  $E^* = 20 - 50$  MeV. Different types of clustering behaviour were identified in nuclei (see Figure 1.5), from small clusters outside closed shells, to complete condensation into  $\alpha$ -particles, to halo nucleons outside of normal core.

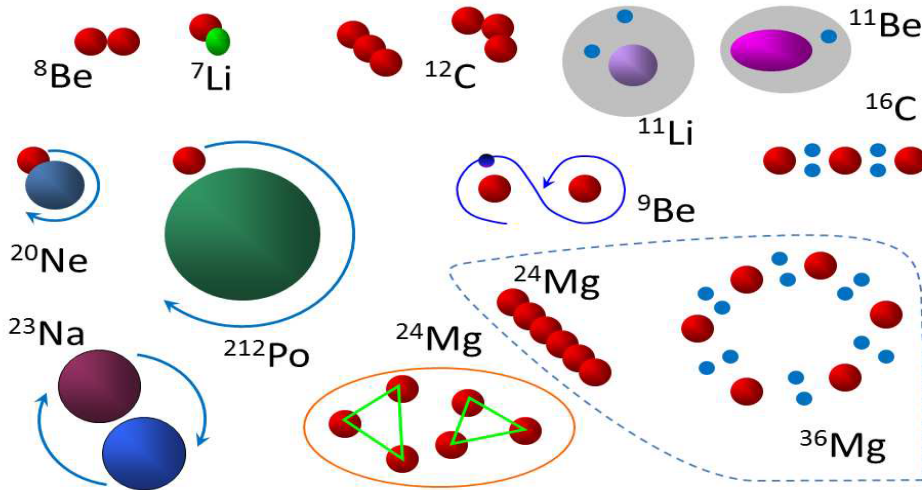


Figure 1.5: Variety of types of nuclear clustering [19].

In light alpha-conjugate nuclei, clustering is observed as a general phenomenon at high excitation energy close to the alpha-decay thresholds. This exotic behaviour is well illustrated in the "Ikeda-diagram" for  $N=Z$  nuclei [20], which has been modified and extended by von Oertzen [21] for neutron-rich nuclei, as shown in Figure 1.6. For

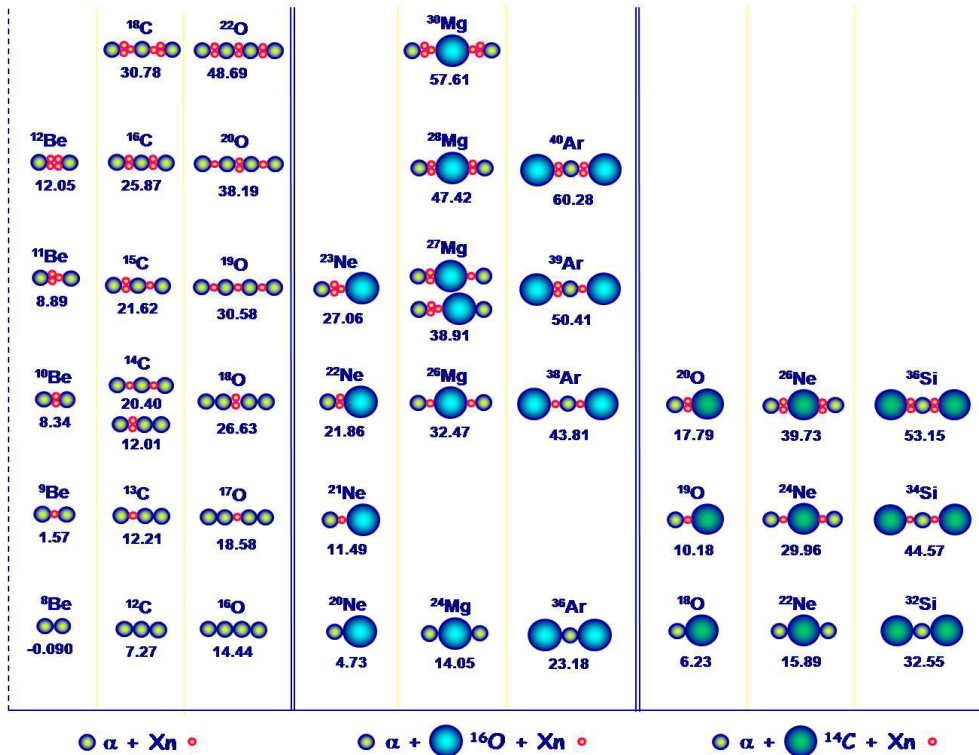


Figure 1.6: Extended Ikeda-diagram with  $\alpha$ -particles (left),  $^{16}\text{O}$ -cores (middle) and  $^{14}\text{C}$ -cores (left) [21]. The numbers represent the threshold energy (in MeV) dissociating the ground state into the respective cluster configuration.

example, in the bottom left side of Figure 1.6, the  $^{16}\text{O}$  nucleus at excitation energy above 14.44 MeV can be sketched as a system formed by 4- $\alpha$  particles. The unstable ground state of  $^8\text{Be}$  is maybe the most simple and convincing example of alpha clustering in light nuclei and it is well known to decay into two  $\alpha$  particles with a half-life of  $2.6 \cdot 10^{-6}\text{s}$ .

Moreover, clusterization is intimately connected with the formation of elements and even life itself. These two aspects intersect in  $^{12}\text{C}$  and the Hoyle-state. This excited state (7.65 MeV) of  $^{12}\text{C}$  was proposed by Sir Fred Hoyle more than 50 years ago [22] and represents the gateway through which carbon is synthesized in stars via what is known as the triple-alpha process:



Its actual structure in terms of alpha-particle components has been described in various ways, from a linear  $\alpha$ -chain [23], to a Bose-Einstein condensate or a dilute alpha-particle gas [24]. Still, the structure of the Hoyle state remains controversial as experimental results in favour of one or another hypothesis are found to be in disagreement [25, 26]. It is an argument of debate whether the decay mechanism is sequential, through the formation

of  ${}^8\text{Be}_{gs}$ , or if the simultaneous decay in three  $\alpha$ -particles can play a significant role in the decay of the Hoyle state. The results mentioned in [26, 27, 28], all indicate the former as the dominant process with a very low limit to the possible contribution from the latter process. On the contrary, the authors in [25] have measured, in a reaction with heavier systems than the aforementioned results, a few percent contribution of the simultaneous decay to the total decay mechanism of the Hoyle state. Further measurements are needed in order to investigate if a large nuclear medium, as in the second case, can affect the decay mechanism of this Carbon excited state.

### 1.3.1 The ${}^{16}\text{O}$ nucleus

Similarly to the  ${}^{12}\text{C}$ , a quest for 4- $\alpha$  or carbon-core based cluster states in  ${}^{16}\text{O}$ , as in Figure 1.6, has started. In particular, these state can be detected near the  ${}^8\text{Be}+{}^8\text{Be}$  and  ${}^{12}\text{C} + \alpha$  decay thresholds. In 1967 Chevalier et al. [29] could excite these states in an alpha-particle transfer channel leading to the  ${}^8\text{Be}+{}^8\text{Be}$  final state. They then proposed that a structure corresponding to a rigidly rotating linear arrangement of four alpha particles may exist in  ${}^{16}\text{O}$ . The  ${}^8\text{Be}+{}^8\text{Be}$  decay has also been studied in a measurement of the  ${}^{12}\text{C}({}^{16}\text{O}, 4\alpha){}^{12}\text{C}$  by Freer et al. [30]. Despite the fact that many of the states found in the excitation spectrum by Freer et al., and other more recent works [31], coincide with the ones found by Chevalier et al., the current results do not provide enough evidence to confirm the proposed linear chain of four  $\alpha$ -particles.

More recently, in the case of a  ${}^{12}\text{C}$  core, a new state with the structure of a Hoyle state coupled to an alpha particle was predicted in  ${}^{16}\text{O}$  at about 15.1 MeV [32]. The energy of this state is just 700 keV above the 4- $\alpha$  breakup threshold, therefore it is expected to decay mainly by alpha emission to the Hoyle state with very small gamma decay branches. From a theoretical point of view, this was interpreted by [32] as a signature of Bose-Einstein condensation. To confirm this hypothesis, the  ${}^{16}\text{O}$  excitation spectrum must be measured with very efficient coincident particle detection which allows to have a good background rejection and to clearly separate the levels of interest.

## 1.4 The ${}^{16}\text{O}+{}^{12}\text{C}$ Reaction

The aim of the experiment performed and analyzed during the work for this thesis is to progress in the understanding of statistical properties of light nuclei as well as studying new  $\alpha$ -cluster states at excitation energies above particle emission thresholds. By using an exclusive channel selection and a highly constrained statistical code, one is able to put in evidence deviations from a statistical behaviour in the decay of hot fused nuclei formed in heavy-ion collisions. Moreover, one can also select a reaction leading to the excited projectile-like nucleus formed in a non-central collision and study the decay of this system. This is one of the methods used in literature to study the

Hoyle state cluster structure, as described in section 1.3, and that of many other nuclei as well. Hence, given this reaction, one is capable of performing both statistical decay and particle spectroscopy experimental studies.

The reactions,  $^{16}\text{O}+^{12}\text{C}$  at 90.5, 110 and 130 MeV incident energy, have been investigated within the campaign started by the NUCL-EX collaboration. The goal was to study the physics case previously described in this chapter. The results obtained in the past by the collaboration suggested a possible alpha-structure correlation in the  $^{24}\text{Mg}$  compound nucleus formed in two different reactions ( $^{12}\text{C} + ^{12}\text{C}$  at 95 MeV and  $^{14}\text{N} + ^{10}\text{B}$  at 80.7 MeV) but populated at the same excitation energy [3]. The reactions were performed in order to study if an influence of the entrance channel is present, by specifically using reaction partners with ( $^{12}\text{C} + ^{12}\text{C}$ ) and without ( $^{14}\text{N} + ^{10}\text{B}$ ) a definite cluster structure. The experiments used the same GARFIELD + RCo apparatus to detect the reaction products. A general description of the detector is given in Chapter 2.

The analysis focused on the selection of fusion-evaporation channel mechanism, based on the coincidence between LCP's (GARFIELD) and an evaporation residue (RCo) in complete events (total detection of the charge). A first hint for a possible contamination from  $\alpha$ -structure correlation came from the comparison between energy spectra, from protons and  $\alpha$  particles detected in GARFIELD in coincidence with different residue, and a Hauser-Feshbach statistical model as shown in Figure 1.7. For the  $^{12}\text{C} + ^{12}\text{C}$  reaction, this figure shows a very good agreement between the data and the model for the proton energy spectra while the same cannot be stated for the  $\alpha$ -particles detected in coincidence with an Oxygen fragment. In particular, in the  $\text{O} + 2\alpha$  channel a much higher experimental branching ratio with respect to the model was evinced [3].

The experiment of this thesis is a natural extension of the aforementioned studies as the cluster correlation previously observed in the decay of the excited  $^{24}\text{Mg}$  nucleus could possibly be present also in the  $^{28}\text{Si}$  at higher excitation energies. Furthermore, due to the three different beam energies, one could also investigate the evolution of the clustering degree of freedom varying the excitation energy of the system, as recently done by Vadas et al. [33].

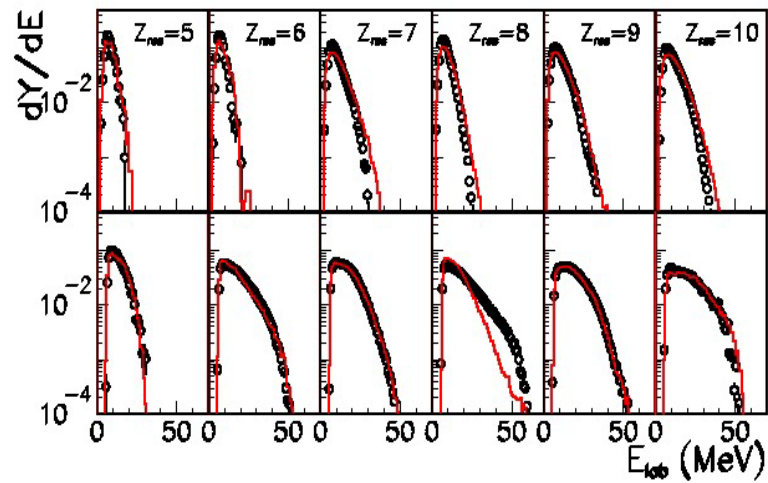


Figure 1.7: Proton (upper part) and  $\alpha$  (lower part) energy spectra in complete  $Z_{det}=12$  events detected in coincide with a  $Z_{res}$  charge residue, for the  $^{12}C + ^{12}C$  reaction at 95 MeV incident energy. The black dots indicate the experimental measurements while the red lines are the model predictions [3].

# Chapter 2

## The Experimental Apparatus

In nuclear heavy ion reactions, one has to detect a very large number of different particles, from protons to fission fragments, in a wide range of energy which can vary from tens of keV to GeV. These are very important to study the behaviour of a nuclear system undergoing a reaction. For instance, in the case of a compound nucleus, any change in its nuclear matter characteristics such as pressure, density or isospin, can be correlated to the variation of experimental signatures directly obtained from the detected products .

More in general, to efficiently measure, disentangle and weight all decay channels of an excited system formed in a collision, it is necessary to detect and identify all the reaction products. Thus the use of G.AR.F.I.E.L.D (*General ARray for Fragment Identification and for Emitted Light particles*) detector, coupled with Ring Counter (RCo) and installed at LNL-INFN [34], is very well suited for such measurements. Using these two detectors allows having for every event nearly complete information on light charged particles and more heavier mass fragments.

The coupled system covers nearly  $4\pi$  of the total angle with high granularity, low energy thresholds, large dynamic ranges in energies and identification capabilities on an event by event basis. These characteristics are fundamental for a complete reconstruction of the kinematics for each event.

In the following sections, we briefly describe the main features and working principles of the experimental apparatus used to perform the experiment.

### 2.1 GARFIELD Apparatus

GARFIELD is a multi-detector consisting of two large-volume drift chambers, C1 and C2 (Figure 2.1), placed back to back with respect to the target. The detector is equipped with digital electronics and it is mainly based on  $\Delta E$ -E telescopes. These telescopes exploit energy measurements in two different stages of the detector to obtain

charge identification and accurate energy measurements of the reaction products.

The forward chamber (C2) has cylindrical symmetry with respect to the beam axis and it is mechanically divided into 24 azimuthal sectors. Each sector has four CsI(Tl) crystals covering the polar angular region between  $29.5^\circ < \theta < 82.5^\circ$ , plus a micro-strip gas chamber pad (*MSGC*) that is used as the first stage of detection ( $\Delta E$  stage), whereas the CsI(Tl) crystals measure the residual energy of particles (E stage). Overall, the forward chamber consists of 96  $\Delta E(\text{gas})\text{-E}(\text{CsI(Tl)})$  modules. The scintillators have different

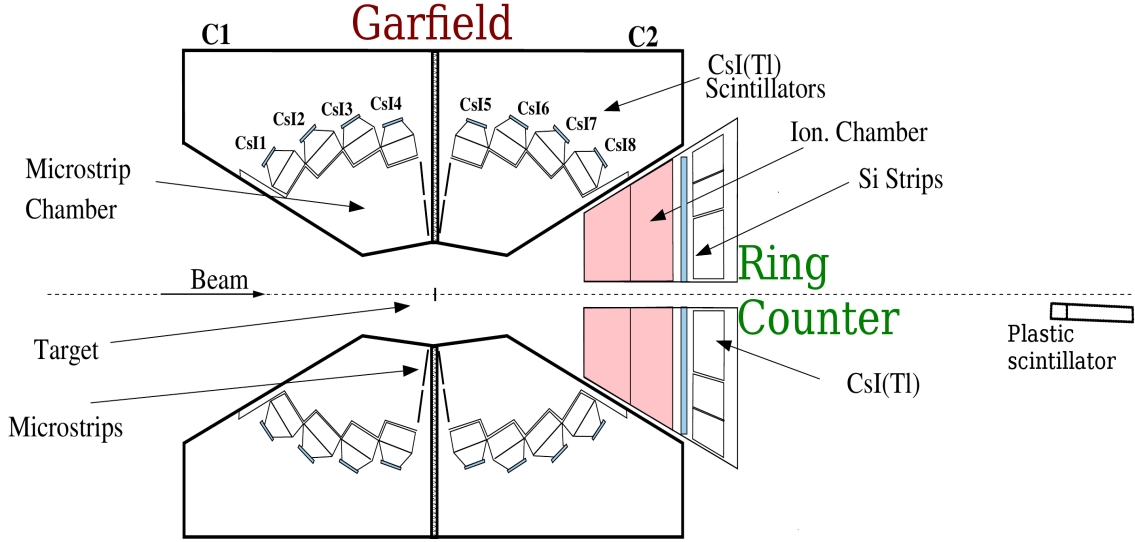


Figure 2.1: Trasverse view of the GARFIELD Appartus coupled with the RCo.

shape and dimensions as to adapt better to the polar angle  $\theta$  (Table 2.1). Furthermore, they are placed in such a way that impinging particles coming from the target enter perpendicularly to the crystal face in its center (Figure 2.2).

	CsI-1	CsI-2	CsI-3	CsI-4	CsI-5	CsI-6	CsI-7	CsI-8
$\theta_{min}$	139.9°	127.5°	113.5°	97.5°	68.0°	53.0°	41.0°	29.5°
$\theta_c$	145.2°	133.0°	120.0°	104.8°	75.3°	60.0°	47.0°	34.9°
$\theta_{max}$	150.4°	138.5°	126.5°	112.0°	82.5°	66.0°	52.0°	40.0°

Table 2.1: Minimum, central and maximum angles corresponding to the regions covered by each GARFIELD CsI(Tl) crystal.

The backward chamber (C1) covers the region  $97.5^\circ < \theta < 150.4^\circ$ . This drift chamber has a structure very similar to C2 except for the fact that three sectors are missing, reducing the total coverage in  $\phi$ . Nevertheless, a total active solid angle of 7.8 sr is

covered by the two chambers. The intent of this design is to allow for future mounting of other possible detectors like the ones studied by the FAZIA collaboration [35].

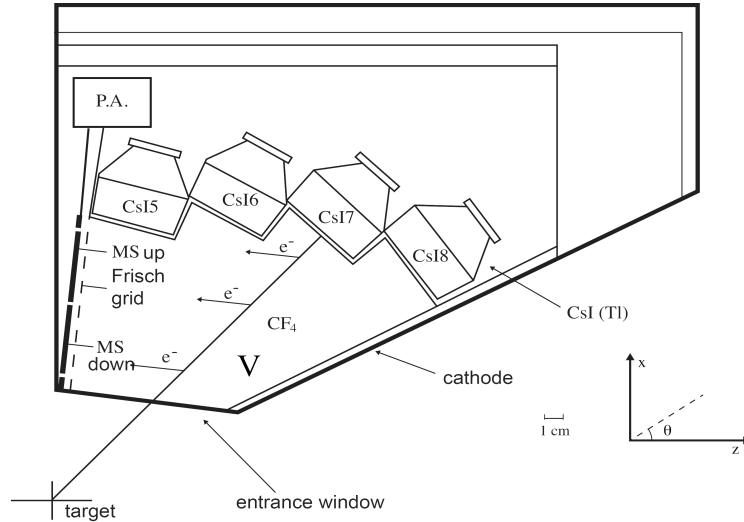


Figure 2.2: Lateral view of one of Garfield's sectors.

Granularity is obtained by dividing each GARFIELD drift chamber in sectors with an angular width of  $\Delta\phi = 15^\circ$ . An even greater granularity is then achieved by taking advantage of the fact that the microstrip pads are further divided in the azimuthal coordinate. This characteristic is well illustrated in Figure 2.3. All in all, the apparatus can reach angular resolutions of  $\Delta\phi = 7.5^\circ$  and  $\Delta\theta = 14^\circ$  if the chambers are used as ionization chambers. The azimuthal resolution is increased to about  $1^\circ$  if also the drift time is used.

The two drift chambers are filled with flowing  $CF_4$  (*carbon tetrafluoride*) gas at a pressure around 50 mbar for C2 and around 20 mbar for C1. In the latter case, the adopted pressure is lower since the only backward detected particles are protons and alpha. Therefore, only the PSA technique with the CsI(Tl) is employed and the lower pressure allows having lower identification thresholds. Even so, a minimum value of 20 mbar has to be used as to cool down the preamplifier electronics located inside the chamber. The employed  $CF_4$  is a stable gas and it is suitable for detectors due to its high stopping power (five times larger than  $CH_4$  and 17 % more than isobutane), high density ( $3.93 \text{ mg/cm}^3$  at STP) and relatively low cost. Its average ionizing potential is around 16 eV and it has a high drift velocity (about  $10 \text{ cm}/\mu\text{s}$  at  $1 \text{ V/cm} \cdot \text{Torr}$ ). This being said, the charge produced is usually collected within 2-3  $\mu\text{s}$ .

### 2.1.1 Drift Chamber and Microstrip

The particles produced in a reaction, after passing through the entrance window, enter into the drift chambers where they interact with the gas. This interaction is due to the Coulomb force (electromagnetic interaction) and can cause either excitation or ionization of the gas molecules. It is this second process that generates the electron-ion pairs which represent the charge carriers. These carriers are afterwards collected by the electrodes due to the drift field created inside the gas volume.

The GARFIELD chambers have a  $6\ \mu\text{m}$  thick ( $0.78\ \text{mg}/\text{cm}^2$ ) mylar entrance window with thin metallic deposited strips. This thickness keeps low the window dead layer while maintaining a safe mechanical robustness to sustain the pressure deformations. The gas circulates in a closed circuit system and it is forced to flow in a continuous cycle (the time required for a total replacement is of the order of minutes). This is necessary for the purpose of eliminating any impurity or contamination such as molecules produced by the  $CF_4$  breaking or oxygen and water vapor infiltrations.

Inside the drift chamber a drift cathode at around  $-1000\ \text{V}$  and a Frisch grid (at  $60\ \text{V}$ ) generate an electrical field oriented in such way that the electrons formed along the trajectory of the particles are forced to drift toward the microstrip pads (see Figure 2.2). Due to the geometry of the sector, the cathode is made by many strips kept at the proper voltages via a resistive divider to make the electric field as homogeneous as possible. For the same reason, a series of additional electrodes are used at different potential via resistive dividers (scaled taking into account the irregular shape of the chamber) also on the front and side surfaces of the various CsI crystals and on the entrance window. These electrodes contribute to maintain the electric field uniform so that electrons move with constant drift velocity. Typical values of electric field inside the GARFIELD chamber are of the order of  $10^4\ \text{V}/\text{m}$ .

The Frisch grid separates the region close to the microstrips, in which the electric field reaches a much greater intensity and sufficient to start the multiplication effect (avalanche effect), from the region where the electrons simply drift towards the electrodes. Moreover, it prevents the induction of signals on the microstrips when charge carriers drift in the active gas volume and it eliminates the positive ions contribution to the signals.

The microstrip pads (Figure 2.3) have a trapezoidal shape (with dimensions of approximately  $4\ \text{cm}$  for the larger base,  $2\ \text{cm}$  for the smaller base and  $7\ \text{cm}$  for the height) and they are placed almost perpendicular to the beam axis. Each pad is divided into four charge collection zones, indicated conventionally with  $ul$ ,  $ur$ ,  $dl$  and  $dr$ . The letters  $u$ ,  $d$ ,  $l$  and  $r$  stand for *up*, *down*, *left* and *right* when one looks at the glass pads with the small base downward. Therefore, the two down areas are those closest to the beam, while the two up are the furthest. The division of each pad allows having four independent regions of signal collection, hence providing  $\Delta E$  values to use for  $\Delta E - E$  correlations. The cathodes are generally grounded whereas the anodes are connected to a certain bias voltage which allows the device to operate in a proportional mode. Therefore, the num-

ber of collected electrons and the output signal are proportional to the energy deposited by the incident particle.

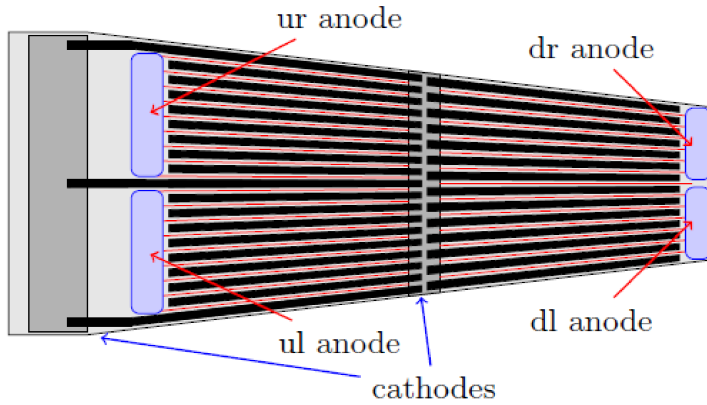


Figure 2.3: Microstrip geometry and division in the four electrically separated regions of signal collection.

The choice of using microstrip gas as detectors was influenced by two important requests. First of all, it is necessary to keep the identification energy threshold as low as possible (around 0.8-1 MeV/A) and secondly, they still have to be able to detect particles with a wide range of energies. Furthermore, MSGC have the advantage of a high signal-to-noise ratio for low ionization ions. In fact, microstrip chambers can sustain high counting rate and high gains (gain factor varying from 30 to 50 ) and they are nevertheless drift chamber which makes it possible the measurement of the particle position .

### 2.1.2 CsI(Tl) Crystals

As mentioned in the previous section, the GARFIELD apparatus uses mainly  $\Delta E - E$  modules to detect and identify the incident particles. After the first  $\Delta E$  part, for the last stage of detection a detector that can stop and efficiently measure the reaction products that pass through the gas volume is needed. Therefore, CsI(Tl) crystals have been chosen due to their excellent characteristics, like the high stopping power, the sufficiently good energy resolution (close to 3%-4% with 5.5 MeV  $\alpha$  particles from  $^{241}\text{Am}$  source [36]), the small sensitivity to the radiation damage and the fact that they are quite easy to cut and machine in order to obtain the shape needed for the experiment. These crystals in particular, have variable thicknesses of about 3-4 cm and different shapes depending on

the  $\theta$  angle, as already mentioned in section 1.1 . The different shapes of GARFIELD CsI(Tl) crystals are illustrated in Figure 2.4.

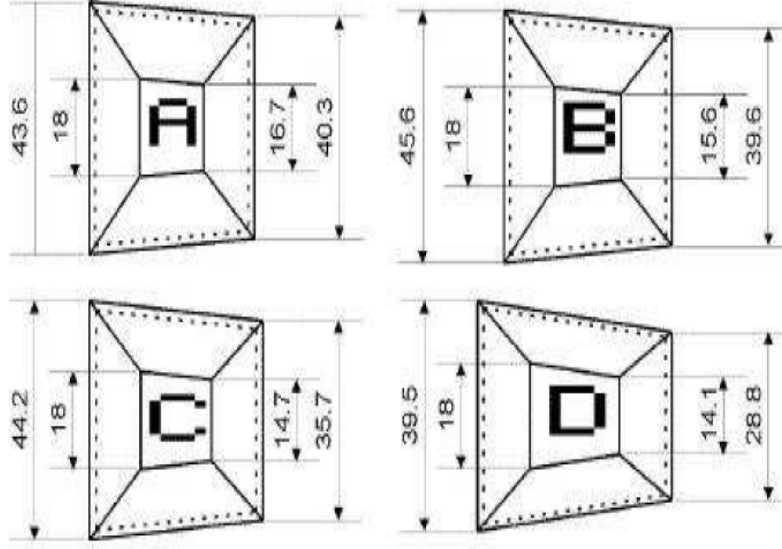


Figure 2.4: Shape of GARFIELD CsI(Tl) crystals. The A shape corresponds to the nearest to the microstrip plane ( $\theta$  greater with respect to the beam line).

Another advantage of CsI(Tl) detectors is the possibility to perform *pulse shape analysis* (PSA) for detected particles. As a matter of fact, the scintillation of the CsI(Tl) crystal is well described by the sum of two exponentials with different time constants: a short one ( $\tau_s \sim 0.75\mu s$ ) and a long one ( $\tau_l \sim 5\mu s$ ). As a result, the current pulse produced in the photodiode by the scintillation light is described by:

$$i_l(t) = \frac{dQ_L(t)}{dt} = \frac{Q_s}{\tau_s} e^{-\frac{t}{\tau_s}} + \frac{Q_l}{\tau_l} e^{-\frac{t}{\tau_l}} \quad (2.1)$$

where  $Q_L(t)$  is the whole collected charge at time  $t$ ;  $Q_s$  and  $Q_l$  are the charges produced respectively by short and long components of scintillation.  $Q_L$  is thus given by:

$$Q_L = \int_0^{\infty} \frac{dQ_L(t)}{dt} dt = Q_s + Q_l \quad (2.2)$$

Particle identification capability comes from the different charge and mass dependence of  $Q_s$  and  $Q_l$  components. Also  $\tau_s$  and  $\tau_l$  values slightly depend on charge and mass of the particle. In general, with the same total charge, the short component grows when  $Z$  increases.

Concerning their stopping properties, these crystals are able to stop protons and  $\alpha$ -particles with energies up to  $\sim 100$  MeV/u. Each crystal is wrapped in a white diffusive paper to maximize the collection of light and finally protected with an opaque layer to avoid light penetration from outside. This is to be considered as an additional  $1.5\mu\text{m}$  thick dead layer when reconstructing the original energy of particles from the residual energy. The rear part of the crystal is tapered to behave as a light guide and it narrows to reach the dimensions of the photodiode coupled to the crystal. This photodiode is the model S3204-05 manufactured by Hamamatsu, with an active area of 18 mm x 18 mm. The choice of using photodiodes instead of photomultiplier tubes is due to their greater stability, low power dissipation, much smaller size and to their low bias voltage ( $\sim 100\text{V}$ ) which makes possible the operation inside the GARFIELD low pressure gas chamber.

## 2.2 Ring Counter

The Ring Counter (RCo) is an annular detector designed to be centered at  $0^\circ$  with respect to the beam direction. It is an array of three-stage telescopes realized in a truncated cone shape. The first stage is an ionization chamber (IC), followed by a strip silicon detector (Si) while the last stage is formed by CsI(Tl) scintillators. The RCo uses PSA and the  $\Delta E - E$  telescope techniques to identify and detect particles. Each stage of the RCo is mounted on a low-mass aluminum support that is adjustable, for the relative alignment of all the active elements of the device. The preamplifiers are mounted on the same sliding plate of the RCo. A picture of the whole apparatus is shown in Figure 2.5.

During the measurement, the Ring Counter is inserted just in the forward cone of the GARFIELD metallic cage and its entrance window is placed 170 mm far from the target. The detector covers the polar angles in the range  $5.4^\circ < \theta < 17.0^\circ$ . The Ring Counter has a cylindrical symmetry along the beam axis and it is divided into 8 azimuthal sectors. Each sector thus covers  $45^\circ$  in  $\phi$  (azimuthal coordinate).

The IC is a 6 cm long axial type chamber with the electric field parallel to the ion tracks in the gas. The field inside the IC is generated by three aluminized mylar electrodes. There are two input-output electrodes which are the grounded cathodes, while the anode is a central foil with metal deposition on both faces. The mylar cathodes act also as gas windows and are metallized only on the internal face. Since the anode is in between the two cathodes, its voltage can be kept halved with respect to a geometry with only two electrodes for the same gas gap. The cathodes are azimuthally divided into eight parts in order to follow the 8-sector partition of the RCo in the  $\phi$  coordinate. The gas ( $CF_4$ ) used is the same as in GARFIELD's drift chambers.

Behind each IC sector is placed a trapezoidal  $300\mu\text{m}$  thick Silicon (nTD) pad. These pads are segmented into eight strips increasing the detector's granularity (Figure 2.6) up

Strip	Int. radius (mm)	Ext. radius (mm)	Min. angle (deg)	Max. angle (deg)
1	77.9	85.0	15.6	17.0
2	70.8	77.8	14.2	15.6
3	63.7	70.7	12.9	14.2
4	56.6	63.6	11.5	12.8
5	49.4	56.4	10.1	11.4
6	42.3	49.3	8.6	10.0
7	35.2	42.2	7.2	8.6
8	26.2	35.1	5.4	7.2

Table 2.2: Radii and polar angle limits of RCo silicon strips.

to  $\Delta\theta \approx \pm 0.7^\circ$  for the polar angle. The use of silicon detectors allows to obtain an energy resolution of around 0.3%. They are reverse mounted, namely oriented in such a way that the particles impinge on the ohmic side. This mounting has been studied by the FAZIA group and proved to increase the fragment discrimination capabilities by means of PSA [37] as it will be discussed in 3.2.3. In Table 2.2 above are listed the radii and angles covered by each of the 8 strips. The overall geometrical coverage of the Si stage is about 90%. The remaining inactive area is due to the interstrip regions, containing the guard rings, and to the printed circuit board frame that holds each Si sector.

Finally, for each sector, there are 6 CsI(Tl) crystals read by a photodiode (model S2744-08 manufactured by Hamamatsu) with active area 10 mm x 18 mm. These crystals are similar to those employed in GARFIELD but they have a different percentage

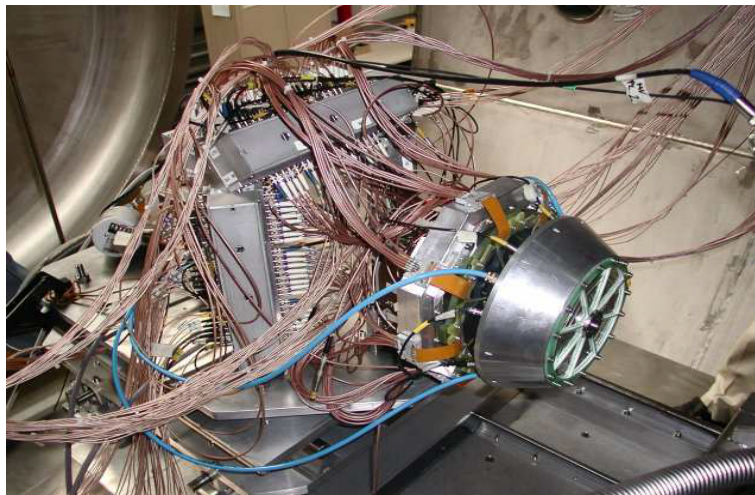


Figure 2.5: Picture of the Ring Counter detector and the electronic counterpart connected to this detector.

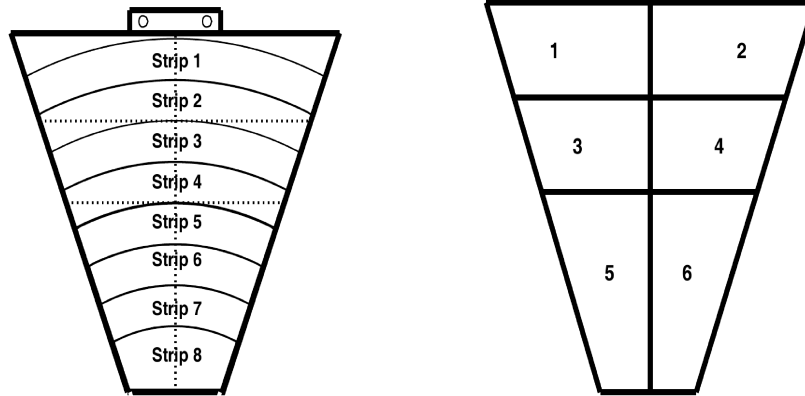


Figure 2.6: The Ring Counter's silicon strips (left) and the superposition (right) with the corresponding Cesium crystals.

of thallium doping (between 1500 and 2000 ppm) as to enhance their light output. Altogether, we have 48 Cesium Iodide crystals, each one covering half sector in the azimuthal coordinate. As a result of the mentioned division in sectors, an accuracy of  $22.5^\circ$  is obtained in the azimuthal angle of the particles impinging on the scintillators. These CsI(Tl) crystals can also reach an overall 2-3% energy resolution. The designed overlap between Silicon pads and CsI(Tl) crystals is illustrated in Figure 2.6 and it can be seen that at least two Silicon strips correspond to each crystal.

## 2.3 Electronics

The various detectors, except for the GARFIELD drift chamber, are equipped with digital electronic processing stages. Each signal, from all the detectors, is processed by charge sensitive preamplifiers with different gain. These preamplifiers are located inside the scattering chamber to reduce noise influence upon the already small signals generated. Subsequently, the outputs of the preamplifiers are feed into digital cards developed within the collaboration by the Florence group. These cards contain a 125 MHz, 12 bit ADC (*Analog-to-Digital Converter*) and a DSP (*Digital Signal Processor*).

The DSP is programmable and it is capable of performing advanced on-line data reduction [38]. This means that instead of sending all the digitized samples to the acquisition, the DSP elaborates the data and reduces them by applying filtering and shaping algorithms. According to the different detector type a specific calculation is performed and the DSP also extracts information like time and parameters apt to particle identification from the sampled signal. For example, a semi-gaussian digital filter is applied to the signal coming out from every detector; this is particularly useful for

extracting the maximum amplitude which it is known to be proportional to the energy of the incident particles. However, so as to check the behaviour of the cards, every 1000 events the DSP sends a complete waveform to acquisition for further off-line checks and debugging analysis. In Figure 2.7 the structure diagram of an acquisition channel is shown.

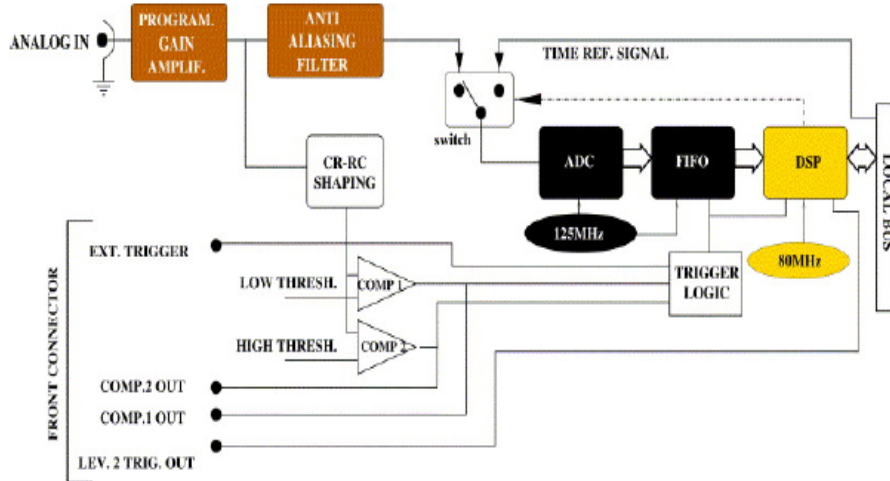


Figure 2.7: Main components of a digital acquisition channel: an analog input stage, the ADC, an internal FIFO (*First In First Out*) memory, a trigger section and the DSP.

Signals coming from the microstrip pads, inside GARFIELD’s drift chambers, instead are processed by a usual analog chain which is made of a charge amplifier followed by a peak sensing ADC. A digital upgrade, for the GARFIELD drift chamber, is currently underway in order to have a better position determination from the drift time.

### 2.3.1 Triggers and Acquisition

As shown in Figure 2.7, the acquisition system contains a section called trigger logic. This results to be fundamental for the experiment as it represents a direct connection with the physics of the reaction. To be more precise, it allows us to impose physical conditions using logical combinations of trigger signals based on the type of reaction mechanism we want to study. If we acquire everything coming from the detectors, most of the data would be useless events mostly dominated by the elastic and quasi-elastic rates.

These selections are made by using two types of triggers, namely local triggers and validation signals. The first ones are generated from a detector signal that has exceeded its acquisition threshold by means of a CFD (*Constant Fraction Discrimination*). Therefore, it is possible to obtain local triggers from GARFIELD’s CsI(Tl) crystals or from the

Bit	Trigger	Reduction	Description
0	OR CsI GARF	2	OR of the GARFIELD scintillators
1	OR IC RCo	1	OR of the different parts of IC
2	OR Si RCo	1	OR among the RCo strips
3	OR GARF AND OR Si RCo	1	AND of trigger 0 and trigger 2
4	OR GARF AND OR IC RCo	1	AND of trigger 0 and trigger 1
5	OR Si AND OR IC	1	AND of trigger 2 and trigger 1
6	Plastic Monitor	100	Plastic Scintillator
7	Pulser	1	Pulse Generator

Table 2.3: The available triggers with their reduction factors which include the ones selected during the measurements.

RCo silicon detectors. On the other hand, a validation signal is generated by a trigger box (CAEN V1495), which is a VME standard electronic board, featuring an FPGA (*Field Programmable logic array*) programmed to perform coincidence and trigger tasks. This trigger box collects all the various local triggers and generates a validation signal according to a user defined table of possible combinations inside a specific time window. When a validation signal occurs, the acquisition starts and the DSP sends its data to be stored on disk.

During the experiment, up to eight different local trigger combinations can be programmed. The trigger-box output is a bitmask that indicates which trigger was activated. In Table 2.3 are reported the different triggers available for this experimental campaign. Each bit is associated with a particular type of trigger. Moreover, often it was used a reduction factor "R" as to activate the acquisition once every "R" occurrences. Throughout this experiment, the triggers selected were trigger 0 and trigger 2 (Table 2.3). These two triggers, are imposed by the light nature of the excited system produced in the reaction and its kinematics, be it a CN or projectile-like fragment. In fact, in the former case one will mainly have an evaporation residue at small angles in RCo and few LCP in GARFIELD. Therefore, we adopted as the main physics trigger the OR of triggers signals coming from the RCo (trigger 2) and the additional OR from the GARFIELD signals (trigger 0). More specifically, trigger 0 is the logic OR of all CsI(Tl) signals while trigger 2 is obtained from the logic OR of Si strip signals. The coincidence (logic AND) between these two triggers (trigger 3), even though non activated, can be recovered during the offline analysis.

Besides the measurement triggers mentioned above, two additional triggers were used. One of them is a pulser trigger (bit 7 in Table 2.3), applied to control the stability of the whole electronic chain. This is especially useful when interested to sum data from several runs of measurement. A pulse generator creates signals with a well known amplitude and stable in time, which can be employed afterwards to correct potential faults due to

the electronic response. And last, bit 6 is a trigger referred to a plastic scintillator that is positioned at a polar angle ( $\theta \simeq 1.2^\circ$ ) smaller than the *grazing angle*. This scintillator registers elastic Rutherford scattering events in order to normalize counts to the absolute cross sections.

# Chapter 3

## The Experimental Measurement and Energy Calibration

In the first part of this chapter, the experimental conditions of the reactions measurement are introduced. Then we will proceed by describing the methods used to identify the particles detected with the GARFIELD + RCo apparatus.

These methods, as mentioned in Chapter 2, are the  $\Delta E$ - $E$  and the Pulse Shape techniques for particles detected with Cesium Iodide scintillators. Furthermore, since the RCo detector is equipped with a silicon detection stage it is also possible to make use of a Pulse Shape technique, consisting in an energy-rise time correlation to identify particles. Another section will be dedicated to the energy calibration process of the apparatus, mainly through the elastically scattered Oxygen ejectiles by a  $^{197}\text{Au}$  target, measured between the different runs of the experiment. This allows to calibrate in energy the response of the silicon detector and therefore to reconstruct the energy of the incident particles impinging on a detector. Finally, we will present a few global observables able to select the particular reaction mechanisms of interest.

### 3.1 The Measurement

The measurements were performed using a pulsed beam (1 ns resolution and 400 ns repetition period) of  $^{16}\text{O}$  with an energy of 90.5, 110 and 130 MeV supplied by the Tandem XTU accelerator at the INFN laboratories in Legnaro. This electrostatic accelerator is based on two acceleration stages, as it is shown by the operational sketch in Figure 3.1. Ions are generated inside an external source and are extracted with a weakly positive charge state ( $q=+1$ ). Before entering in Tandem, the ions cross a charge-exchange region filled with gas (Cesium) in which, by playing on the relative electronic affinity, there is a high probability of receiving two electrons from the gas. With such charge state ( $q=-1$ ), the ions enter the low energy side of the tandem and are

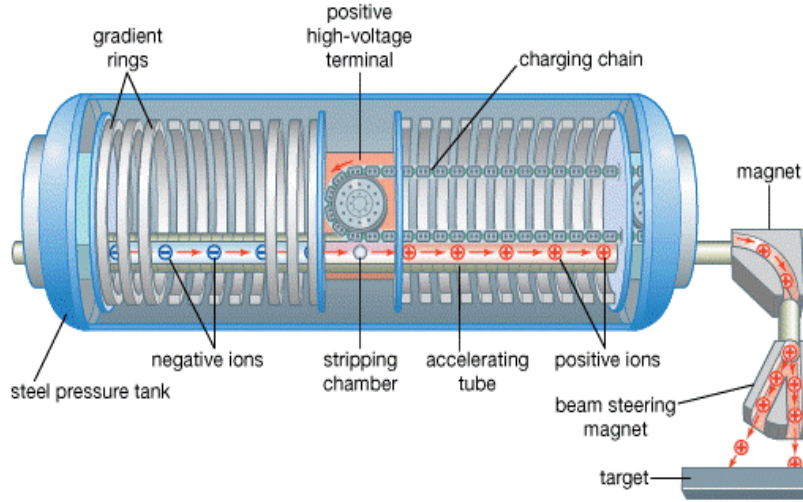


Figure 3.1: Illustration of a Tandem accelerator were the following elements can be identified: the accelerating pipe, the column which supports the high voltage terminal, the "stripping" chamber, the "ladderton" charging belt and last the bending magnets .

attracted towards a high voltage terminal (HVT) at +14.5 MV, located in the centre of the accelerator. Inside the terminal (a Faraday cage), the ions pass through a very thin carbon foil called "stripper". As the name suggests, this device can strip a large number of electrons to the ions (up to  $q=10-20$  depending on the ion type and the acquired energy). The ions then enter the opposite side of the HVT with a highly positive charge state. The repulsive electrostatic field then accelerates furthermore the ions in the second half of the accelerator. Afterwards, the exiting particles are driven, using magnetic deflectors and lenses, towards the measurement apparatus where the target is located.

The  $^{16}\text{O}$  generated beam, in our case having a maximum intensity of about 0.1 pA, impinges on  $^{12}\text{C}$  self-supporting target with a thickness of  $85 \mu\text{g}/\text{cm}^2$ . In the case of complete fusion, for the three beam energies (90.5, 110 and 130 MeV), such reaction leads to a fused  $^{28}\text{Si}$  system respectively at 55, 63 and 72 MeV excitation energy. The trigger configuration, described in section 2.3.1, focuses on the selection of a fused system (CN). Nevertheless, it is sufficiently flexible to allow studying peripheral events as well. An automatic system was available for changing target operations in order to swap between the slots containing the carbon foils and therefore avoid wear off the target. Under the same beam conditions, the  $^{16}\text{O}+^{197}\text{Au}$  reaction was measured providing a reference point for the energy calibration by means of the elastically scattered  $^{16}\text{O}$  ions. Together with the Gold and Carbon foils, an additional  $\text{AlO}_2$  target was present in the target holder. Its purpose is to allow for the initial beam focalization. Indeed this material is lighten when hit by the beam. A central hole allows to position the beam on the center of the

target, also by maintaining the alignment with two other  $AlO_2$  foils positioned at the beginning and at the end of the scattering chamber, and to control its size to about 1mm in diameter .

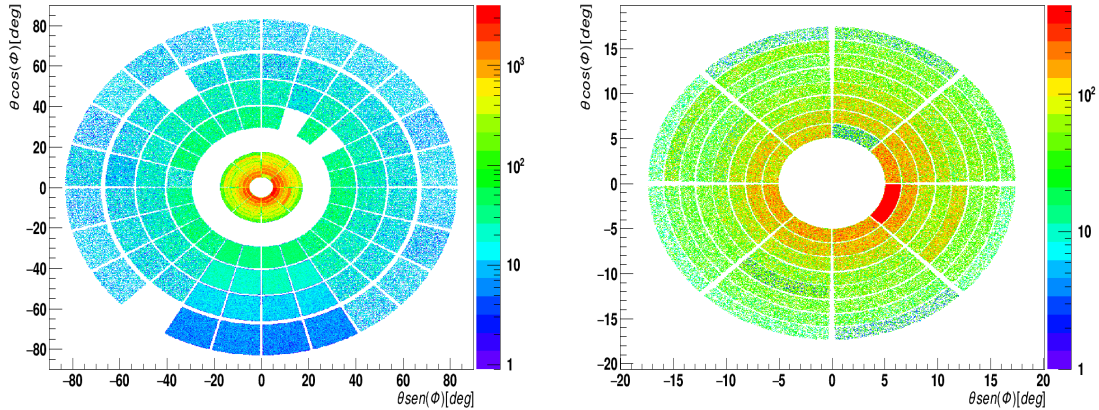


Figure 3.2: Countings for the complete apparatus (GARFIELD + RCo) on the left and for the Ring counter on the right. The figure for RCo is a zoom of the internal crown present on the left. As it can be seen, four GARFIELD detectors are not counting due to bad functioning.

An online control of the acquired data during the measurement sessions was possible due to a graphical interface program named GARFIELD Monitor [39]. This ROOT-based software can visualize several pre-defined 1D and 2D histograms, filled either with raw experimental data or with preprocessed variables. For example, one can have an overall view of the operation of the apparatus by plotting the countings for each separate detector within the apparatus (see Figure 3.2). The GARFIELD Monitor is crucial during the first phase of the measurement as it allows the setting of ADC pedestals and software thresholds. Another parameter kept under close control was the dead time because in this time window the system is inhibited due to the time needed to process the signal. As a consequence, all new events are lost causing an inefficiency in the counting rate. The dead time, throughout which the acquisition system collects the data, has been limited to around 30%-50% by adjusting the beam intensity. The acquisition system is able to measure the dead time by counting all the signals that can be processed over the total number of events hitting the detectors.

To verify the electronic stability of the pre-amplification, from time to time a pulser run is acquired. The pulser is a signal generator that produces pulses similar to the ones generated by the detectors. In this way, one can test the stability and linearity of the gain which may be sensitive to environmental conditions such as temperature variations.

## 3.2 Data Reconstruction and Particle Identification Methods

The acquired data are first processed to obtain the removal of bad signals originated from noise or disturbances that exceed the on-line detection thresholds. In the case of the signals processed by the DSP, this noise removal process is done by imposing specific conditions on the baseline and the maximum of the signal. Considering that 12-bit samples assume values in the range 0-4095, the baseline must lay within a reasonable interval (10-2000) and the maximum of the charge signal must not exceed 4095 (overflow).

A collection of "raw" events is therefore obtained. These are a list of acquisition data parameters characterized by the same event number. The event reconstruction process consists in the analysis of the before mentioned parameters in order to recreate the characteristics of the particles from the detector's signals. Therefore, for every event we reconstructed the multiplicity of particles, each one characterized by its charge, mass (if possible), angular coordinates and its energy loss and/or residual energy. These last two variables are then used to recover the information on the particle's incident energy. Before the energy calibration, the particle must be first of all identified. As mentioned, this means that one has to attribute to each particle a charge value and when possible also its mass. The various identification techniques for our experimental set-up are detailed in the following sections.

### 3.2.1 $\Delta E$ - $E$

The  $\Delta E$ - $E$  identification technique is based on the well-known Bethe-Block expression for the energy loss of a charged particle in an absorber of given density. In particular, in the non-relativistic limit, the energy loss is a function of the particle charge, mass and incident energy [40]:

$$-\left\langle \frac{dE}{dx} \right\rangle \propto \frac{Z^2 A}{E} \quad (3.1)$$

Therefore, the energy loss inside a material increases quadratically with the impinging particle charge and linearly with its mass, while it decreases with energy. Exploiting the dependencies in eq. 3.1, one has the possibility to identify particles by using a sequence of detectors with the requirement that at least one must be entirely crossed by the particle and then stopped in an other detector. Under the assumption that the dependence of the energy loss on the  $E/A$  ratio, is a power law with the exponent left as a free parameter, the Bethe-Bloch expression can be worked out analytically, and therefore one can find a direct relation between the  $\Delta E$  in the first layer of detection and the energy deposited in the second layer. This relation is called a *particle identification function* (PIF). However, experimentally it is quite difficult to find a unique PIF able to linearize the correlation on each telescope of the apparatus by using only one free parameter. Not to mention

that this procedure has to apply to the whole range of residual energies and for a wide range of ion charges. The solution to this issue is to use additional free parameters that take into account possible deviations from the simple Bethe expression. This implies using a phenomenological  $\Delta E$ - $E$  correlation in the event by event identification and a fit of the experimental  $\Delta E$ - $E$  of every available detector to obtain the values of the free parameters [41].

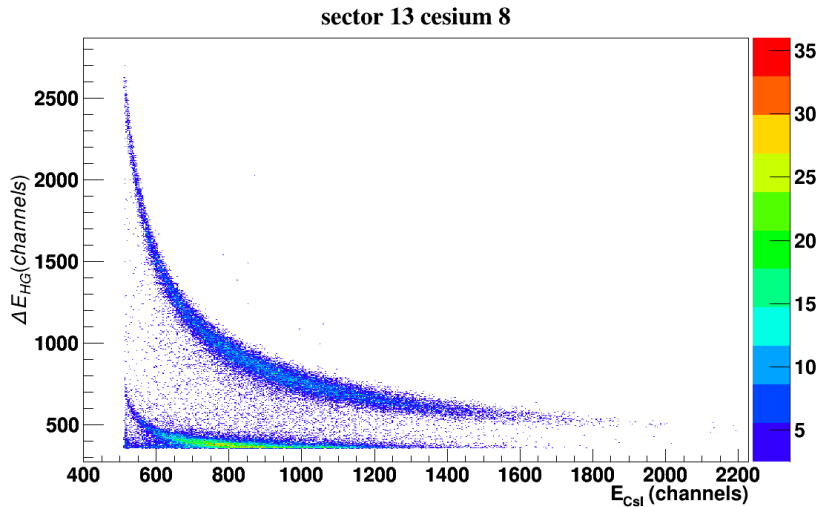


Figure 3.3:  $\Delta E$ - $E$  correlation for sector 13 and Cesium 8 in the GARFIELD apparatus.

For the GARFIELD apparatus, the  $\Delta E$ - $E$  correlation is obtained using the signals coming from the microstrip electrodes (MSGC) and from the Cesium scintillators. In Figure 3.3 is shown such a correlation where a high gain was used to separate  $Z=1$  from  $Z=2$ . In this case, only charge identification is in principle possible, with a threshold of the order of 0.8 AMeV. In the measurement presented in this work, since the maximum charge for the detected particles is  $Z=2$ , this type of correlation is not used for particle identification in GARFIELD as the PSA method from CsI(Tl), which is described in the next section, provides more information (charge and mass) than the  $\Delta E$ - $E$  technique.

In contrast, the  $\Delta E$ - $E$  correlation for the RCo detector is actually used for particle identification and two different  $\Delta E$ - $E$  correlation are feasible. The first is obtained using the  $\Delta E$  extracted from the IC and the energy from the silicon detector when particles are stopped in the latter one. As for GARFIELD, only charge identification (0.8 AMeV threshold) can be achieved with these two stages. The second  $\Delta E$ - $E$  matrix can be built from the Si and CsI(Tl) signals when the particles punch through the silicon strip. In this latter case, also isotopic identification of the detected particles can be obtained. In this measurement, only light particles were sufficiently energetic to cross the first two detection stages and reach the CsI(Tl). An example of the RCo  $\Delta E$ - $E$  matrices are shown in Figure 3.4.

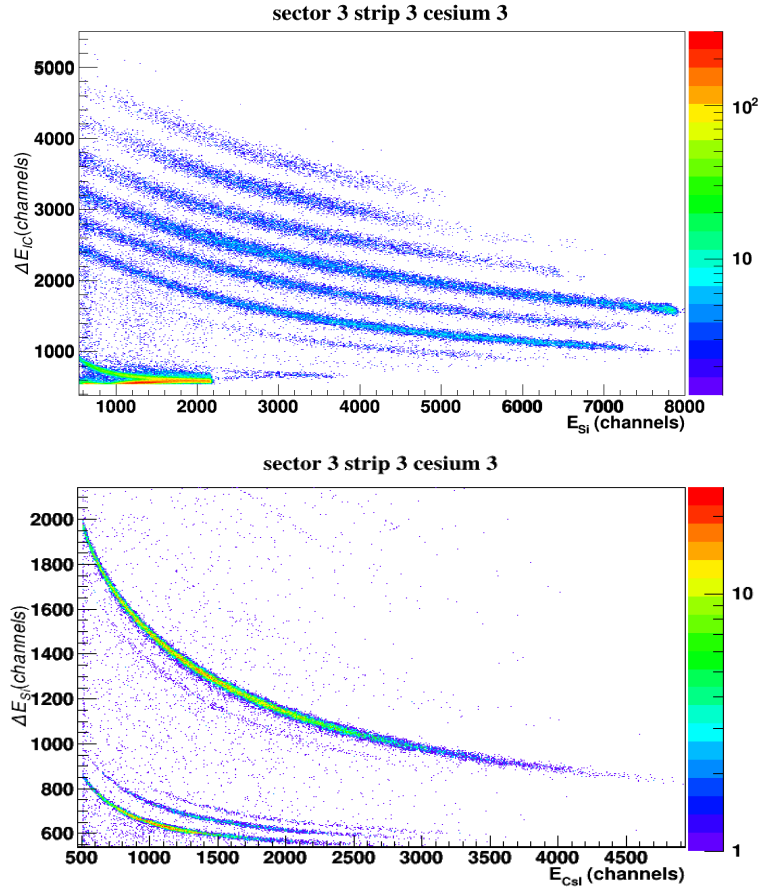


Figure 3.4:  $\Delta E$ - $E$  correlation for IC sector 1 and Si strip 2 (upper panel) and  $\Delta E$ - $E$  correlation for sector 3 Si strip 3 and Cesium 3 (lower panel) in the RCo apparatus. In the upper panel  $Z$  values up to  $Z=10$  are clearly seen, whereas in the lower panel  $p$ ,  $d$ ,  $t$ ,  ${}^3\text{He}$  and  $\alpha$  particles appear.

### 3.2.2 Pulse Shape Analysis

As mentioned in section 2.1.2, the CsI(Tl) scintillators emit light pulses whose shape varies as a function of the type of incident radiation. This characteristic is exploited for particles identification in both Garfield and RCo (when they punch through the  $300\ \mu\text{m}$  silicon detector). The correlation is built between the so-called *fast* and *long* components of the CsI(Tl) signals. These quantities are extracted by the DSP applying two filters with two different time constants to the pre-amplified CsI(Tl) signals. Hence, one is able to disentangle the fast component with a short-gate integration of the signal from the long component which corresponds to the overall integration. To be more specific, the identification procedure shows a better isotopic separation if instead of correlating

the fast with the long, one uses a new parameter obtained from a linear mixing of the two components. In this way, the trivial linear correlation between fast and long, due to the fact that part of the long component is integrated within the short gate, is partially removed. Therefore, the actual correlation is obtained from the fast component and the SlowPSA (spsa) defined as:

$$SlowPSA = 3.5 \cdot (long - 4fast) \quad (3.2)$$

Figure 3.5 shows the fast-spsa scatter plot for a chosen GARFIELD and RCo Cesium Iodide detectors. For the GARFIELD scintillators, the particles can be clearly identified up to  $Z=2$  and for  $Z=1$  also isotopic ridges can be distinguished, corresponding to protons, deuterons and tritons. Lastly, one can notice the presence of  $\gamma$ -rays characterized by a linear dependence between fast and spsa. For the scintillators of RCo, due to higher energy particles also  $Z=2$  isotopes and  $Z=3$  ridges are present. Summarizing, low threshold ( $\simeq 2-4$  AMeV) mass identification of light isotopes (up to  $Z=3$ ) is possible for the Garfield apparatus while for RCo the threshold is of the order of  $\simeq 6$  AMeV due to the preceding  $300 \mu m$  silicon detector.

### 3.2.3 Energy vs Rise-Time

An additional identification method (mass and charge) of the reaction products consists in the application of pulse shape analysis to the signals coming from the Si detectors alone. For a fixed energy of the incident particles, heavier ions tend to create more electron-hole pairs in the first part of the detector and this results in different charge collection time. Therefore, the pulse shapes and the corresponding signal rise time vary with the charge and/or mass of the impinging particle. This charge rise time difference is furthermore enhanced by the reverse mounting configuration of the silicon detectors, so that the particle enters from the low-field side.

In this case, one exploits the correlation between the energy detected in the silicon strip and the rise time of the signal produced by the same detector. This second parameter is defined as the time interval needed for the signal to go from 12.5% to 62.5% of its full amplitude. A typical energy-rise time correlation for a particular Si strip detector is shown in Figure 3.6. The charge identification is easily achieved for all charge products stopped in the silicon detector, with a threshold of about 2.5 AMeV. This value corresponds approximately to the energy needed by the particle to cross the first  $30 \mu m$  of the Si detector. In fact, with decreasing energy, the rise time increases until all ridges merge into the very intense quasi-parabolic structure on the right in Figure 3.6. From this plot, one is also able to identify the elastically scattered  $^{16}O$  ions, clearly visible in the top middle side of Figure 3.6. Furthermore, with the same request of particles stopped in this Si detector, a tip over "v"-like structure can be observed at the end of the corresponding alpha ridge. These alpha particles (graphical cut in Figure 3.6 ) have been identified as

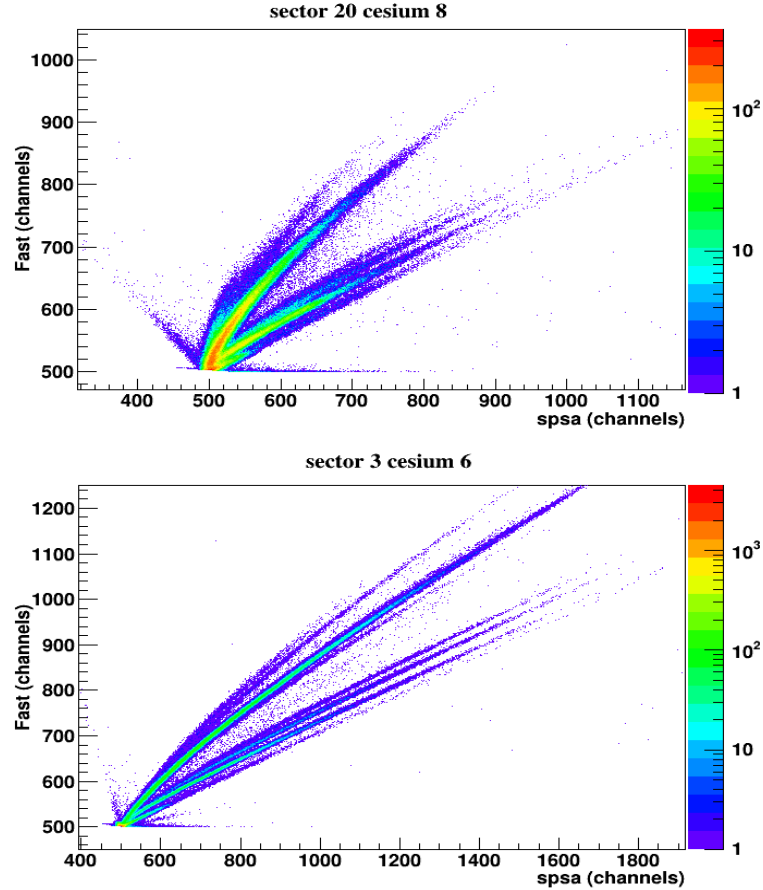


Figure 3.5: Fast vs spsa scatters plots for the Cesium 8 sector 20 of Garfield (upper panel) and for the Cesium 6 sector 3 of RCo (lower panel).

the ones punching through the silicon strip detector and which have not been detected by one of the following corresponding CsI(Tl) detector due to small geometrical mismatches or to the support dead layers between these two detectors. Even though these particular punch through alpha particles are a small percentage with respect to the ones stopped in this silicon stage, we decided to include them in our analysis. Their incident energy was reconstructed using the energy loss tables and treating the detected energy as a  $\Delta E$  loss instead of residual energy.

### 3.2.4 Identification Procedures

In the last sections, we described the three possible identification correlation for the apparatus. Hereafter, we recall first the scheme of the generally employed procedure to identify the reaction products in charge and mass and then we will focus on the details

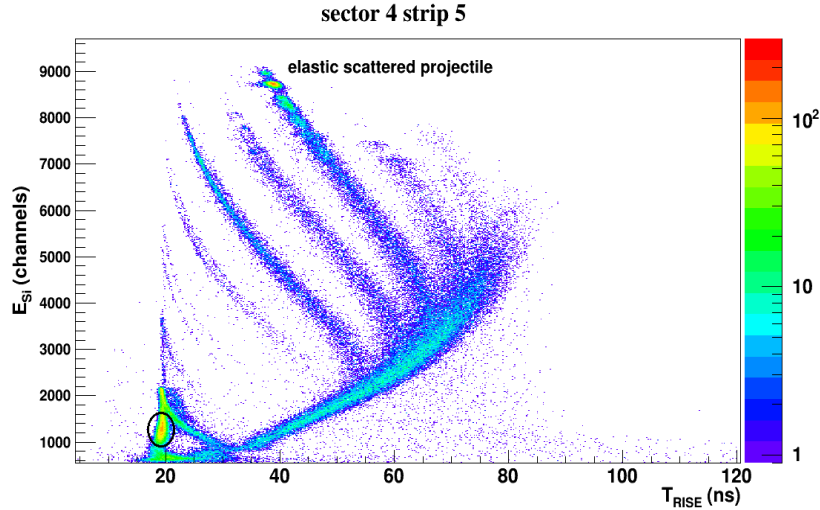


Figure 3.6: Si energy vs. rise time correlation for the silicon detector 5 in sector 4.

of the various methods.

The common steps of the identification procedures are the following:

- to start, in the bidimensional scatter plot several points are sampled by hand on the ridges of well defined isotopes. Generally, these are easy to recognize due to their abundance or their separation from other charges and/or masses as it is the case for example for  ${}^4\text{He}$  and  ${}^{1,2,3}\text{H}$  in Figure 3.4 and 3.5. The charge, mass and coordinates in the scatter plot of these sampled points are saved in a table.
- the characteristic parameters of each detector response to the charge  $Z$  and mass  $A$  are obtained (and stored) by fitting the coordinates of the aforementioned sampled points with the analytical or semi-empirical PIF describing the correlation between the two coordinates.
- the following event by event identification is performed by means of a  $\chi^2$  minimization. For all measured event, isotopes are identified in mass and charge, by minimizing the distance between the measured signals with respect to the values provided by the identification function calculated with the fit parameters of the hit detector. The charge and mass identification is, in general, a two step process: in the first step, charge identification is achieved assuming a mass  $A=2Z$  whereas in the second step the procedure is repeated considering the mass coordinate.

The procedure, as here described, results to be time-consuming in the case of a large number of detectors mainly because the first part requires a huge number of points on each branch to be sampled in order to obtain in the second step a reliable set of parameters. Therefore an automatic or semi-automatic sampling process is highly needed.

One particular example of this will be detailed for the fast-spsa identification procedure [42]. We turn now to see how this procedure is applied to the different correlations available. For the data presented in this work, only fast-spsa scattering plots for GARFIELD and  $\Delta E$ - $E$  or fast-spsa scattering plots for RCo were used in the particle identification process since they are sufficient to identify all the emitted ions and particles. Thus, the details and results of the procedure will be referred mainly to those two mentioned methods.

Starting with the  $\Delta E$ - $E$  for the RCo detector, the previous general procedure was applied using the analytical particle identification function described by [41]:

$$\Delta E = [gE^{\mu+\nu+1} + (\lambda Z^\alpha A^\beta)^{\mu+\nu+1} + \epsilon Z^2 A^\mu (gE)^\nu]^{\frac{1}{\mu+\nu+1}} - gE \quad (3.3)$$

where  $\lambda$ ,  $\alpha$ ,  $\beta$ ,  $\mu$ ,  $\nu$  and  $\epsilon$  are free parameters, related to the characteristics and non-linear effects of the  $\Delta E$  and  $E$  detectors and  $g$  accounts for the ratio of the electronic gains of the two detector's signals. Typical charge and mass distributions obtained from the IC-Si and Si-CsI matrices are shown in Figure 3.7.

In the case of fast-spsa correlation for GARFIELD (and RCO) signals, the semi-automatic procedure, described in details by [42], was used. Hereafter, we will mention a few key points of this procedure. This ROOT based procedure reduces the time dedicated to the manual sampling along the various isotopes ridges with the help of an automatic "tracking" method that samples the Z and A ridges of the fast-spsa scatter plot. The structure of isotope ridges is interpreted as successive monodimensional Gaussian distributions and peaks within these distributions are searched firstly along the X-axis and then along the Y-axis using the ROOT method *Projection* and the *TSpectrum* class [43]. A peak observed on the Y projection is validated only if a peak in the X projections falls in the same cell of the bidimensional plot. This results in a series of coincident peaks, lying on the isotope ridges (see Figure 3.8). The peaks with the same (A, Z) must then be connected to the other ones of the series (called a cluster). In order to do so, a tracking method is used, which is basically a local method of pattern recognition. The propagation of the track starts from a seed, defined as the leftmost point of each cluster, and is based on a local linear equation between each pair of points along the ridge. Moreover, a quality criterion is established as to distinguish good track candidates from ghosts, namely when several points are possible candidates for the trajectory propagation the method selects the point giving the minimum change in the angular coefficient of the straight line between the previous two points of the ridge. The procedure is continued until the end of the tracking area has been reached or no other suitable points are found. Further details on this semi-automatic method are specified in ref. [42].

Once the sampling has been completed, the next operation in the identification procedure is to obtain the fit parameters for the particle identification function. In this case, the proposed function is based on the consideration that a power law relation can be assumed for the total light output (long) of the CsI scintillators as a function of the

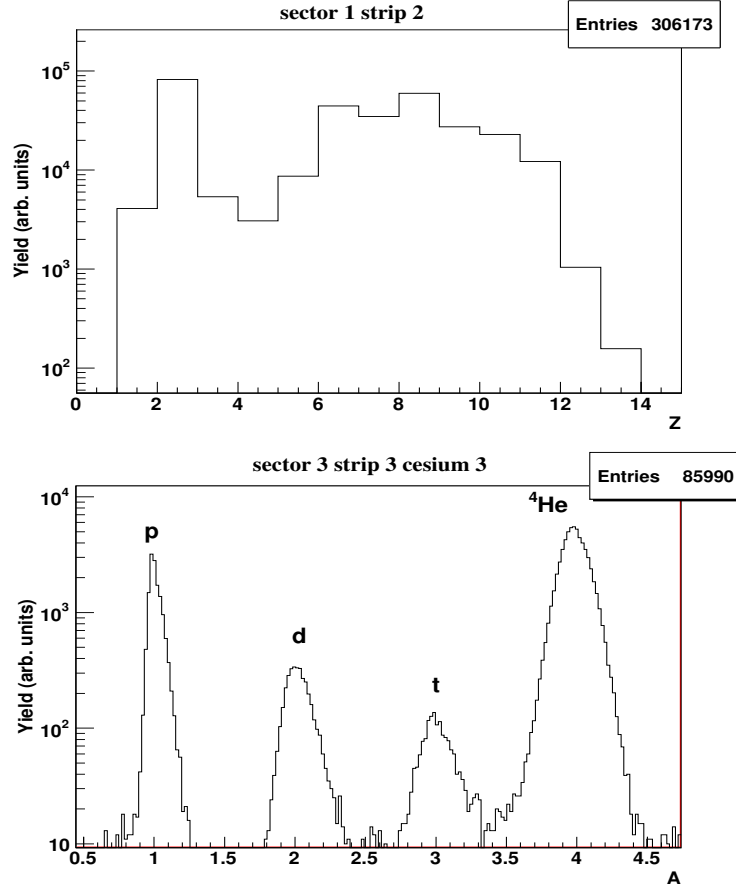


Figure 3.7: Results of the identification procedure on the  $\Delta E-E$  matrices of Figure 3.4 for particles detected in the RCo. The top panel contains the charge distribution obtained from the IC-Si correlation while the bottom panel shows the charge and mass distribution from the Si-CsI correlation. The different identified isotopes (lower panel) are labelled as: protons (p), deuterons (d), tritons (t) and  $\alpha$  particles ( ${}^4\text{He}$ ).

energy [44]:

$$LO(Z_{eff}, E) = (d_1 + d_2 \exp(-d_3 Z_{eff})) (1 + d_4 Z_{eff}) E^{[d_5 - d_6 \exp(d_7 Z_{eff})]} \quad (3.4)$$

Furthermore, due to the almost linear correlation between the fast and the long components, we expect a power law behavior for both fast and spsa variables and also for their mutual dependence. Therefore we can write the following relation:

$$spsa(\text{fast}, A, Z) = a_1 * \text{fast}^{a_2} \quad \text{with} \quad a_1, a_2 > 0 \quad (3.5)$$

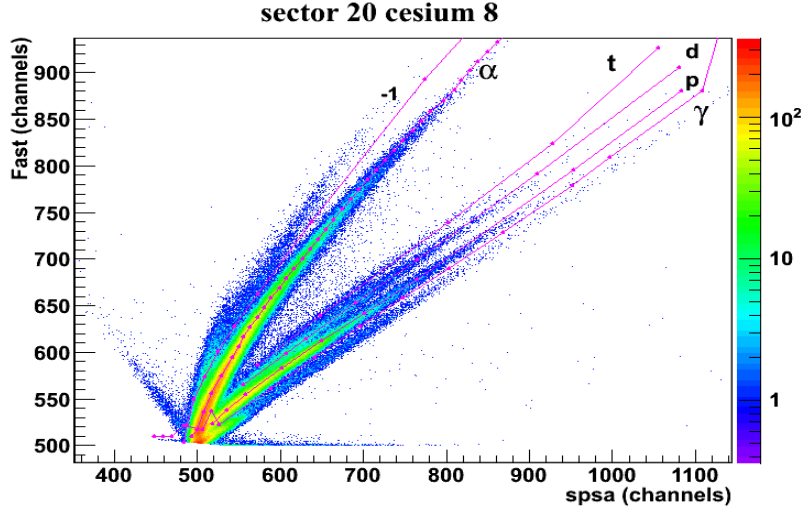


Figure 3.8: Application of the semi-automatic procedure for the particles identification in GARFIELD CsI through the fast-spsa correlation. The figure shows for the various isotope ridges the points determined and connected by the procedure. The lowest red line delimitates the region of gamma rays while the highest (-1) excludes the heavier ions.

where an exponential behavior can be attributed to each of the two parameters  $a_1$  and  $a_2$ :

$$a_1 = [d_1 + d_2 \exp(-d_3 Z_{eff})] \exp(-d_4 Z_{eff}) \quad (3.6)$$

$$a_2 = [d_5 - d_6 \exp(d_7 Z_{eff})] \quad (3.7)$$

The use of  $Z_{eff} = (AZ^2)^{1/3}$  represents the most effective way to take into account the charge and the mass of the analyzed isotope ridges. Lastly, the event by event identification procedure is performed as described in the general case. For each detected particle an integer  $Z$  and a real  $A$  value are attributed by minimizing the distance between the experimental point (spsa, fast) and the analytical function of eq. 3.5 with the free parameters determined by the fit with the sampled points. In Figure 3.9, the results of the identification procedure for a particular CsI of GARFIELD are shown.

### 3.3 Energy Calibration

The next step, given that to a detected particle has been attributed a charge  $Z$  and if possible a mass  $A$ , is to reconstruct the incident energy. In particular, light charged particles detected by GARFIELD (and RCo) CsI(Tl) have been calibrated using the previous analytical function used to fit the sampled tracks in the case of fast-spsa

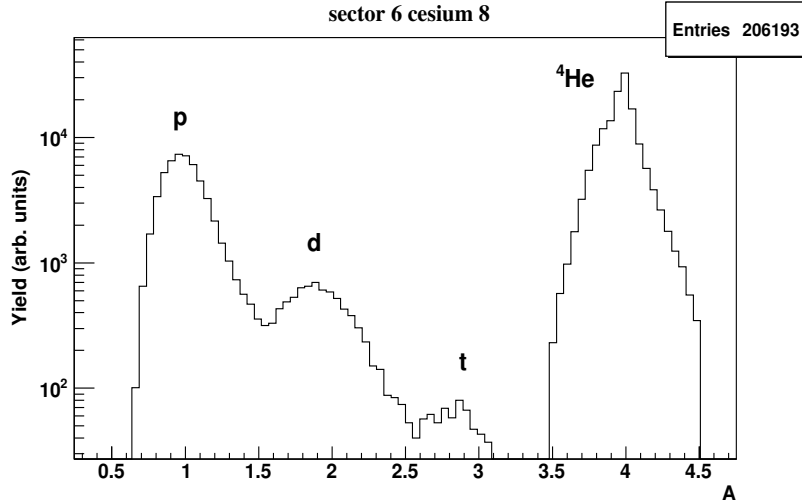


Figure 3.9: Mass distribution obtained for the GARFIELD CsI 8 in sector 6. The different identified isotopes are labelled as: protons (p), deuterons (d), tritons (t) and  $\alpha$  particles ( ${}^4\text{He}$ ).

identification, where a power law relation has been assumed for the total light output as of function of the energy [44]. Instead, for particles identified using the Si strips in RCo, energy calibration has been performed using the elastic scattering measurements of  ${}^{16}\text{O}$  on a gold target, as anticipated in the introduction of this chapter. Since the reaction products are sufficiently energetic to cross the gas layer in both GARFIELD and RCo, the  $\Delta E$  loss in this detection stage is calibrated using energy loss tables from the residual energy of one of the other two mentioned detectors (Si strips or CsI(Tl))

Starting with the former case, the energy calibration of these particles results from the fit of the detector light output (eq. 3.4), provided that we have a sufficient number of points of known energy to constrain the free fit parameters [42]. These points, have been gathered over several years by the collaboration using elastically scattered isotopes ranging from  $Z=1$  to  $Z=28$  detected with CsI(Tl) detectors. This is shown in Figure 3.10, where the signals obtained in the previous measurement for a reference crystal are plotted as a function of the energy. The energy, charge, mass are known either because particles, coming from a well defined beam, were directly elastically scattered on the CsI(Tl) detector or because were identified through a  $\Delta E$ - $E$  technique, exploiting a silicon detector in front of the crystal.

For particles identified by the silicon detector, the energy calibration is possible by employing the several runs of elastically scattered oxygen ions on the gold target. From time to time, generally at the beginning and at the end of the measurements of a particular reaction energy, the mentioned collision was performed once with the IC filled with gas and once empty. For the measurements without the gas, the Si signals correspond to

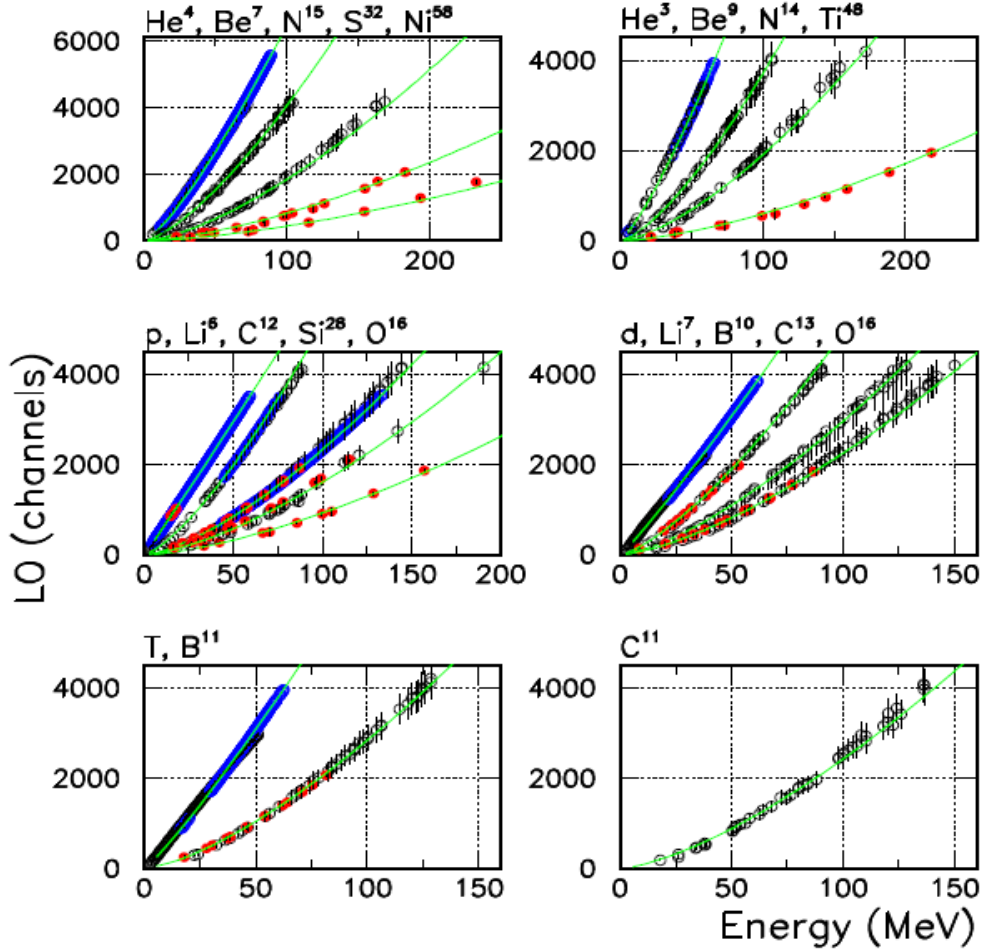


Figure 3.10: Light output (LO) vs E (MeV) for different ions ranging from  $Z=1$  to  $Z=28$ . The points represent the experimental data while colored lines are the analytical function from the fit results.

a well-known energy easily calculated from the Rutherford expression for elastic scattering. Therefore, fitting these experimental points, one can obtain the conversion factor between the energy measured in channels and in eV. The other elastic data, performed with the IC filled with gas, are useful for validating the previous three energy points (90.5, 110 and 130 MeV). In this case, their calculated energy is scaled by taking into account also the initial gas layer positioned before the Si strip detector. In Figure 3.11 the calibration curve including all the elastic scattering points is shown. As we expected for a Silicon detector, these points follow a linear trend for the energy calibration curve meaning that non-linear effects, due to the possible bad functioning of the electronics, are not present.

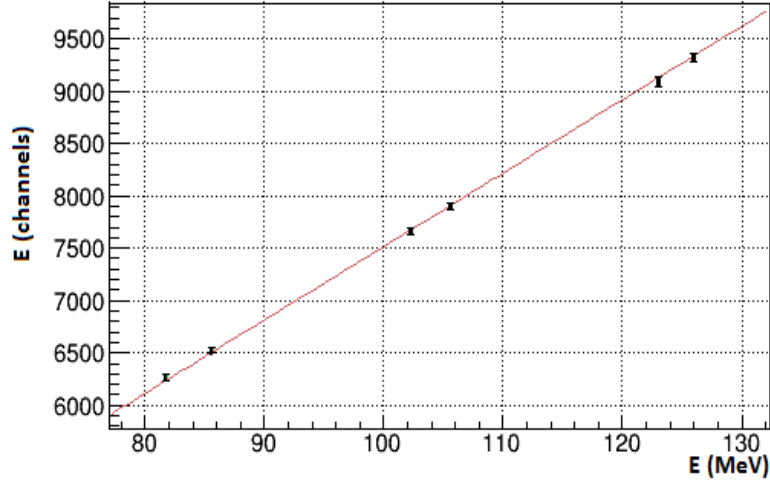


Figure 3.11: Fit procedure on the elastic scattering points, with and without the gas in the IC, for strip 5 in sector 3 [45].

### 3.4 Experimental Observables and Data Reduction

After the identification and calibration procedures, one has a set of observables associated either with each single particle or with the global reconstructed event. To this latter category belong global variables such as the event charged particle multiplicity and the charge distribution. The multiplicity represents the number of particles detected in each event and depends experimentally on the angular coverage of the apparatus. On the other hand, the charge distribution of the reaction products displays the relative yield of the different charges emitted in the collision. Both these quantities can be connected to the type of reaction mechanism.

From an experimental point of view, another important observable is the sum of the detected charge ( $Z_{tot}$ ) as it gives information on the actual efficiency of the apparatus. In fact, on an event by event basis one is able to reconstruct the total charge and to compare the detector's response to the known charge in the entrance channel. This quantity will be particularly useful when we will select complete or quasi-complete events, namely  $Z_{tot} = 14$  or  $Z_{tot} > 10$  in the case of the currently studied reaction. For the study of the compound formation, an interesting observable is the charge distribution of the detected residue ( $Z_{big}$ ). This value can be used to select afterwards a particular decay channel which may contain specific information, as for example clustering effects. An example of a typical  $Z_{big}$  distribution, obtained in the  $^{16}O + ^{12}C$  reaction, is shown in Figure 3.12. The  $Z$  distributions for the reaction will be discussed more in detail in Chapter 5.

The reaction mechanism can be furthermore constrained by using the correlation between the total detected charge in an event and the total longitudinal momentum.

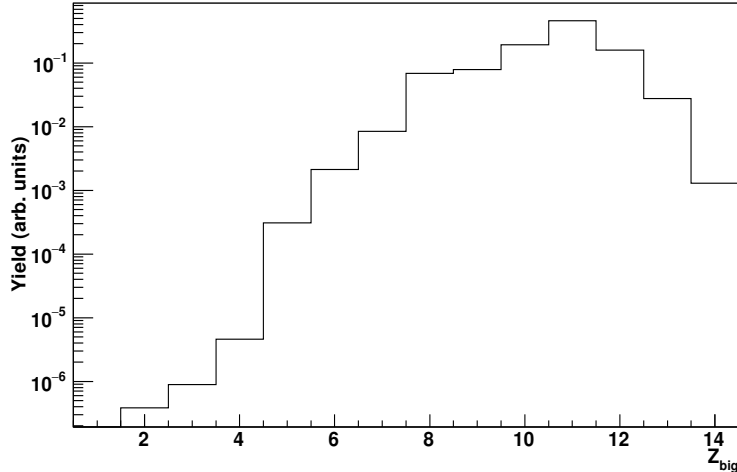


Figure 3.12: The  $Z_{big}$  distribution obtained for the  $^{16}O+^{12}C$  reaction at 90.5 MeV.

To be more specific, because of total momentum conservation, the total longitudinal momentum associated to a fused system will be close to the one of the incident projectile while the total detected charge will be much higher than for peripheral events. Indeed for peripheral events the total charge is much lower since the quasi-target particles are not detected due to the velocities under the thresholds. The scatter plot of the total collected charge  $Z_{tot}$  versus the ratio between the total momentum projection along the beam axis and the initial momentum ( $p_z/p_{beam}$ ) is shown in Figure 3.13. One can clearly notice different peak yield regions and in particular a very intense zone around  $Z=8$  and  $0.8 < p_z/p_{beam} < 1$ , corresponding to the before-mentioned (quasi)-elastic events with only the Oxygen ejectile detected, is evident. These type of correlations are used for every energy of the reaction as the starting point in the final analysis described in Chapter 5.

Even after the first initial data processing, some spurious events remained. These events correspond to a total collected charge larger than the one of the initial system ( $Z_p + Z_t$ ) and/or the total momentum larger than the initial projectile momentum  $p_{beam}$ , as it can be seen in Figure 3.13. Therefore, for the final analysis one has to remove the events with  $Z_{tot} \geq 15$  and  $p_z/p_{beam} > 1.1$ . The events contained in this cut are only a very small part, representing less than 1% of the total experimental data shown in the correlation plot of Figure 3.13. We allowed for a 10% excess of  $p_z$  to take into account both ion mass uncertainties and effects of energy resolution.

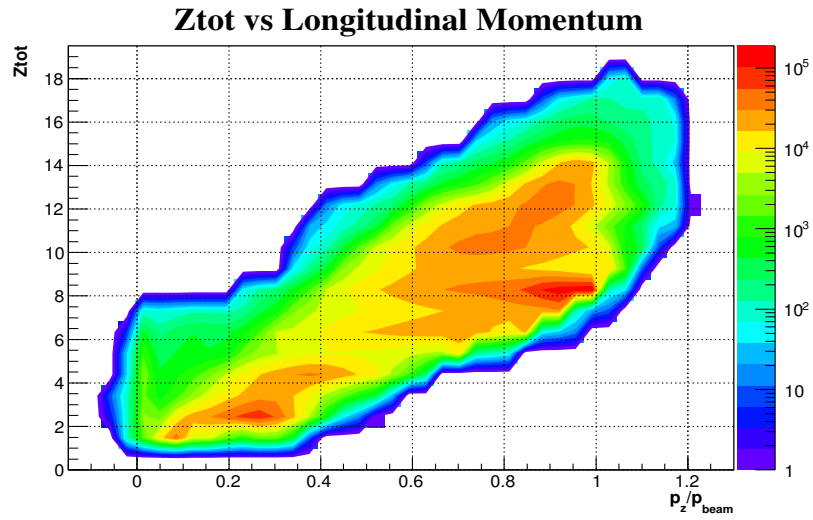


Figure 3.13: The  $Z_{tot}$  vs the  $p_z/p_{beam}$  correlation for the  $^{16}O+^{12}C$  reaction at 130 MeV.

# Chapter 4

## The Hauser-Feshbach Statistical Decay Code

This chapter contains a general description of the Monte Carlo Hauser-Feshbach code that has been developed in the framework of the NUCL-EX collaboration for the practical application to the problem of sequential evaporation of the compound nucleus. Previously, in chapter 1, we have shown the basic standard statistical model. Hereafter, we will detail and extend some of the simple assumptions regarding the form of the key ingredients for the calculation of the branching ratio for the decay channels. In particular, we will describe the complete expression for the decay width in a particular channel for the CN and the choice of the realistic parametrizations for the nuclear Level Density (LD). The latter has been highly constrained to experimental data and also includes all available experimental information on low-energy excitation spectra. In this way, the newly developed code is addressed to perform calculations for the decay of equilibrated light nuclei, for which one expects a strong influence of nuclear structure effects even at high excitation energy as it is the case for the reaction studied in this thesis.

### 4.1 Monte-Carlo Implementation of the Decay Model

The complete expression for the decay width in channel  $\xi$  for a compound nucleus in its state  $C$  (specified by the energy  $E^*$  and the angular momentum  $J$ ) in the Hauser-Feshbach statistical decay model reads:

$$\Gamma_{\xi}^C = \frac{1}{2\pi\rho_C(E^*, J)} \cdot \int_0^{E^*-Q} d\epsilon_{\xi} \sum_{J_d} \sum_{j=|J-J_d|}^{J+J_d} \sum_{l=|j-s_p|}^{j+s_p} T_{j,s_p}^J(\epsilon_{\xi}) \cdot \rho_d(E^* - Q - \epsilon_{\xi}, J_d) \quad (4.1)$$

where  $\epsilon_{\xi}$  is the relative kinetic energy of the decay products, namely the daughter nucleus labelled by the "d" subscript and the evaporated particle labelled by "p".  $Q$  represents

the decay Q-value while  $J_d$ ,  $s_p$  and  $l$  are the angular momentum of the daughter nucleus, the spin of the emitted particle and the orbital angular momentum of the decay. Lastly,  $T$  is the transmission coefficient whereas  $\rho_C(E^*, J)$  and  $\rho_d(E^* - Q - \epsilon_\xi, J_d)$  are the nuclear LD of the decaying nucleus and of the daughter nucleus, respectively. A simple analytical expressions can be employed for light compound nuclei and in the code, the expression for the transmission coefficients is implemented as in the work of [46]:

$$T_l(\epsilon_\xi) = \frac{1}{1 + \exp\left(\frac{V_b - \epsilon_\xi}{\delta \cdot V_b}\right)} \quad (4.2)$$

where the barrier  $V_b$  is the sum of a Coulomb and a centrifugal term depending on  $l$ . Its full expression reads:

$$V_b = \frac{1.44}{r_Z} \frac{Z_p(Z - Z_p)}{(A - A_p)^{1/3} + A_p^{1/3}} + \frac{\hbar l(l + 1)}{2r_Z^2} \frac{\frac{A}{A_p(A - A_p)}}{\left[(A - A_p)^{1/3} + A_p^{1/3}\right]^2} \quad (4.3)$$

The two free parameters  $\delta$  and  $r_Z$  were optimized to reproduce the decay of discrete resonances [46].

With the aforementioned parameters, and the phenomenological LD which we will describe in the next section, eq. 4.1 allows calculating the widths  $\Gamma_\xi^C$  for all the possible decay channels and therefore the Branching Ratio associated to a particular channel  $\xi$ :

$$BR^C(\xi) = \frac{\Gamma_\xi^C}{\sum_i \Gamma_i^C} \quad (4.4)$$

This quantity simply represents the probability for the excited CN to decay via the  $\xi$  channel, as already stated in chapter 1 when we overviewed the emission probability in the much simpler classical case. The Hauser-Feshbach decay probability, shown in eq. 4.1, constitutes the main ingredient of the Monte-Carlo simulation. It is important to notice that only the LD of the daughter nucleus  $\rho_d(E^* - Q - \epsilon_\xi, J_d)$  is relevant for the BR calculation since the factor  $1/2\pi\rho_C$  is the same both in the numerator and denominator of eq. 4.4. The decay channels implemented in the code are the evaporation of light particles or of a charged fragment (always in their ground state) like: n, p, d, t,  ${}^3\text{He}$ ,  $\alpha$ ,  ${}^6\text{Li}$ ,  ${}^7\text{Li}$  and  ${}^8\text{Be}$ . The code does not contain an implementation of the  $\gamma$ -emission as it was assumed that above particles emission thresholds this process is not competitive with respect to charged particle decay. Moreover, even if  $\gamma$  unstable levels (part of the simulation database) under the threshold for particle emission are populated, their further decay does not modify the isotopic yields.

The decay chain starting from the initial hot source is stopped whenever an excitation energy lower than the particle emission threshold (the decay Q-value) for the evaporation residue is reached. In the code, these thresholds are calculated from experimental binding

energies taken from the Audi and Wapstra online database [47]. Therefore, a complete decay chain is defined as a series of successive binary decays, in which at each step a new decaying source is formed, inheriting the characteristics of the evaporation residue of the previous step. These characteristics, such as mass, charge, excitation energy and angular momentum, come from the usual conservation laws.

Once the decay channel is selected by the Monte-Carlo according to its weight  $BR^C(\xi)$ , the relative kinetic energy of the emitted particle and the evaporation residue is extracted from the same distribution integrated for the calculation of the branching ratio. The extraction of a  $\epsilon_\xi$  value according to its distribution is performed with the acceptance-rejection method. Subsequently, one checks if the ER is left with a residual excitation energy such that a discrete level of its spectrum is populated. To do so, the code accesses at each decay step a database containing all the information concerning the discrete experimental levels. This information was obtained from the online archive NUDAT2 [48].

## 4.2 The Level Density Model

The choice of the level density model, as stated in the previous section, has to include in a coherent way all the available experimental information on the low energy discrete spectra. Within a phenomenological approach, the back-shifted Fermi gas model (BSFG) is able to well reproduce the many-body correlated nuclear level density. This model includes only two free fit parameters: the LD parameter  $a(E^*)$  and the pairing backshift parameter  $E_2$ . In ref. [49] it is shown that the BSFG model also allows an excellent fit of the complete low-lying level schemes. Therefore, with this in mind, one is interested in studying a functional form that can be used to describe the nuclear LD at any excitation energy, provided that one is able to match correctly the low and high energy regimes.

The level density model implemented in this Monte-Carlo simulation is the one presented by [49], where the free parameters for the BSFG model have been determined for 310 nuclei (from  $^{18}F$  to  $^{251}Cf$ ) from the fit of complete level schemes at low excitation energies and  $s$ -wave neutron resonances spacings at the neutron binding energies. Moreover, the formulas proposed by [49] provide a reliable extrapolation of the LD parameters of exotic nuclei or of the nuclei which are not part of the studied data set. The adopted expression for  $\rho(E^*)$ , after integration on  $J$  and  $\pi$ , is given by:

$$\rho(E^*) = \frac{\exp[2\sqrt{a(E^* - E_2)}]}{12\sqrt{2}\sigma a^{1/4}(E^* - E_2)^{5/4}} \quad (4.5)$$

where  $\sigma$  is the spin cut-off parameter:

$$\sigma^2 = 0.0146A^{5/3} \frac{1 + \sqrt{1 + 4a(E^* - E_2)}}{2a} \quad (4.6)$$

and here also the backshift  $E_2$  and the LD parameter  $a(E^*)$  enter in the calculation of  $\sigma$ . For the latter parameter, a phenomenological expression, proposed by [50], has been chosen. This particular energy dependence parametrization is able to reproduce the damping of shell and pairing effects at high excitation energies:

$$a(E^*, Z, N) = \tilde{a} \left[ 1 + \frac{S(Z, N) - \delta E_p}{E^* - E_2} (1 - e^{-0.06(E^* - E_2)}) \right] \quad (4.7)$$

where  $S(Z, N) = M_{exp}(Z, N) - M_{LD}(Z, N)$  is the shell correction term.  $M_{exp}(Z, N)$  and  $M_{LD}(Z, N)$  are the experimental mass and the mass calculated with a macroscopic liquid drop model for the binding energy which does not consider any pairing or shell correction terms.  $\delta E_p$  is a pairing factor expressed in terms of the deuteron separation energy:

$$\delta E_p = \begin{cases} +0.5P_d & \text{for even - even} \\ 0 & \text{for odd - A} \\ -0.5P_d & \text{for odd - odd} \end{cases} \quad (4.8)$$

where:

$$P_d = \frac{1}{2}(-1)^Z [S_d(A + 2, Z + 1) - S_d(A, Z)] \quad (4.9)$$

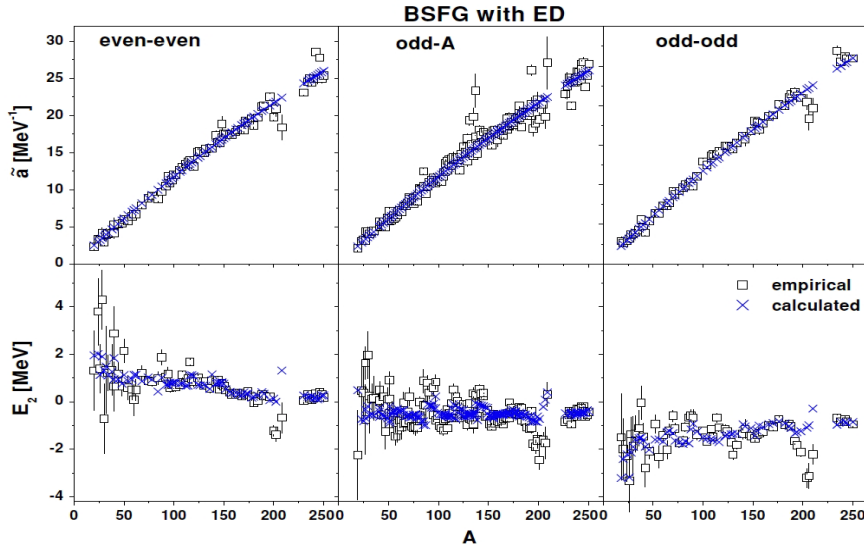


Figure 4.1: Fits to the BSFG model of the parameters  $\tilde{a}$  and  $E_2$  obtained with the empirical formulas reported in [49].

As a result of the fit procedure (see Figure 4.1), the authors in [49] provide a complete table of values for the empirical parameters  $\tilde{a}$  and  $E_2$  for all the nuclei studied. These results are then introduced in eq. 4.5 and a good overall reproduction of the experimental distributions of measured levels can be observed. A few example are illustrated in Figure 4.2, where a comparison between the cumulative distribution of the number of levels, calculated from eq. 4.5, and the cumulative counting of experimentally measured levels from the NUDAT2 database is shown. The figures include the  $^{12}\text{C}$  and  $^{16}\text{O}$  isotopes where the values of the  $\tilde{a}$  and  $E_2$  parameters are an extrapolation of the formulas proposed in [49] out of the fitted data set. It can clearly be seen that the LD density parametrization turns out to be reliable also for nuclei whose LD has not been directly optimized, as anticipated at the beginning of this section. Nevertheless, as stated by the authors of [49], the proposed model is considered trustworthy only up to energies of 15-20 MeV for nuclei with  $A \approx 20$ . In fact, it is found that the values of the LD parameter  $a(E^*)$  which well reproduce the discrete levels information are normally lower than the one coming from fusion-evaporation data or evaporation-after-fragmentation studies at higher energies.

Therefore, the HF $\ell$  Monte-Carlo code developed by [2] inside the NUCL-EX collaboration contains an expression for the  $a(E^*, Z, N)$  which is able to match the previous formula (at low energy) also with the higher energy regime. For the high excitation energy case, the following functional form was used [51]:

$$a_\infty = \frac{A}{14.6} \left( 1 + \frac{3.114}{A^{1/3}} + \frac{5.626}{A^{2/3}} \right) \quad (4.10)$$

in which no energy dependence is present but a more complicated mass dependence is included. Combining eq. 4.7 and eq. 4.10 with a continuous interpolation between the two energy regimes, the following functional form for the LD parameter was adopted:

$$a(E^*, A) = \begin{cases} a_D = \tilde{a} \left[ 1 + \frac{S(Z,N) - \delta E_p}{E^* - E_2} (1 - e^{-0.06(E^* - E_2)}) \right] & \text{if } E^* \leq E_m + E_2 \\ a_C = \alpha \exp[-\beta(E^* - E_2)^2] + a_\infty & \text{if } E^* > E_m + E_2 \end{cases}$$

A rapid exponential increase of  $a_C$  is imposed due to the fact that the value of  $a_\infty$  is connected to a sharp threshold process, namely the opening of the break-up or multifragmentation channels. The  $\alpha$  and  $\beta$  parameters are constrained by the matching conditions between the low energy and high energy regimes:

$$a_D(E_m, A) = a_C(E_m, A) \quad (4.11)$$

$$a_C(E_l, A) = a_\infty \pm 10\% \quad (4.12)$$

where  $E_l$  represents the limiting energy at which the break-up or fragmentation regime is attained while  $E_m$  is the excitation energy marking the transition between the discrete and the continuum part of the excitation spectrum. The former is left as a free parameter of the calculation and governs the rapidity of the variation of  $a(E^*)$  above  $E_m$ . During

the past experiments this value was varied and the functional form of the LD parameter for different values of the  $E_l$  was studied [2]. In particular, for our analysis, the value of the limiting energy is fixed to 3 AMeV as this was observed to give good results for a similar reaction [2] in the case of  $A < 40$  nuclei. The latter is fixed to a value of the order of  $E_m \approx 10$  MeV coherently with the value of the critical energy for the damping of pairing effects [52]. Beyond this critical energy, the LD parameter is assumed to be independent of structure effects.

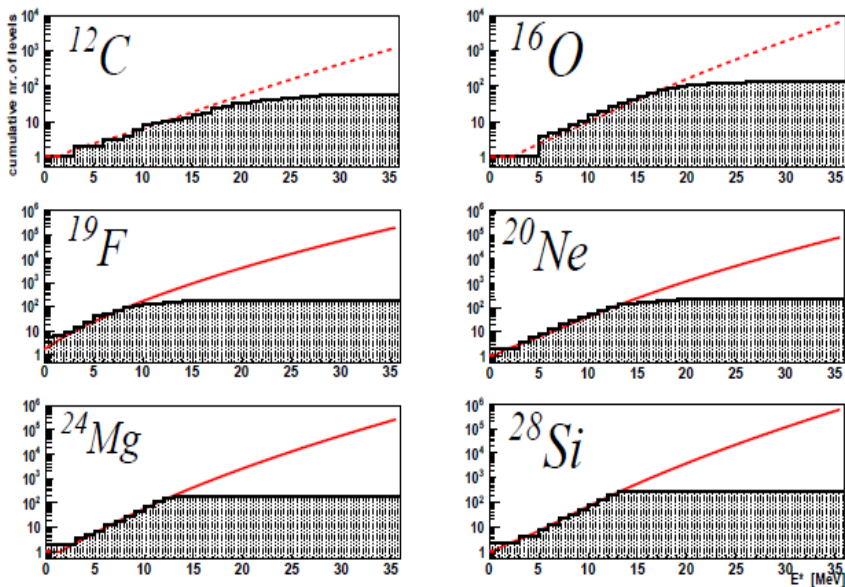


Figure 4.2: Comparison between the cumulative number of levels given by eq. 4.5 (red line), and the cumulative counting of measured levels from NUDAT2 (histograms).

### 4.3 Treatment of the Angular Momentum

The treatment of the angular momentum represents the progress of the standard Weisskopf approach in the new statistical evaporation model of the Hauser-Feshbach formalism. The implementation is based on a semi-classical approach already used by the GEMINI++ [53] model where angular momenta are treated as classical vectors. In the fusion reaction the angular momentum  $\vec{J}$  of the CN is the result of the different couplings of the momenta in the entrance channel. In fact, these are due to the different possible configuration of the spin of the target and of the projectile and to the orbital angular momentum between the incoming particles. Similarly, at every evaporation step, a decomposition of the initial  $\vec{J}$  of the decaying source into the different components is

performed by taking into account the conservation of the total angular momentum:

$$\vec{J} = \vec{J}_d + \vec{j} \quad (4.13)$$

$$\vec{j} = \vec{l} + \vec{s}_p \quad (4.14)$$

This means that the orbital angular momentum of the decay  $\vec{l}$  and the spin of the emitted particle  $\vec{s}_p$  are coupled to the vector  $\vec{j}$ , and the daughter nucleus can be left with every possible value of its angular momentum  $J_d$  coming from the coupling of  $\vec{J} - \vec{j}$ . At this point, it is assumed that all values of  $j$  and  $l$  are equally probable in the ranges:

$$|J - J_d| \leq j \leq |J + J_d| \quad (4.15)$$

$$|j - s_p| \leq l \leq |j + s_p| \quad (4.16)$$

so that one can randomly select the module of the  $\vec{j}$  and  $\vec{l}$  vectors in these intervals. However, the angular momentum of the daughter nucleus after a first decay stage may differ from its ground state spin, since the residual nucleus can still be excited. In general, an upper limit  $J_{limit}$  for the angular momentum of a given evaporation residue with excitation energy  $E^*$  is determined by the Yrast line limitation, namely  $E^* \leq E_{yrast}^*$  with:

$$E_{yrast}^* = \frac{J_{limit}(J_{limit} - 1)\hbar}{2I_d} \quad (4.17)$$

where  $I_d$  represents the moment of inertia of the daughter nucleus. On the other hand, the lowest value the angular momentum can assume has to be either 0 or 1/2 depending on the residue being an even- or odd-A nucleus. For a selected decay channel, the angular momentum  $J_d$  is obtained through a maximization of the  $\rho_d(J)$  as a function of  $J$ . Our analysis of the reaction is based on the assumption of a triangular distribution for the initial angular momentum of the CN issued in the case of complete fusion. The input maximum for the  $J$  distribution, which better reproduces the systematics of the fusion cross section, is  $J = 17\hbar$  with a diffuseness parameter of the distribution of  $\Delta J = 2$  to account for the fact that the real  $J$  has a smooth distribution rather than a sharp threshold distribution like the triangular one (see Figure 1.1).

## 4.4 Correlation Function

As it was stated in this chapter, the implementation of the HF $\ell$  decay model includes discrete levels which can be populated in the decay chain. In particular, for light nuclei ( $3 < Z < 8$ ), their discrete spectrum is quite extended which implies that the last evaporation step generally takes place from a discrete resonance. The information on these discrete levels of hot nuclei can be accessed, backtracing the last but one step of the

decay, by means of the correlation function technique in relative kinetic energy of coincident pairs of fragments. For this purpose, the measurements have to be carried out with detectors having good energy resolution and high granularity.

The two particle correlation function ( $1 + R(\epsilon_{rel})$ ) may be defined as [54]:

$$\sum_{(\vec{p}_1 - \vec{p}_2)^2 / 2\mu = \epsilon_{rel}} Y_{12}(\vec{p}_1, \vec{p}_2) = C[1 + R(\epsilon_{rel})] \cdot \sum_{(\vec{p}_1 - \vec{p}_2)^2 / 2\mu = \epsilon_{rel}} Y_1(\vec{p}_1)Y_2(\vec{p}_2) \quad (4.18)$$

where  $Y_{12}$  is the two particle coincident yield of a given pair of particles with momenta  $\vec{p}_1$  and  $\vec{p}_2$ , respectively. Instead,  $Y_i(\vec{p}_i)$  represents the single particle yields for the two particles measured under the same analysis selection but belonging to a different event. The summations on both sides of the eq. 4.18 run over pairs of momenta  $\vec{p}_1$  and  $\vec{p}_2$  corresponding to the same bin in relative kinetic energy. The correlation constant is generally chosen as the ratio between the total (integrated over momentum) number of generated mixed events and the total number of coincident yields:  $C = \sum Y_{12} / \sum(Y_1 Y_2)$  as to normalize the correlation function to the number of particles pairs.

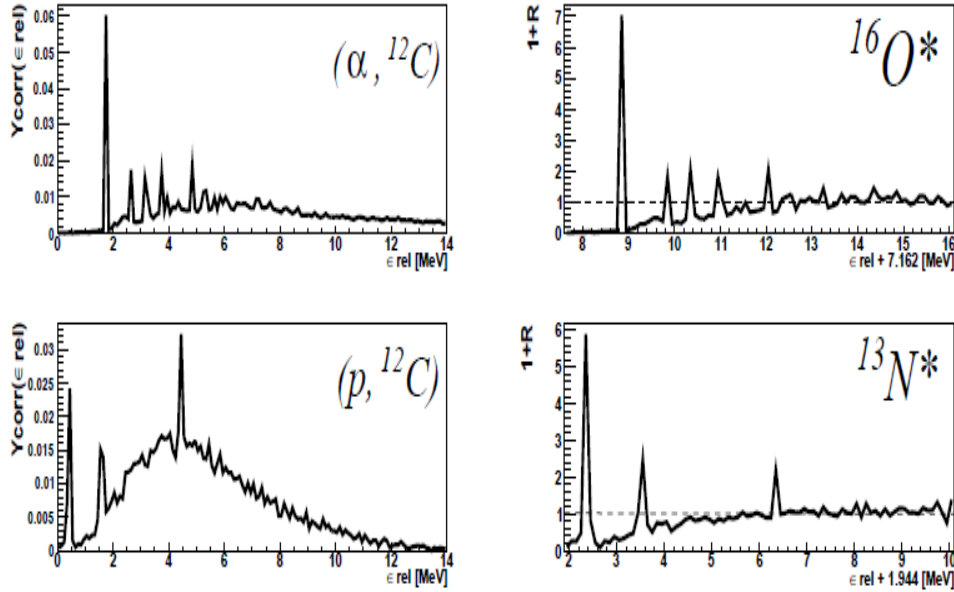


Figure 4.3: Relative kinetic energy distribution (left) for the  $(\alpha, {}^{12}C)$  and  $(p, {}^{12}C)$  pairs. Normalization is to the total number of coincident pairs. On the right are shown the corresponding correlation function, given as a function of the excitation energy ( $\epsilon_{rel} + Q$ -value) for the parent nucleus [2].

Therefore, with this in mind, eq. 4.18 can be simply written also as:

$$1 + R(\epsilon_{rel}) = \frac{\sum_{\epsilon_{rel}} Y_{corr}(\epsilon_{rel})}{\sum_{\epsilon_{rel}} Y_{uncorr}(\epsilon_{rel})} \quad (4.19)$$

where now  $Y_{uncorr}(\epsilon_{rel})$  represents the uncorrelated background calculated by the event mixing technique [54]. The correlation function describes overall how the correlation between interacting particles measured in the same event differs from the underlying two particle phase space. In Figure 4.3 are presented two correlation function examples for the decay of the  $^{24}Mg$  for HF $\ell$  [2]. One can clearly distinguish discrete states (ground and bound excited ) for the two excited nuclei ( $^{16}O$  and  $^{13}N$ ) produced along the decay chain for the  $^{24}Mg$  compound nucleus.

# Chapter 5

## Data Analysis and Results

This chapter contains the data analysis, performed after the previous identification and calibration procedures, and the results obtained. These preliminary results are the first ones obtained for the  $^{16}\text{O}+^{12}\text{C}$  reaction by the NUCL-EX collaboration. The goal is to identify possible channels of interest for a more detailed future study.

Having three energies at our disposal, the comparison between the results obtained for each one can give an indication of the energy dependence of some specific observables. Furthermore, a comparison between the data and the Hauser-Feshbach model, described in Chapter 4, can indicate if the data are compatible with a statistical decay. If it is not the case, deviation of the experimental data from the statistical evaporation model could be a signature of structure or clustering effects. Before being able to compare the data and the HF $\ell$  simulation, one must filter the HF $\ell$  output by applying, via software, a Monte-Carlo simulation of the apparatus. This software simulation mainly covers the following key points:

- takes into account the geometrical efficiency of the experimental apparatus by eliminating particles generated at angles not covered by the detectors.
- includes dead layer energy loss for the emitted particles.
- includes detection and identification thresholds and energy fluctuations reproducing the experimental energy resolution.

For a first selection of the measured fusion-evaporation events we made use of the total detected charge as a function of the total longitudinal momentum, already discussed and described in section 3.4, shown in Figure 5.1 with the applied cuts. We will first show some global variables (charge distribution, proton and  $\alpha$  particles multiplicity and energy distributions) obtained with a loose cut on the total detected charge and the total momentum, *i.e.*  $10 < Z_{tot} < 15$  and  $0.6 < p_z/p_{beam} < 1.1$ . From now on, we will refer to this condition as Quasi-Complete charge detection (QC). Secondly, the distributions of the

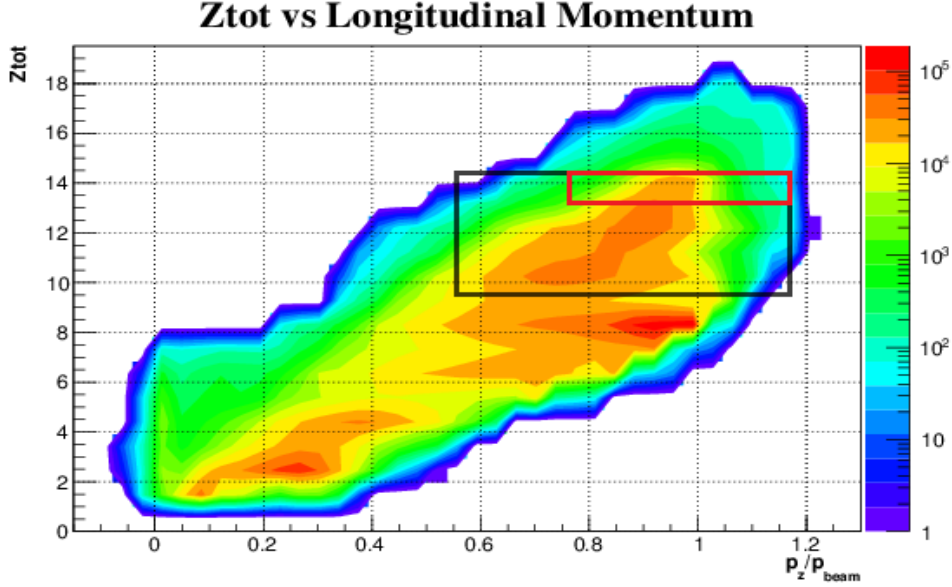


Figure 5.1: The  $Z_{tot}$  vs the  $p_z/p_{beam}$  correlation for the  $^{16}O+^{12}C$  reaction at 130 MeV. The black solid line represents the Quasi-Complete condition ( $10 < Z_{tot} < 15$  and  $0.6 < p_z/p_{beam} < 1.1$ ) while the red line shows the more stringent condition on the total charge detection and the total momentum ( $Z_{tot} = 14$  and  $0.8 < p_z/p_{beam} < 1.1$ )

aforementioned variables will be compared with the ones obtained from a more stringent condition on the total charge detection and the total momentum, which for the investigated system in these reactions is  $Z_{tot} = 14$  and  $0.8 < p_z/p_{beam} < 1.1$ . This comparison is necessary since in the second part of the analysis we would like to concentrate on specific channels and therefore require a complete charge detection. If the distributions are not largely affected by the latter condition, the characteristics of the events are very similar to the ones with the former condition. If this is the case, we can focus our attention on a few particular channels, imposed by selecting the evaporation residue and the decay mode, which may reveal evidence of structure or clustering effects.

Beam Energy (MeV)	$\sigma_F$ (mb)	$E_{CN}^*$ (MeV)	CN recoil velocity (cm/ns)
90.5	887	55	1.884
110	841	63	2.083
130	810	72	2.264

Table 5.1: Fusion cross section estimates for the different energies of the  $^{16}O+^{12}C$  reaction and general characteristics of the formed compound nucleus (CN) calculated by the PACE4 code.

In Table 5.1, the estimated fusion cross section for each energy of the reaction are

reported. These were calculated by the PACE4 code [55] using the Bass model [56] for the optical potential parameters. The same code, used to obtain the values for  $\sigma_F$  in

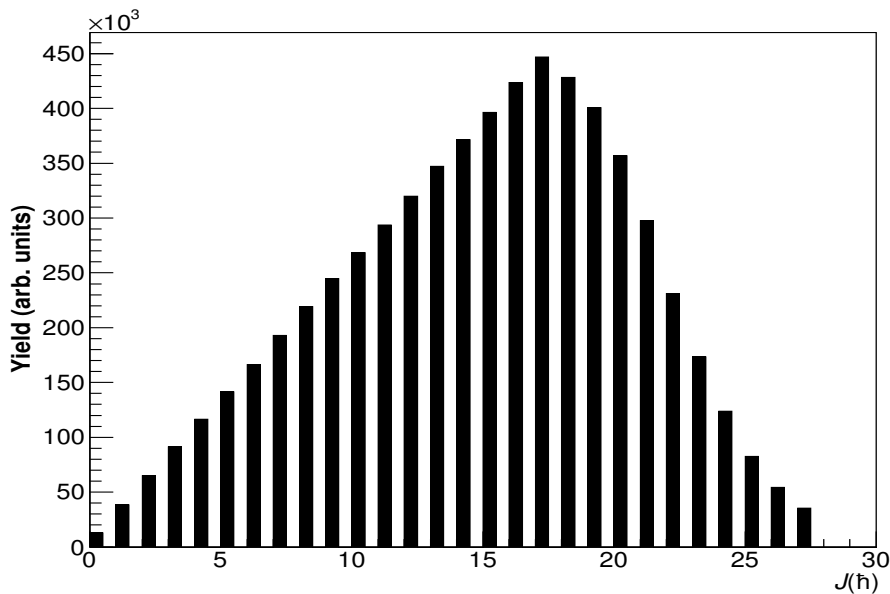


Figure 5.2: The distribution of the angular momentum of the CN, issued in the reaction at 130 MeV beam energy, used as an input for the HF $\ell$  simulation.

Table 5.1, is also used for the input of the angular momentum distribution in the HF $\ell$  Monte-Carlo simulation. The distribution used in the HF $\ell$  code is illustrated in Figure 5.2 for the  $^{16}\text{O}+^{12}\text{C}$  reaction performed at 130 MeV incident energy. A maximum value  $J_{max}=17 \hbar$  and a diffuseness parameter  $\Delta J = 2$  has been employed for this work similarly to a previous analysis [3].

## 5.1 Quasi-Complete Charge Detection Condition

As indicated in the introduction of this chapter, we will investigate some global distributions of observables for the events selected by the QC charge and momentum condition. A first comparison between experimental data and the HF $\ell$  model will also be made. In the last part of this section, these distributions will be compared with the results for the complete charge detection condition.

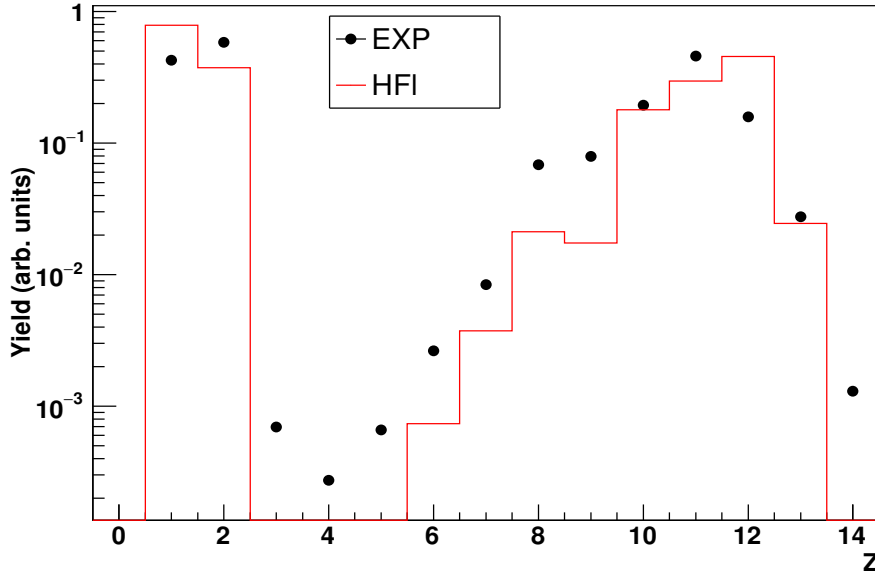


Figure 5.3: Charge distribution for the Quasi-Complete condition ( $10 < Z_{tot} < 15$ ) of the reaction at 90.5 MeV: the distributions are normalized to the total number of events. The black symbols represent the measured points while the red line gives the result of the HF $\ell$  calculation.

### 5.1.1 Charge Distribution and Multiplicities

The experimental charge distribution compared with the results of the HF $\ell$  evaporation code is shown in Figure 5.3 for the 90.5 MeV reaction. In the following figures, data are always shown with the statistical error bar, when visible. The charge distribution is overall well-reproduced by the HF $\ell$  model and the shape of the distribution is typical of fusion-evaporation reactions. In fact, one can clearly distinguish the light charged particle zone in the  $Z$  distribution, corresponding to Hydrogen and Helium isotopes, from the evaporation residue zone ( $Z > 4$ ). Nevertheless, a few differences can be noticed between the two charge distributions. First of all at this energy, in the region of  $Z=3, 4$  and  $Z=5$ , fragments are absent in the HF $\ell$  prediction while they are present in the experimental data. This could be explained as the presence in the data of a decay mechanism not included in the model calculation, *i.e.* the break-up channel. For  $Z=6, 7, 8$  and  $Z=9$  residues, the model underestimates the actual yield observed in the experimental data. This may be due to contamination from peripheral reactions caused by the inclusive condition imposed with this cut. In this way, an event with  $10 < Z_{tot} < 15$  could be shown in the distribution even though it is not a fusion-evaporation one. In Figure 5.4 the charge distribution is shown for the 110 MeV and 130 MeV incident energies. A

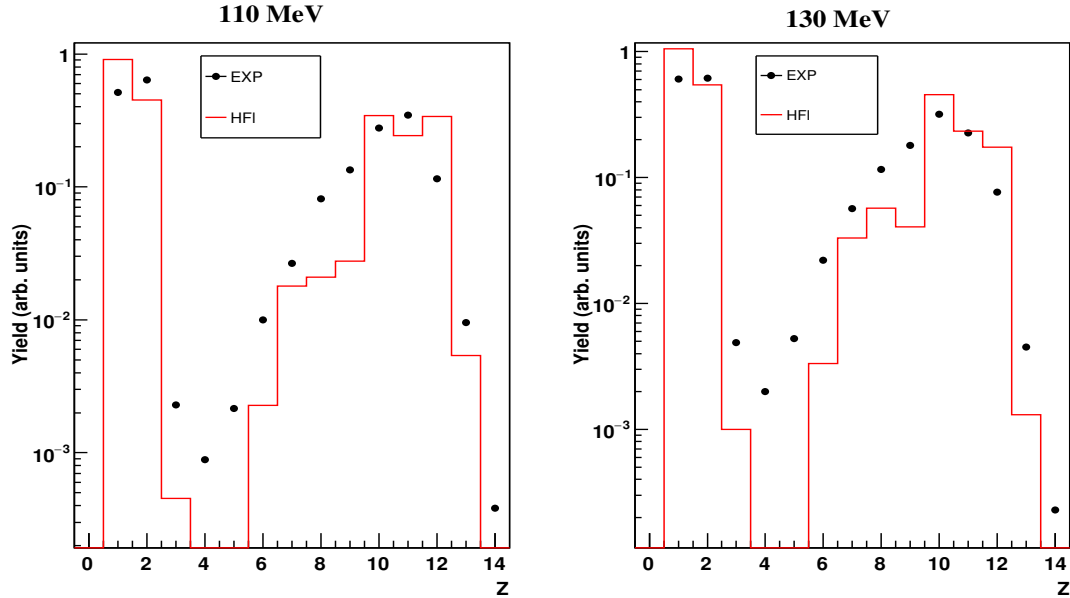


Figure 5.4: Charge distribution for the Quasi-Complete condition ( $10 < Z_{tot} < 15$ ) of the reaction at 110 MeV (left) and 130 MeV (right): the distributions are normalized to the total number of events. The black symbols represent the measured points while the red line gives the result of the HF $\ell$  calculation.

similar behaviour to the lowest energy appears.

Concerning the proton and  $\alpha$ -particle multiplicity, in Figure 5.5 the distributions are displayed. Every distribution seems to be quite well reproduced by the HF $\ell$  model for the three energies. Even so, for the proton distributions the experimental yield seems to be slightly overestimated by the model calculation at all incident energies. On the other hand the  $\alpha$ -particle multiplicity is better reproduced. A difference can be noticed for the five  $\alpha$ -particle multiplicity at all energies, where the fusion-evaporation model predicts a negligible yield.

### 5.1.2 Angular and Energy Distributions

We will now focus on the angular and energy distributions for protons and alpha particles detected in coincidence with an evaporation residue. In Figure 5.6 the global proton and alpha angular distributions in coincidence with any residue are presented for the 90.5 MeV reaction. The angles covered by the RCo apparatus are  $\theta < 20$ , whereas  $\theta > 20$  represents the angular coverage of the GARFIELD apparatus. Both distribution are given in the laboratory system. As one can see from Figure 5.6, a good agreement between the experimental data and the HF $\ell$  model predictions can be observed for both

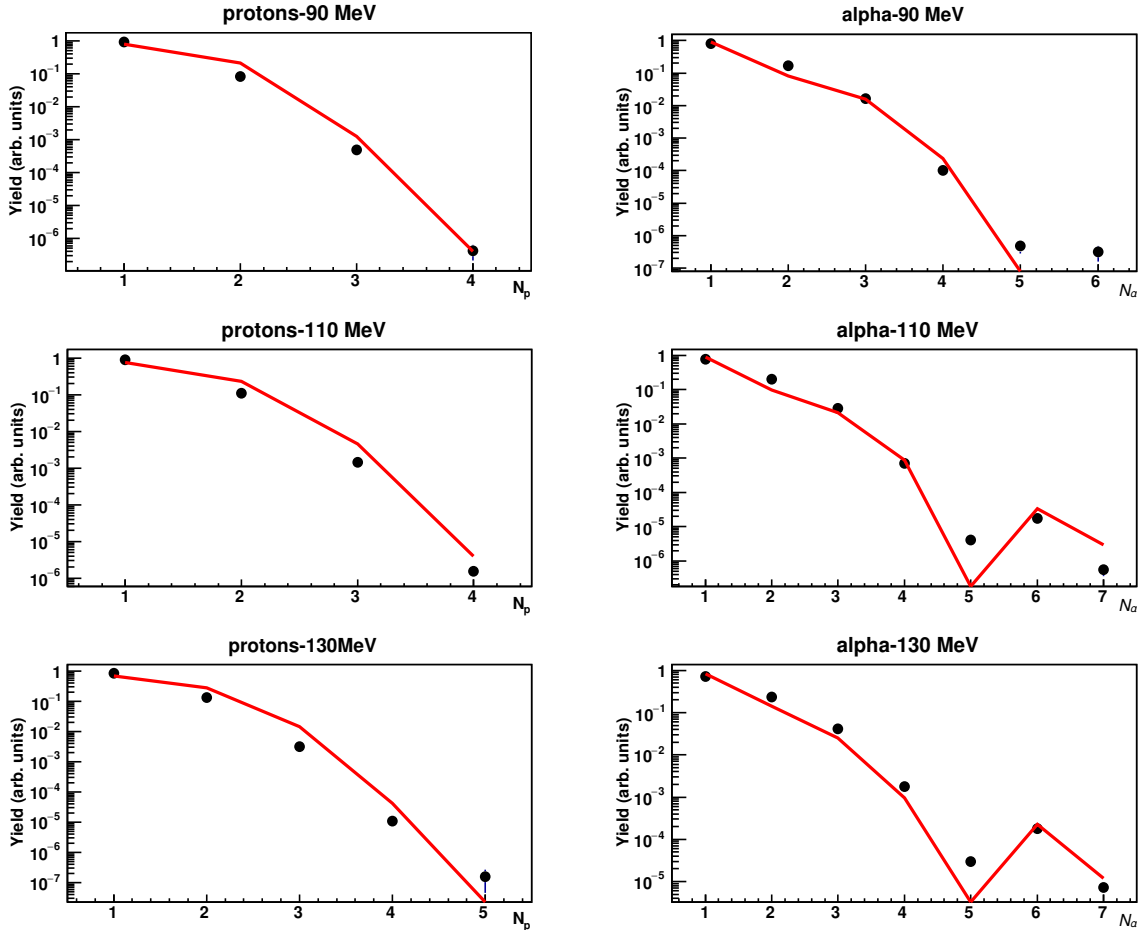


Figure 5.5: Proton (left) and alpha (right) multiplicity distribution for the Quasi-Complete condition ( $10 < Z_{tot} < 15$ ) of the reaction at 90.5 (top), 110 (middle) and 130 MeV (bottom): the distributions are normalized to the total number of events. The black symbols represent the measured points while the red line gives the result of the HFℓ calculation.

protons and  $\alpha$  particles, respectively.

As far as it regards the energies of particles, in Figure 5.7 the inclusive (GARFIELD and RCo) energy distribution for protons and alpha particles, detected with the QC condition (black dots for the experimental points and red lines for the HFℓ model) are presented, for the three reaction energies. For protons, a very good agreement between data and model is noticeable. On the contrary, the alpha particles present some differences. Indeed, one can see that high energy  $\alpha$  are underestimated by the HFℓ model for all energy cases.

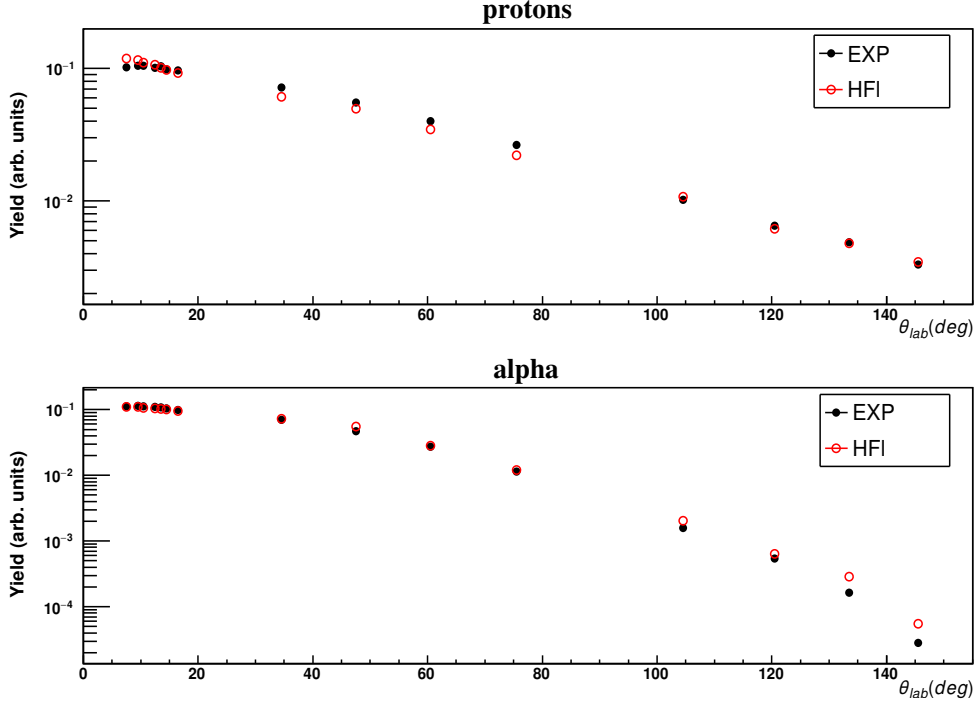


Figure 5.6: Proton (upper panel) and alpha (lower panel) angular distribution in the laboratory frame of reference for the Quasi-Complete condition ( $10 < Z_{tot} < 15$ ) of the reaction at 90.5 MeV: the distributions are normalized to unitary area. The solid black dots represent the measured points while the red empty dots are the result of the HF $\ell$  calculation.

### 5.1.3 Complete Charge Detection Condition

We have previously defined what we mean by complete charge detection, *i.e.* the sum of the detected charge by the whole apparatus (GARFIELD + RCo) has to be equal to the sum of the charges in the entrance channel ( $Z_{tot} = 14$ ). Moreover, a more stringent selection on the total detected momentum is also applied ( $0.8 < p_z/p_{beam} < 1.1$ ). This cut applied to the experimental sample obviously reduces the overall statistics of the analyzed data. Only 20% of the QC data satisfies this second requirement. However, due to the high geometrical efficiency of the apparatus, the remaining data have sufficient statistics for the following analysis.

In Figure 5.7, both alpha and proton energy distributions for the quasi-complete and complete detection of the charge are represented, for the 90.5, 110 and 130 MeV reaction. One can notice that for all the energies an overall good reproduction of the distribution shape by the HF $\ell$  model is achieved. Specifically, there is no significant difference in the energy distribution of the protons between the two cuts of the analysis,

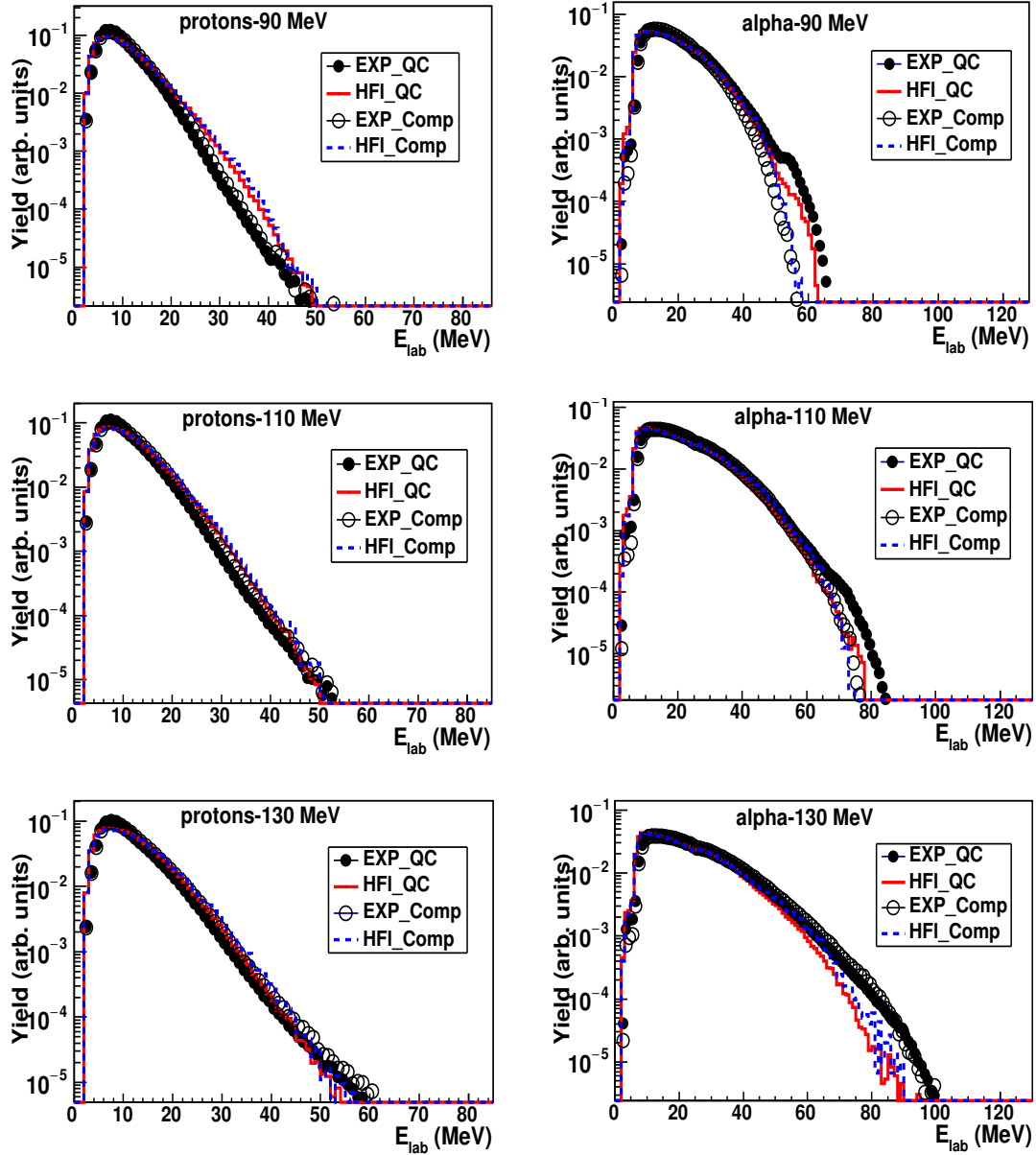


Figure 5.7: Proton (left panel) and alpha (right panel) energy distribution of the reaction at 90.5, 110 and 130 MeV: the distributions are normalized to unitary area. The black solid symbols represent the measured points for the Quasi-Complete condition ( $10 < Z_{tot} < 15$ ) while the red line gives the result of the HF $\ell$  calculation. Similarly, the black empty symbols represent the measured points for the Complete condition ( $Z_{tot} = 14$ ) while the blu dashed line shows the result of the HF $\ell$  calculation.

namely before and after the complete charge detection condition. On the other hand, we can notice that the requirement of  $Z_{tot} = 14$ , for the alpha particles, has slightly reduced the maximum energy and the previous energy differences between data and model. One can attribute this change to the charge conservation requirement which has reduced the contamination from peripheral events. In fact, if one observes the same distribution

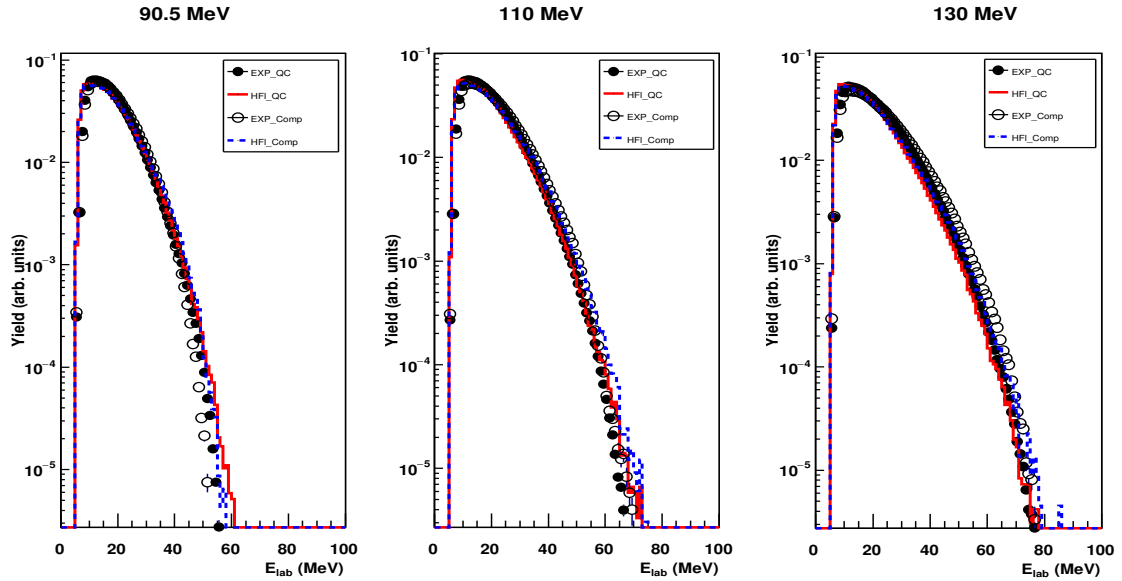


Figure 5.8: Alpha energy distribution, detected only by GARFIELD, in the reaction at 90.5 MeV (left panel), 110 MeV (middle panel) and 130 MeV (right panel): the distributions are normalized to unitary area. The black solid symbols represent the measured points for the Quasi-Complete condition ( $10 < Z_{tot} < 15$ ) while the red line gives the result of the HFℓ calculation. Similarly, the black empty symbols represent the measured points for the Complete condition ( $Z_{tot} = 14$ ) while the blue dashed line shows the result of the HFℓ calculation.

only for alpha particles detected by the GARFIELD apparatus no major discrepancies appear. This behaviour is well illustrated in Figure 5.8 where the energy distribution is plotted for each energy of the reaction. Despite of small changes, it is important to observe that the HFℓ model reproduces the experimental data in the two selections (QC and complete). In the case of complete charge detection, a better agreement between the experimental data and the results of the model predictions seems to be obtained for the energy distributions of the alpha particles.

For the total charge distribution, a comparison between the quasi-complete and complete condition is illustrated in Figure 5.9. As one can notice, the distributions still represent a typical fusion-evaporation charge distribution. The charge conservation requirement has changed the yield for some  $Z$ , reducing in particular  $Z = 7$  and  $Z = 9$ ,

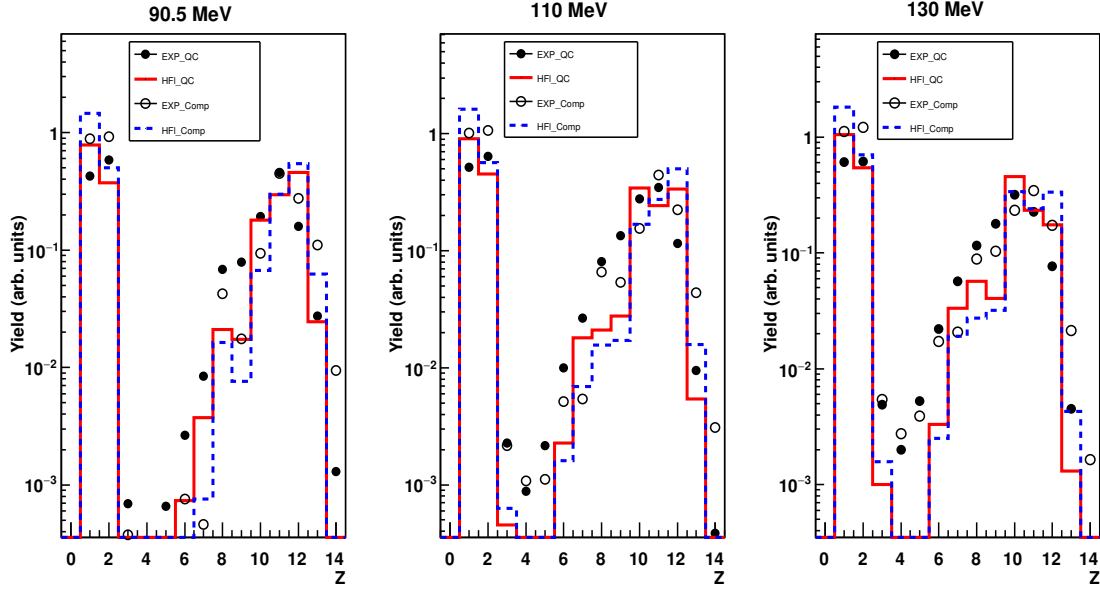


Figure 5.9: Charge distribution for the Quasi-Complete (QC) and Complete selection at 90.5 (left), 110 (middle) and 130 MeV (right): the distributions are normalized to the total number of events. The solid black symbols represent the measured points with the QC condition while the empty dots represent the Complete selection. The results of the HF $\ell$  calculation are given by the red line for the QC and blu dashed line for the complete selection, respectively.

but the whole distribution does not change significantly. The peak of the evaporation residue distribution is located at the same value. All distributions present a low yield of  $Z$  intermediate between LCP and ER with slightly different distributions. It is worthwhile to notice that the shape of the total charge distribution obtained after the complete condition is better reproduced by the HF $\ell$  predictions.

The results obtained in this section, allows us to continue the analysis with the minimum bias event selection imposed by the  $Z_{tot} = 14$  condition as the global variables shown previously do not exhibit major changes after this cut in the analysis. Furthermore, it is evident that the contamination of non-central events is much lower in the complete selection. Henceforth, the following results are obtained with this selection.

## 5.2 Evaporation Residue Selection

The comparison made so far included only global inclusive observables which only indicated the overall dominance of fusion-evaporation events. To take this a step further,

one can study the same observables, as for example energy and angular distributions, with more and more exclusive conditions starting from the ER selection. In the following part of this chapter we will try to investigate in more detail the different decay channels of the CN based on the selection of the evaporation residue. Furthermore, one can study the branching ratio associated with particular channels and identify the most interesting ones. This allows a more precise comparison between the experimental data and the HF $\ell$  statistical decay code which can underline possible significant differences due to either structure or clustering effects. For the following studies only residues with  $Z_{big} > 5$  will be employed in the analysis since the other show too low statistics.

### 5.2.1 Energy Distributions

For the three beam energies (90.5, 110 and 130 MeV), the energy and angular distributions of the LCP detected in coincidence with the evaporation residue and the energy distribution of this latter fragment will be presented and described.

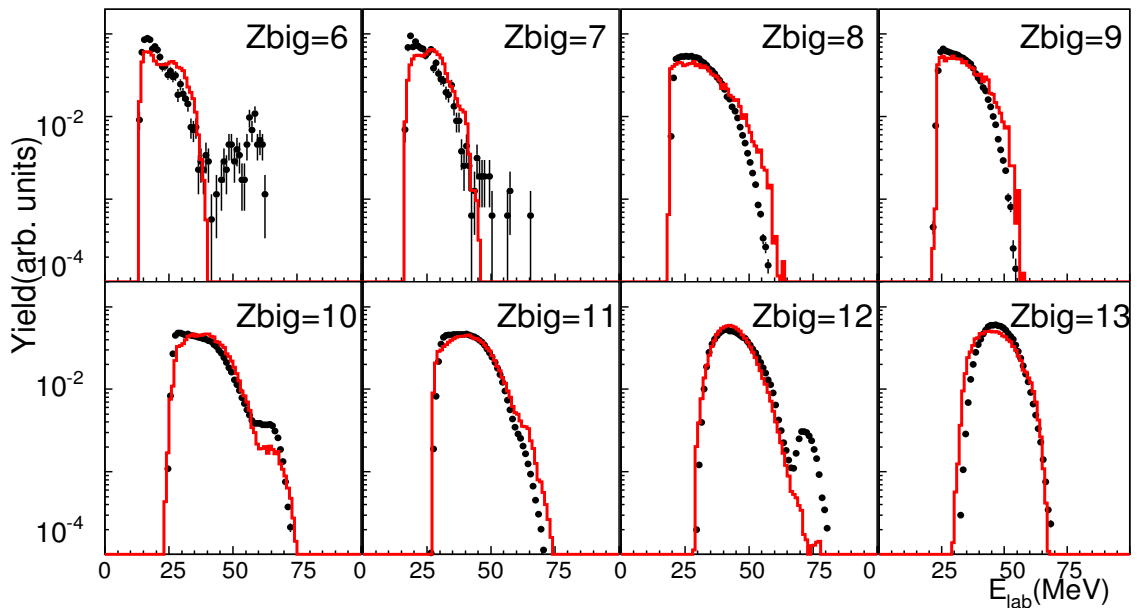


Figure 5.10: Energy distribution for the ER, indicated with  $Z_{big}$  in each panel, for the 90.5 energy case. The data (black dots) is compared to the the HF $\ell$  predictions (red line). All distributions are normalized to unitary area.

The evaporation residue energy distributions are shown in Figure 5.10, 5.11 and 5.12 for the three energies of the reaction. The larger discrepancies are present in the distributions of  $Z_{big}=6$ ,  $Z_{big}=10$  and  $Z_{big}=12$ . In particular, as far as  $Z_{big}=6$  is concerned, one could invoke possible contaminations from reactions different from the fusion-evaporation ones, being  $Z_{big}=6$  very close to the charge of the colliding partners. Indeed, a second

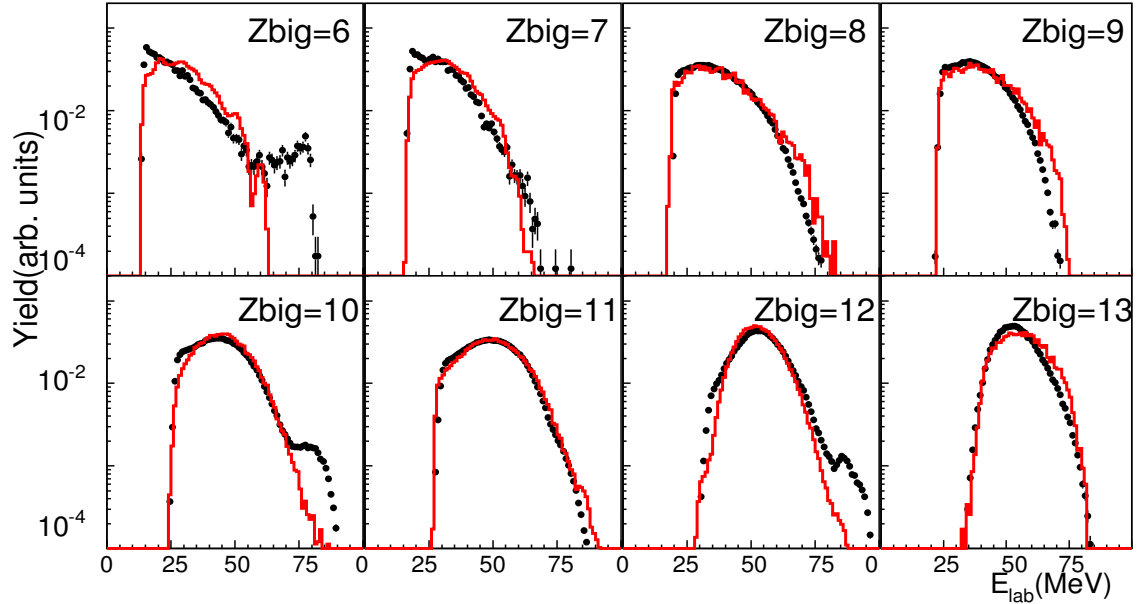


Figure 5.11: Energy distribution for the ER, indicated with  $Z_{big}$  in each panel, for the 110 energy case. The data (black dots) is compared to the the HF $\ell$  predictions (red line). All distributions are normalized to unitary area.

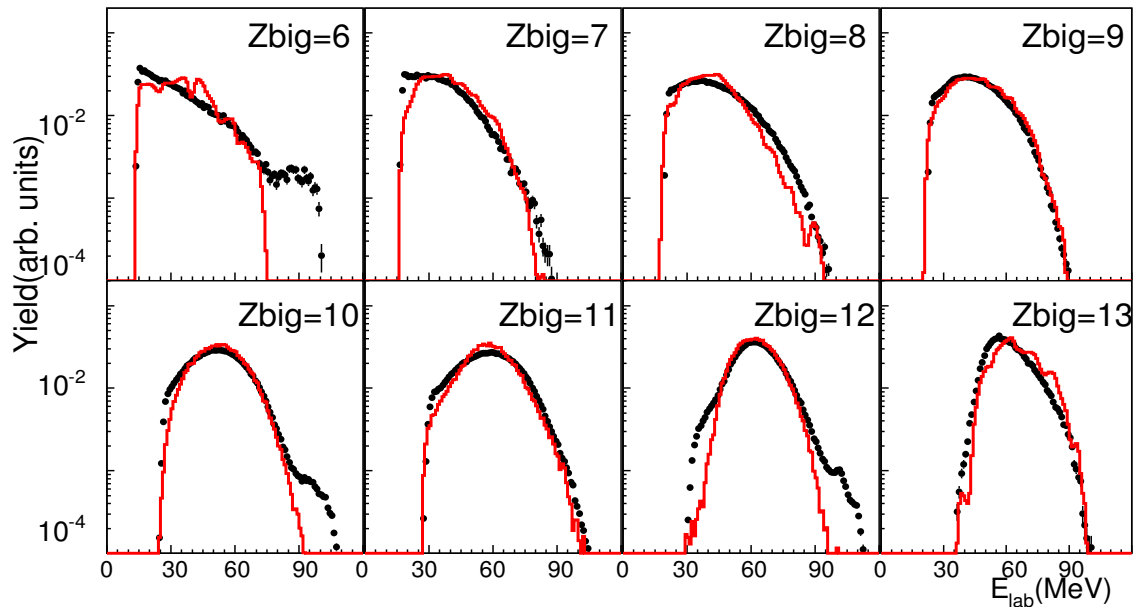


Figure 5.12: Energy distribution for the ER, indicated with  $Z_{big}$  in each panel, for the 130 energy case. The data (black dots) are compared to the the HF $\ell$  predictions (red line). All distributions are normalized to unitary area.

energy peak is particularly evident for the Carbon ER in all energy cases. The discrepancies can be attributed to contamination from direct reaction such as alpha transfer reactions or breakup reactions, which are not included in the fusion-evaporation HF $\ell$  model. In fact, the Carbon residue is for 50% of the cases detected in coincidence with another Z=6 fragment. Moreover, the evaporation of fragments heavier than Berilium isotopes is not considered in the HF $\ell$  event simulations and therefore the model prediction can not reproduce the events present in the experimental data.

To examine more in depth this hypothesis, one can apply a cut to the energy distribution based only on the coincidence of the ER with LCP ( $\alpha$ ,  $^3\text{He}$ , p, d and t). In this case, the agreement between the spectra predicted by the model and obtained from the data is improved for  $Z_{big}=6$  (see Figure 5.13) confirming the presence of direct reaction contamination in the previously seen Figure 5.10, 5.11 and 5.12. For the others ER, the high energy "bump" noticed for  $Z_{big}=10$  and 12 not reproduced by HF $\ell$ , can not be explained on the same basis of  $Z_{big}=6$ . The contaminations from direct or heavy fragments emission is less probable due to the heavier mass of the evaporation residue. Therefore, these cases require further investigations and will be detailed in the next sections with regards to the branching ratio and Q-values of these decay channels.

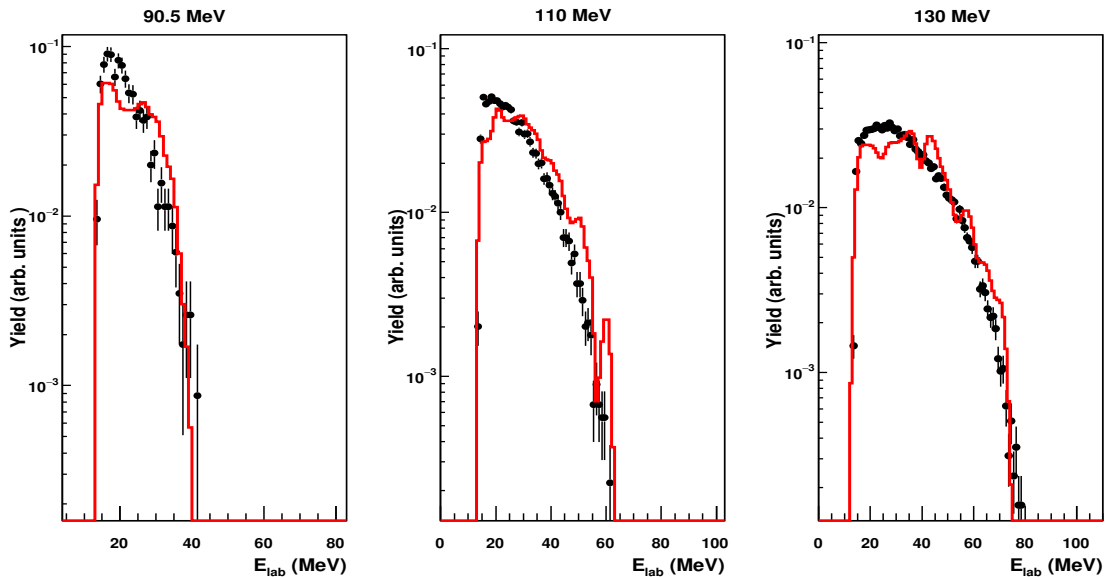


Figure 5.13: Energy distribution for the ER with  $Z_{big}=6$ , for the 90.5 (left), 110 MeV (middle) and 130 (right) energy cases, after the LCP multiplicity cut. The data (black dots) are compared to the the HF $\ell$  predictions (red line). All distributions are normalized to unitary area.

In Figure 5.14, 5.15 and 5.16 the energy of protons and alpha particles detected in

coincidence with a specific residue ( $Z_{big}$ ) are shown for the three energy cases. All the energy distributions are obtained by integrating the particles detected with the coupling of the two apparatus, *i.e.* GARFIELD and RCo. To point out discrepancies of the shape of the spectra between the experimental data and the model calculation, we choose to normalize them to unitary area. From now on, the first panel for protons and the panel for alpha particles have been intentionally left empty due to either very low statistics or non physical cases. When visible, the data points are shown with the corresponding statistical error.

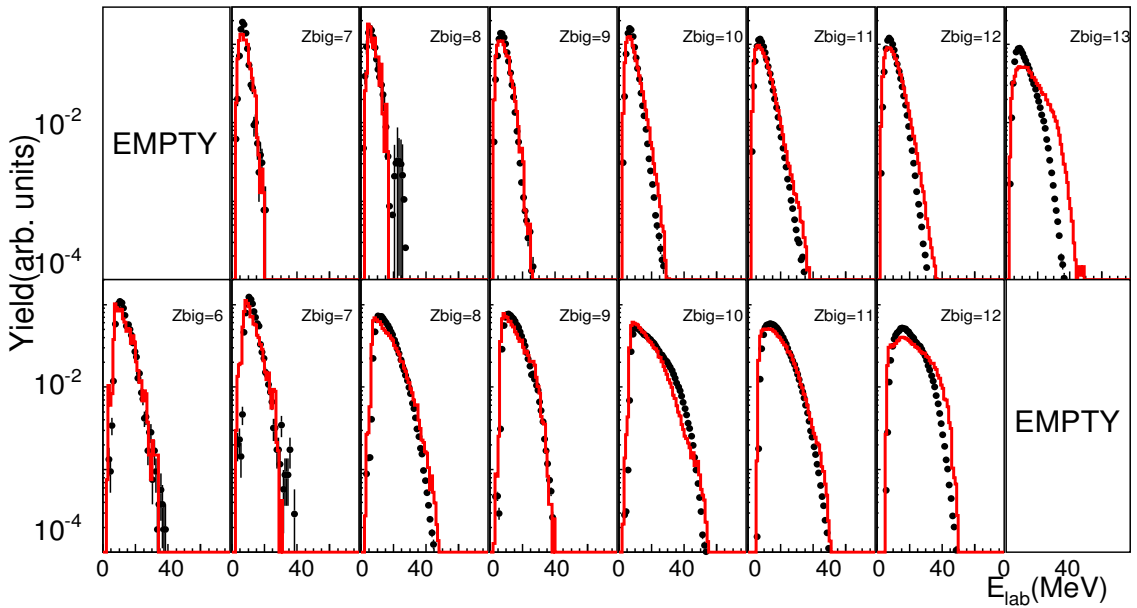


Figure 5.14: Proton (upper panels) and  $\alpha$  (lower panels) laboratory energy spectra detected in coincidence with a ER of charge  $Z_{big}$ , indicated in each pad, for 90.5 MeV. The data (black dots) are compared to the the HF $\ell$  predictions (red line). All distributions are normalized to unitary area. The first panel for protons and the last panel for alpha are intentionally left empty due to either very low statistics or non physical cases.

The proton distributions show an overall good agreement with the HF $\ell$  predictions for all tree energies and for almost all the evaporation residue detected, except for  $Z_{big}=13$ . In this case, a significant discrepancy between the HF $\ell$  and the experimental points is clearly visible for the three energies of the reaction. Indeed, the model overestimates the number of high energy protons and also poorly reproduces the shape of the distribution. Therefore, the channels associated to this particular  $Z_{big}$  will require further studies as we will discuss in the next sections. As far as the alpha particles are concerned, the comparison between data and model calculation shows a satisfying agreement for all the energies and ER considered, except for the Neon ( $Z_{big}=10$ ) case and in smaller part also for the Magnesium ( $Z_{big}=12$ ) case. The discrepancy is particularly evident for the former

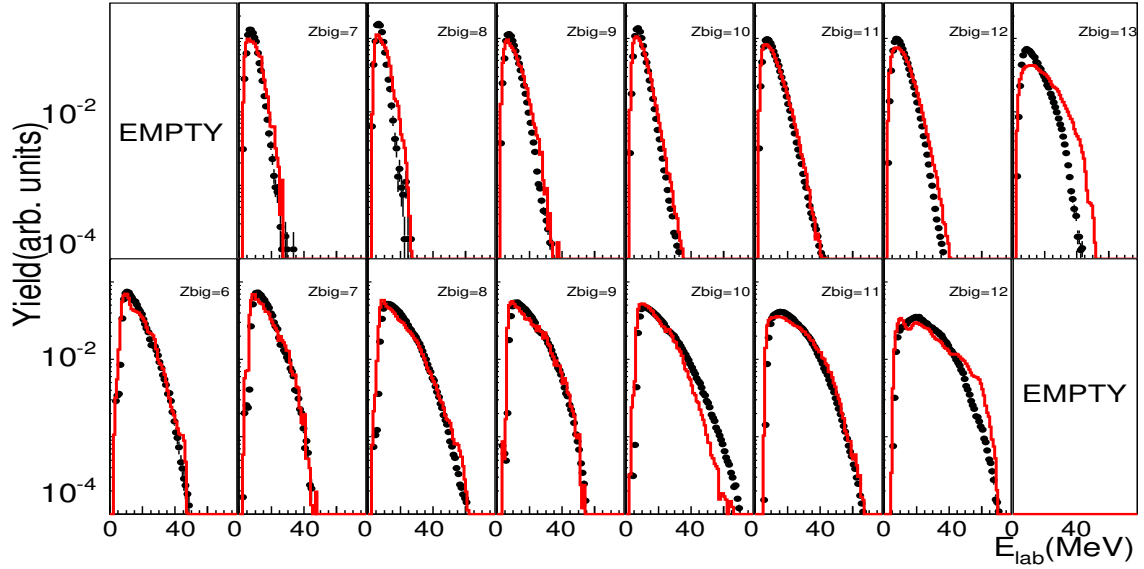


Figure 5.15: Proton (upper panels) and  $\alpha$  (lower panels) laboratory energy spectra detected in coincidence with a ER of charge  $Z_{big}$ , indicated in each pad, for 110 MeV. The data (black dots) is compared to the the HF $^l$  predictions (red line). All distributions are normalized to unitary area.

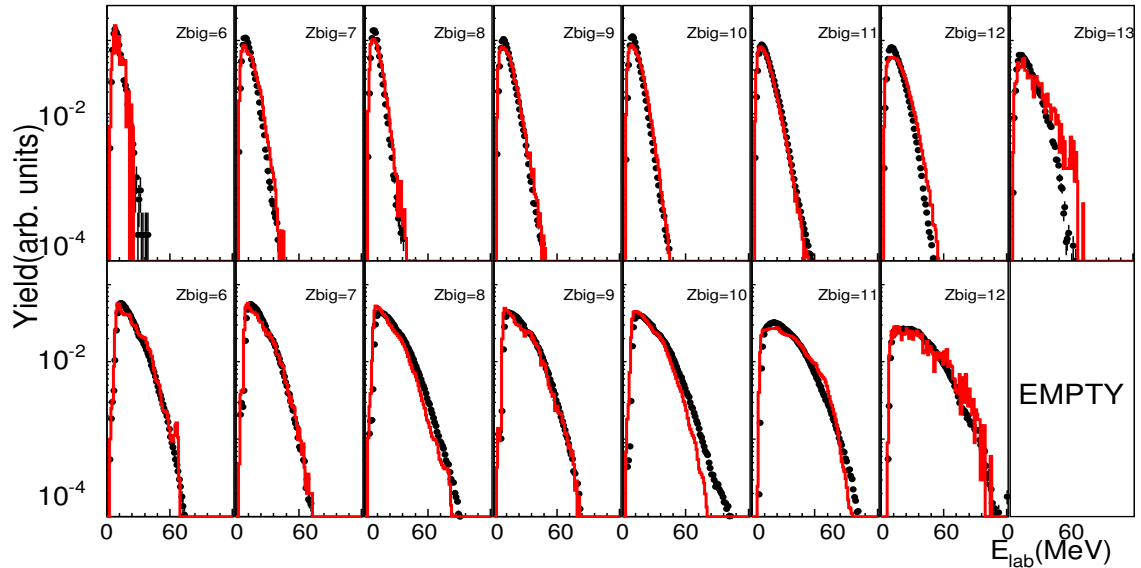


Figure 5.16: Proton (upper panels) and  $\alpha$  (lower panels) laboratory energy spectra detected in coincidence with a ER of charge  $Z_{big}$ , indicated in each pad, for 130 MeV. The data (black dots) are compared to the the HF $^l$  predictions (red line). All distributions are normalized to unitary area.

at greater energies as 110 and 130 MeV where the HF $\ell$  model underestimates the actual experimental yield and shape of the  $\alpha$  particles distribution. It is important to recall that these distributions are inclusive of all the possible decay channels associated to the ER detected and therefore at this point one cannot draw any conclusions on the type of effects that lead to the observed deviations. In fact, these can be caused either by branching ratio differences or by different population of the more dissipative reaction (decay modes involving neutrons) and less dissipative reaction (decay modes without neutrons), for the same decay channel, between data and the HF $\ell$  model. This will be the main topic of the section 5.3.

## 5.2.2 Angular Distributions

Moving forward with the ER inclusive observables, we want to check if the same deviations are present also for other variables. Therefore, we take a closer look to the angular distributions and compare them to the HF $\ell$  model predictions as well. The

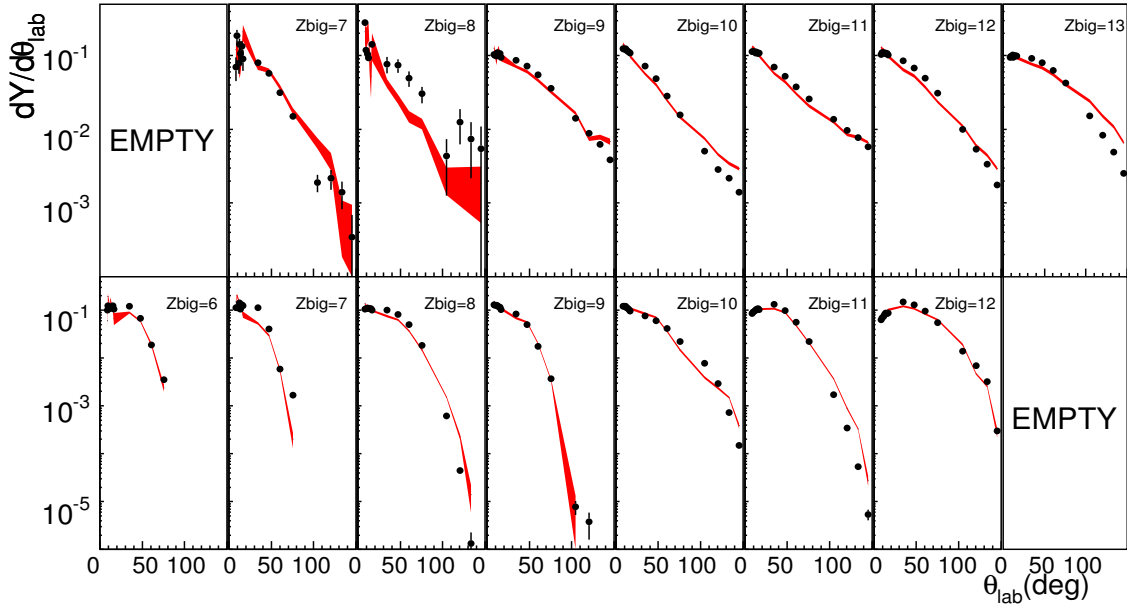


Figure 5.17: Proton (upper panel) and  $\alpha$  (lower panel) angular distributions in the laboratory frame, detected in coincidence with the indicated  $Z_{big}$  evaporation residue for 90.5 MeV incident energy. The experimental data is represented by the solid black dots while the model calculation is displayed by the red band. The experimental and model spectra are normalized to unitary area.

statistical errors for the model predictions are here represented as a red band given by the limits of these errors. In Figure 5.17, 5.18 and 5.19 the angular distributions of protons and alpha particles detected in coincidence with the ER specified by the  $Z_{big}$

charge are represented. The empty pads represent either low statistics cases or non physical cases. For protons, one can notice that the  $HF\ell$  model predictions (red band) reproduces the shape of the angular distribution of the experimental data (black dots) in most of the ER cases. An evident deviation is observed for the Aluminium residue ( $Z_{big}=13$ ) for large emission angles in all three energies of the reaction. This feature confirms the discrepancy noticed previously in the energy distribution for the same ER.

For alpha particles similar considerations can be made. One can notice that generally the model follows the experimental data points except for two values of  $Z_{big}$ . The most obvious case of discrepancy is observed for the Neon residue, where the  $HF\ell$  systematically fails to reproduce the experimental yield. Therefore, the previously observed differences for the Neon residue are confirmed in these distributions as well. Another less evident case is represented by the  $Z_{big}=8$  angular distribution. In particular, for the 130 MeV beam energy, one can notice a not negligible deviation for the alpha particles detected at increasing laboratory angles. This behaviour may suggest a departure from the fusion-evaporation model as the excitation energy increases for this particular residue. The observed discrepancies will be further investigated by trying to disentangle the various contributions of the measured decay modes. The origin of the deviations from the statistical behaviour will be studied more in detail using the branching ratio to  $\alpha$  decay and the Q-values in the different channels involving  $\alpha$  and/or proton emission .

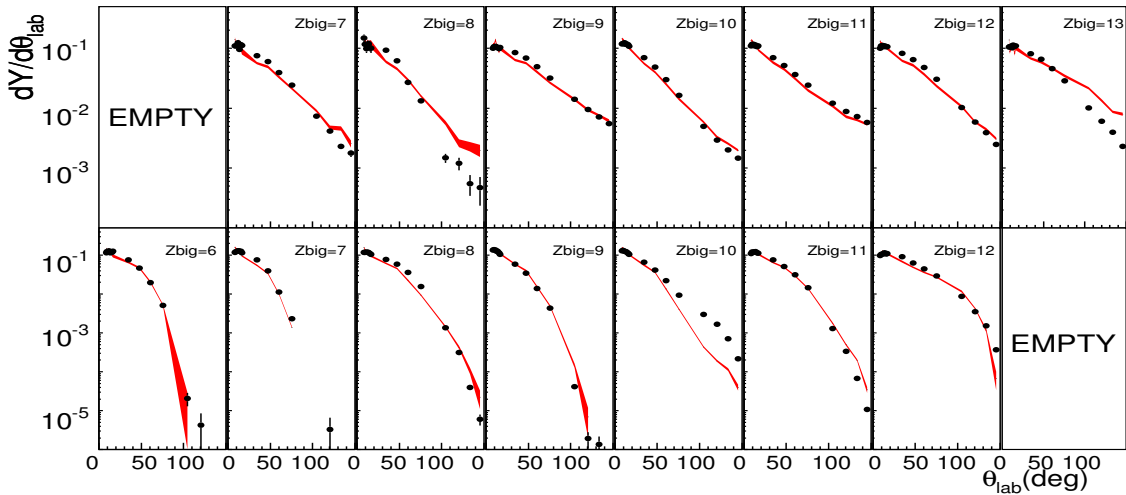


Figure 5.18: Proton (upper panel) and  $\alpha$  (lower panel) angular distributions in the laboratory frame, detected in coincidence with the indicated  $Z_{big}$  evaporation residue for 110 MeV incident energy. The experimental data is represented by the solid black dots while the model calculation is displayed by the red band. The experimental and model spectra are normalized to unitary area.

### 5.3 Excitation Energy Dependence and Clustering Effects

The analysis performed so far has evidenced some deviations from a fusion-evaporation mechanism in most of the observables we investigated. In particular for certain evaporation residues ( $Z_{big} = 10, 12$  and  $13$ ), both their energy distributions and that of the protons and alpha-particles detected in coincidence with the ERs, showed a disagreement between the data and the HF $\ell$  model. This disagreement has been confirmed also by the angular distributions of the LCP.

In the previous analysis one has considered all the decay channels with a given residue. Therefore, the observed shape differences, between experimental data and HF $\ell$  predictions, can be in principle due to differences in the Branching Ratio (BR) of the decay channels between observed and HF $\ell$  calculated values. In fact, one expects that every distinct channel can have a different contribution to the total integrated shape associated to a particular evaporation residue. With a further selection, the model and data agreement can be tested by focusing only on particular channels.

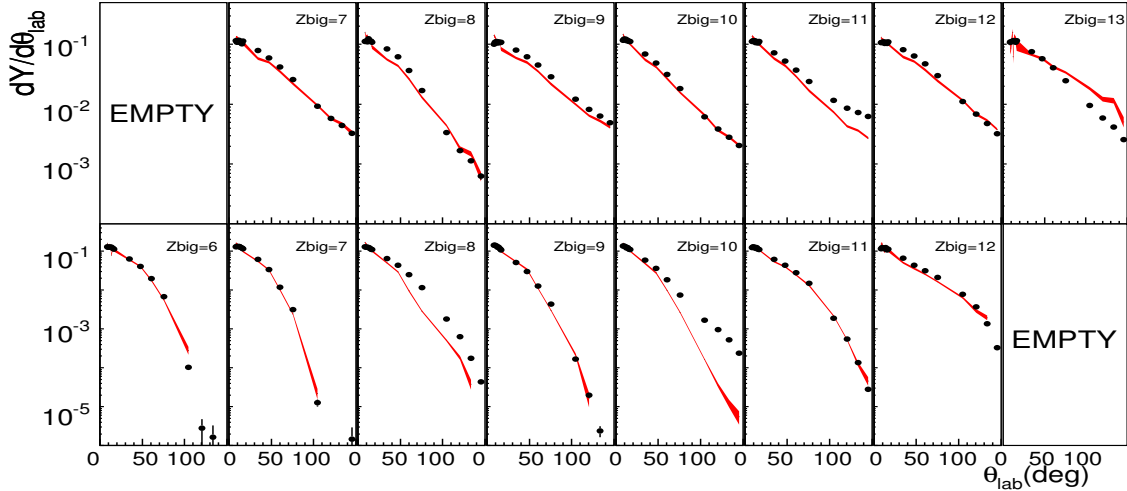


Figure 5.19: Proton (upper panel) and  $\alpha$  (lower panel) angular distributions in the laboratory frame, detected in coincidence with the indicated  $Z_{big}$  evaporation residue for 130 MeV incident energy. The experimental data is represented by the solid black dots while the model calculation is displayed by the red band. The experimental and model spectra are normalized to unitary area.

### 5.3.1 Branching Ratio

Following the work of [3], what is done in this subsection is to identify ER by ER the most populated decay channel and evaluate its branching ratio both for the experimental and the HF $\ell$  data. The most probable decay channels are first selected for the experimental data of the 90.5 MeV reaction and their behaviour with increasing excitation energy is studied. The results are shown in Table 5.2 where each incident energy is presented. Errors on the experimental values are estimated to be about 5%. These take into account both the statistical error and the possible identification contamination between  ${}^3\text{He}-\alpha$  or p-d-t, especially under the discrimination thresholds where the isotopes mass separation is not achievable. Since the excitation energies of the issued CN are

$Z_{res}$	Channel	90.5 MeV (%)		110 MeV (%)		130 MeV (%)	
		BR $_{exp}$	BR $_{HF\ell}$	BR $_{exp}$	BR $_{HF\ell}$	BR $_{exp}$	BR $_{HF\ell}$
6	${}^{12-xn}\text{C}+xn+4\alpha$	100	100	100	100	99	93
7	${}^{15-xn}\text{N}+xn+p+3\alpha$	99	99	98	99	95	98
8	${}^{16-xn}\text{O}+xn+3\alpha$	99	99	99	90	88	46
9	${}^{19-xn}\text{F}+xn+p+2\alpha$	99	99	93	95	87	90
10	${}^{20-xn}\text{Ne}+xn+2\alpha$	74	18	45	4	29	2
11	${}^{23-xn}\text{Na}+xn+p+\alpha$	95	95	92	88	87	58
12	${}^{24-xn}\text{Mg}+xn+\alpha$	52	10	35	4	28	2
13	${}^{27-xn}\text{Al}+xn+p$	90	95	87	94	84	88

Table 5.2: For the measured evaporation residue, the table shows the most probable channels and their experimental branching ratio alongside with the predicted HF $\ell$  value for each one of the three available energies.

large compared with the Q-values for the emission of neutrons, the decay channels in Table 5.2 are shown with the possible number "xn" of emitted neutrons. The first noticeable result of this Table 5.2 is that the most probable experimental channel is mainly the one with a given residue which has the maximum of  $\alpha$ -particles emitted, except for the Aluminium residue where an  $\alpha$ -particle cannot be emitted. As one can notice from Table 5.2 and considering the mentioned errors, the BR of the dominant decay channel is consistent with the HF $\ell$  model calculation for the odd-Z residues, with the exception of the  ${}^{23-xn}\text{Na}+xn+p+\alpha$  channel at 130 MeV. In this decay, the HF $\ell$  prediction fails to reproduce the actual population. On the contrary for even-Z residues, most of the BR of the dominant channels are not well reproduced by the Hauser-Feshbach model. In particular, the Carbon channel is consistent with the HF $\ell$  prediction for two of the three reaction energies while for Oxygen, Neon and Magnesium residues the  $\alpha$  decay channels are almost always underestimated with respect to the experimental data. Moreover, one can notice that this disagreement seems to change with increasing excitation energy, as

for example if we consider the  $^{16-xn}\text{O}+xn+3\alpha$  decay mode. In this case, the experimental BR is confirmed by the model calculation at 90.5 MeV but starts to significantly disagree for the other two higher energies.

The branching ratio can be used to explain the discrepancies for the energy distributions of the ER with  $Z_{big}=10$  and 12 in Figure 5.10, 5.11 and 5.12, by looking at the same distribution with the exclusive condition of ER measured only in a specific channel. In this way, the deviations can be attributed to different values of the branching ratio calculated with the HF $\ell$  model and experimental data, respectively. This hypothesis is supported for example if one compares Figure 5.20 with the Neon panel in Figure 5.11. Indeed, the energy distribution of the Neon ER measured in its most probable decay channel (see Table 5.2) is well reproduced by the HF $\ell$  predictions while the same could not be inferred before for the inclusive energy distribution. Therefore, we can safely conclude that the observed differences, for  $Z_{big}=10$  and  $Z_{big}=12$ , are due to the different population of the decay channels in the HF $\ell$  simulations and the actual experiment, as reported in Table 5.2.

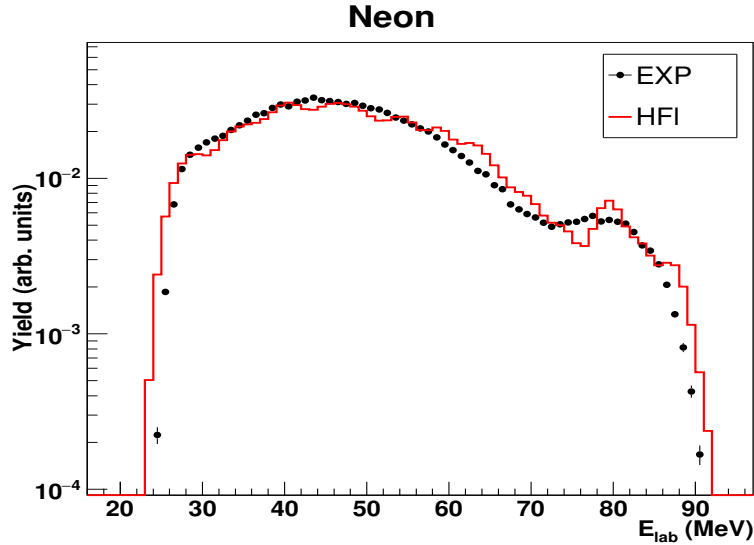


Figure 5.20: Energy distribution of the  $Z_{big}=10$  measured in the channel  $^{20-xn}\text{Ne} + xn + 2\alpha$  for the 110 MeV reaction. The black dots represent the experimental data whereas the red line shows the results of the HF $\ell$  calculation. The energy spectra are both normalized to unitary area.

Similarly, one can point out that the observed discrepancies in the  $\alpha$ -particle energy distribution in Figure 5.14, 5.15 and 5.16 come from the same differences in the branching ratio between data and model. As a matter of fact, if we consider the two reaction energies for which a previous discrepancy was noticed (110 and 130 MeV), the energy distributions of the  $\alpha$ -particles are well reproduced by the HF $\ell$  model (see Figure 5.21)

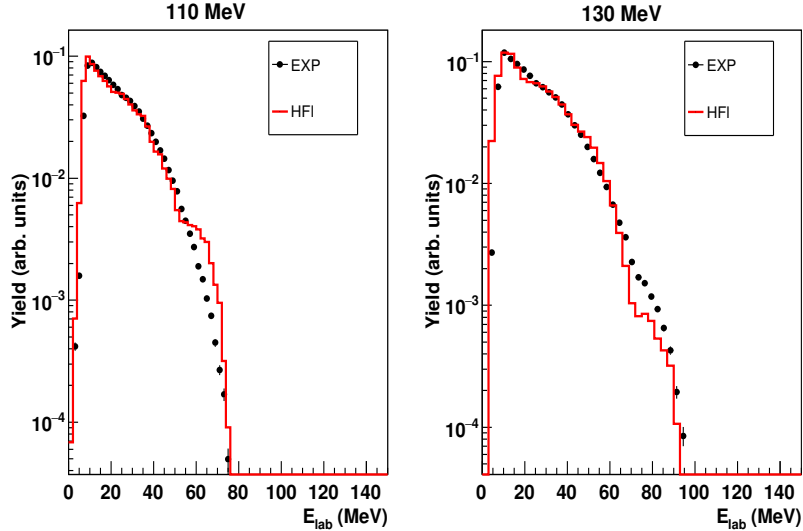


Figure 5.21: Energy distribution of the alpha particles measured only in the  $^{20-xn}\text{Ne} + xn + 2\alpha$  for the 110 and 130 MeV reactions. The black dots represent the experimental data whereas the red line shows the results of the HF $\ell$  calculation. The energy spectra are both normalized to unitary area.

for the specific channels involving two emitted  $\alpha$ -particles. Therefore, we proved that the differences between data and model, in the inclusive energy distributions of the  $\alpha$ -particles for the Neon case, are due to the different evaluation of the BR by the former and latter, respectively. The same holds true also for the  $Z_{big}=12$  ER with the emission of an  $\alpha$ -particle.

To sum up, the previous example showed that the kinematics of the decay are well described by a fusion-evaporation model. However, as each specific channel has its own distributions with its own different shape, the disagreement in the BRs between model and data affects the global shape of the  $\alpha$  distribution, where every single channel is summed up. Further conclusions on the observed BR and differences with the HF $\ell$  model will be drawn in the last part of this chapter.

### 5.3.2 Q-value Distributions

For the study of nuclear reaction another observable which can provide more information is the Q-value. This parameter is normally defined as the mass difference between the initial nucleus and the sum of the decay products. Considering energy conservation of a reaction, the Q-value can also be written as the difference between the initial and final kinetic energy. Therefore, in the case of a fusion-evaporation reaction where a CN is formed, we can define a similar quantity which gives an estimate of the dissipated

energy event by event:

$$Q_{val} = E_{kin} - E_{beam} = \sum_{i=1}^N E_i - E_{beam} \quad (5.1)$$

where  $E_i$  represents the energy of the particles in the laboratory frame and  $E_{beam}$  is the initial energy of the projectile nucleus. The summation extends to the  $N$  particles and fragments that are detected in coincidence, and exhausts the total charge  $Z_{tot} = 14$ . The quantity  $Q_{val}$  in eq. 5.1 corresponds to the real Q-value of the reaction, resulting from the aforementioned mass balance, when the whole mass and energy is detected in the outgoing channel. Therefore, it depends on the experimental apparatus which in our case (GARFIELD and RCo) is not optimized to measure neutrons and gamma ray emitted in the decays. As a result, a region of continuous contribution from the neutron missing energy will be superimposed on the discrete Q-value spectrum. This contribution defines the more dissipative events corresponding to low Q-values, where the emission of one or more neutrons takes place. In Figure 5.22 and 5.23 the Q-value distributions are presented for the most probable decay channels illustrated in table 5.2 for all the reaction energies. The experimental data are always shown together with the HF $\ell$  model predictions.

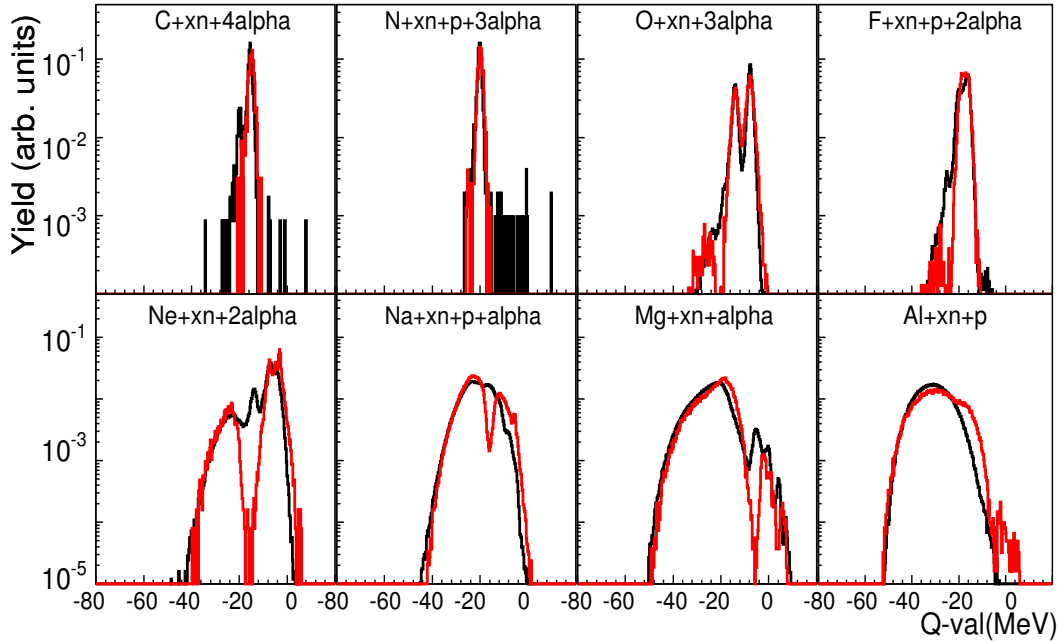


Figure 5.22: Q-value distributions for the channels presented in Table 1.4 for 90.5 MeV. The black line corresponds to distributions obtained for the experimental data while the red one gives the HF $\ell$  predictions. All the distributions are normalized to unitary area.

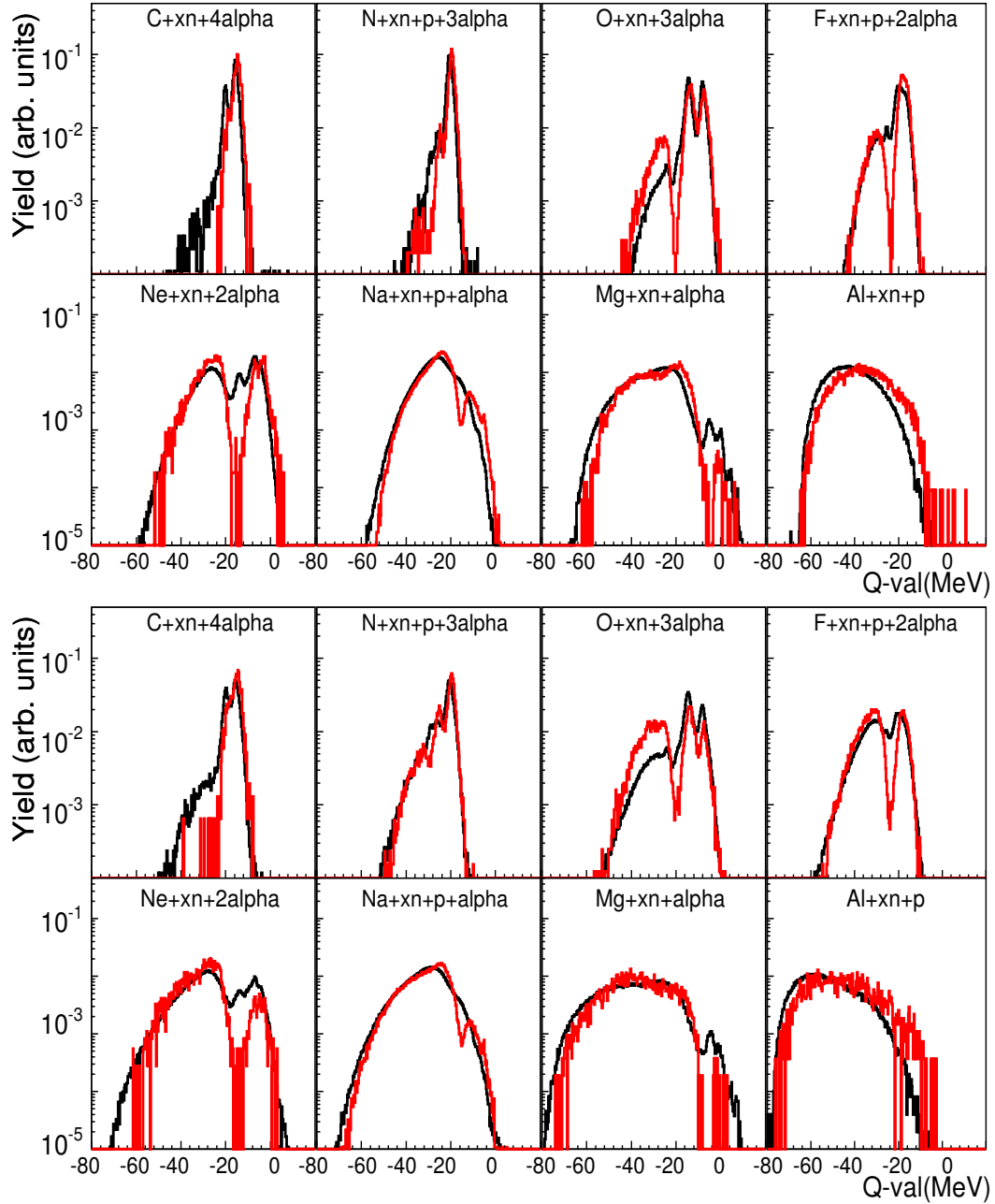


Figure 5.23: Q-value distributions for the channels presented in Table 1.4 for 110 (top panels) and 130 MeV (low panels). The black line corresponds to distributions obtained for the experimental data while the red one gives the  $\text{HF}\ell$  predictions. All the distributions are normalized to unitary area.

We can see that the theoretical and experimental spectra show a common peak structure (higher  $Q_{val}$ ) and the before mentioned broader region (lower  $Q_{val}$ ) associated to the opening of channels involving neutrons. The different peaks at higher  $Q_{val}$  correspond to the various evaporations chains, starting from the excited  $^{28}Si^*$  compound nucleus, and leaving a residue of charge  $Z_{big}$  in one of its isotopic ground or low lying excited states. Even though the  $Q_{val}$  resolution is limited, the energy levels of the residue can be clearly recognized in the experimental sample. The model and data present an overall good agreement with only small differences in the yield caused by a different population of the more dissipative and less dissipative channels. In Figure 5.24, the Q-value distribution for the  $^{16-xn}O+xn+3\alpha$  decay channel is illustrated as an example. One can clearly distinguish the ground state of  $^{16}O$  experimentally located at -8.1 MeV and a second peak distant about 6.3 MeV from the first, which represents the superposition of the excited  $0^+$ ,  $3^-$  and  $2^+$  states, as report in the NUDAT2 database [48]. In order to be separated, these states require a higher  $Q_{val}$  resolution than the one currently achieved. The Q-value spectrum presents also a continuous part, with a predicted  $Q_{val}$  threshold

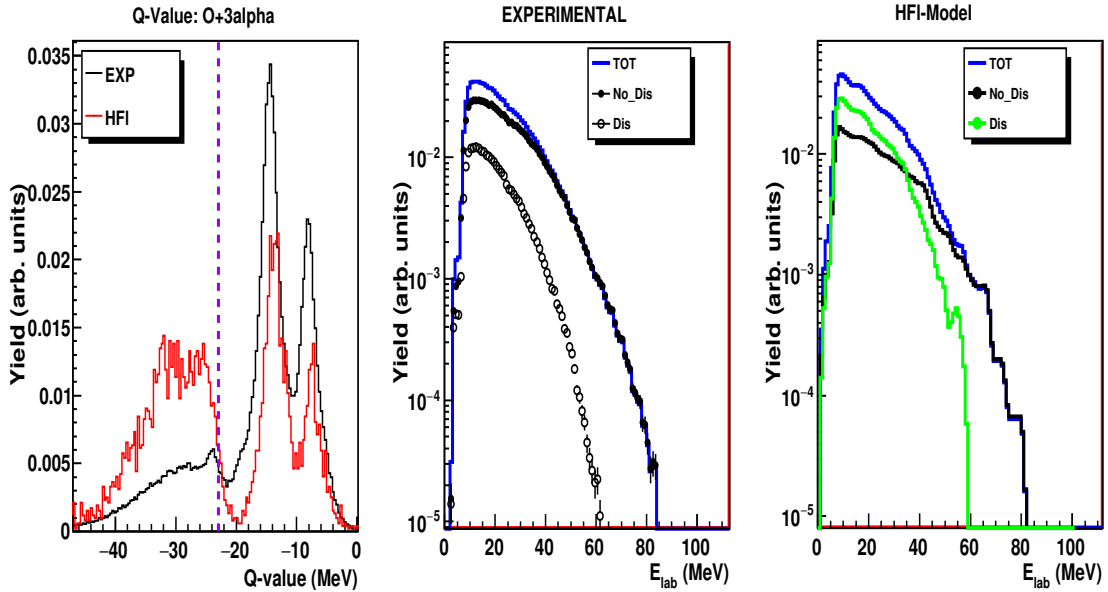


Figure 5.24: Q-value distribution for the  $^{16-xn}O+xn+3\alpha$  decay channel for 130 MeV (left panel). The black line corresponds to distributions obtained for the experimental data while the red one gives the HF $\ell$  predictions. In the middle and right panel the experimental and HF $\ell$  alpha particle energy distributions, shown with the relative contribution given by the less dissipative (No-Dis) and dissipative (Dis) events distinction (dashed purple line), are represented. The Q-value distribution is normalized to unitary area while the other two are normalized to the number of events.

of -22.9 MeV, which corresponds to the previously mentioned emission of neutrons. In the middle and right panel the total alpha particle energy distributions for this channel, are illustrated, separately for data and HF $\ell$  model, together with the contributions given by the less dissipative (No-Dis) and dissipative (Dis) events separation. As one expected from the Q-value, the HF $\ell$  model fails to reproduce the BR associated to these two type of decay modes with respect to the observed data which indicates a dominance of the less dissipative channels.

Due to the identification contamination between  $\alpha$ -particles and  ${}^3\text{He}$ , a spurious peak can be noticed in some of the distributions of Figure 5.22 and 5.23. For instance, this contamination is particularly evident in the  ${}^{20-xn}\text{Ne} + xn + 2\alpha$  channel around -20 MeV which from theoretical calculation corresponds to the Q-value (-19.4 MeV) of the actual  ${}^{21}\text{Ne} + {}^3\text{He} + \alpha$  channel. This means that some of the  ${}^3\text{He}$  is wrongly identified as an alpha particle and can worsen the Q-value resolution if one needs to do a precise study based on the excitation spectrum. In the future, this problem will be investigated in more detail.

Despite these limitations, the Q-value results extremely useful. In fact, referring back to the proton energy spectrum in Figure 5.14, 5.15 and 5.16 for the Aluminium case, we noticed a discrepancy between the data distributions and model predictions. If one takes a closer look to the Q-value spectrum, a possible explanation is given by the fact that the model seems to populate more the channels involving only one neutron emission while in the experimental data the two neutron channel prevails. Therefore, the deviations in the proton energy spectra can be due to the different weights of the decay channels with  $1n$  and  $2n$  in the experimental sample and model calculations.

Lastly, in Figure 5.25 we illustrate the excitation energy dependence of the previous Q-value distributions of Table 5.2. As one would expect, the higher excitation energy allows the opening of more dissipative channels with an increasing number of emitted neutrons. This behaviour is well illustrated for the previously described  $Al + xn + p$  case, where one can notice how the Q-value distributions changes its shape from a  $1n$  neutron emission ( $Q_{val} \leq -7.9$  MeV) to a dominant  $2n$  ( $Q_{val} \leq -19$  MeV) or more neutron emission.

### 5.3.3 Indication of clustering effects

The residue inclusive observables, presented in section 5.2, showed only small deviations from a statistical behaviour. However, the larger experimental branching Ratio in  $\alpha$ -particle decay channels for the even-Z residues is an indication of possible  $\alpha$ -structure correlations in the  ${}^{28}\text{Si}^*$  compound nucleus, as it was pointed out by [3] in a similar case. To better evidence possible alpha clustering effects, we introduce a new variable quantifying the experimental branching ratio excess from Table 5.2, with respect to the

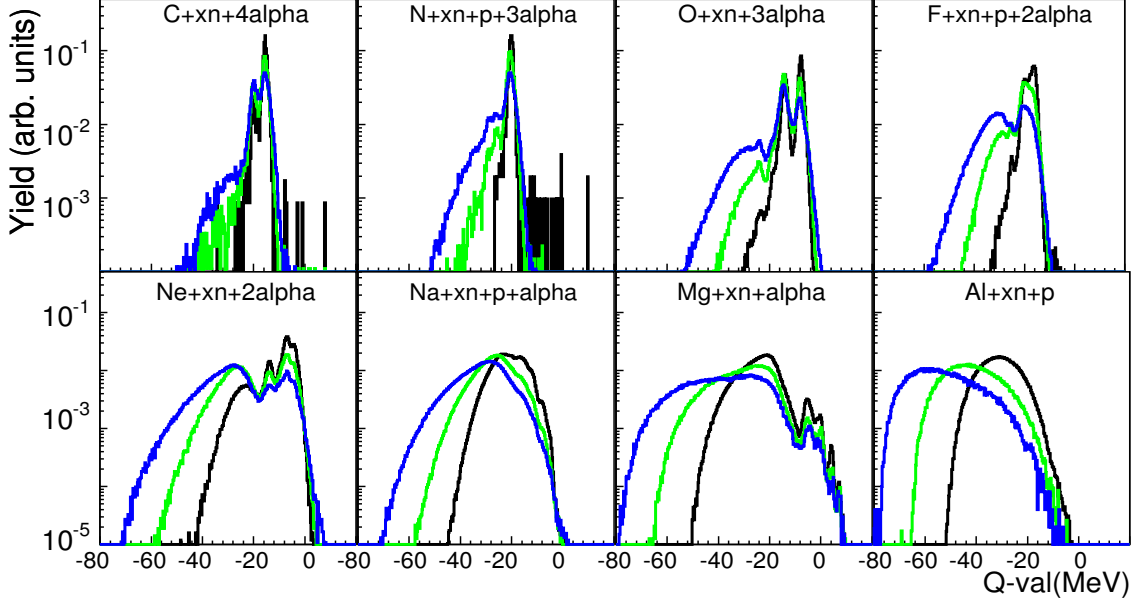


Figure 5.25: Q-value experimental distributions for the channels presented in Table 1.4 for 90.5 (black line), 110 (green line) and 130 (blu line) MeV. The distributions are normalized to unitary area.

HF $\ell$  model, for  $\alpha$  emission:

$$R_{clust}(Z) = \frac{Y_{exp}(Z; n_Z\alpha)}{Y_{exp}(Z)} - \frac{Y_{HF\ell}(Z; n_Z\alpha)}{Y_{HF\ell}(Z)} \quad (5.2)$$

where  $Y_{exp}(Z; n_Z\alpha)$  represents the number of events associated to the maximum  $\alpha$ -multiplicity for the residue of charge  $Z$  (channels illustrated in Table 5.2).  $Y(Z)$  is the total yield of the channels for the residue of charge  $Z$  with respect to which the BR is calculated. In Figure 5.26, the quantity of eq. 5.2, indicating the extra probability of alpha emission is plotted for all three energies of the reaction, giving a visual representation of the results summerised in Table 5.2. One can notice that the evaporation chains leading to even- $Z$  residues show, from an experimental point of view, a preferential  $\alpha$  decay. This excess may be interpreted as an evidence of effects related to the residual  $\alpha$  structure correlations in the  $^{28}\text{Si}$  or in its  $^{24}\text{Mg}$  daughter nucleus. The  $\alpha$  clustering in this latter nucleus was studied and proved in great detail by the previous experiments of the NUCL-EX collaboration [3].

Regarding the odd- $Z$  residues, only the  $Z_{big}=11$  shows an abnormal behaviour for 130 MeV which deviates from the expected and predicted one at lower energies. Therefore, further investigations are needed for this specific channel.

Since we measured the reaction at three different beam energies, we can also study the dependence of the branching ratio excess on the excitation energy. As one can

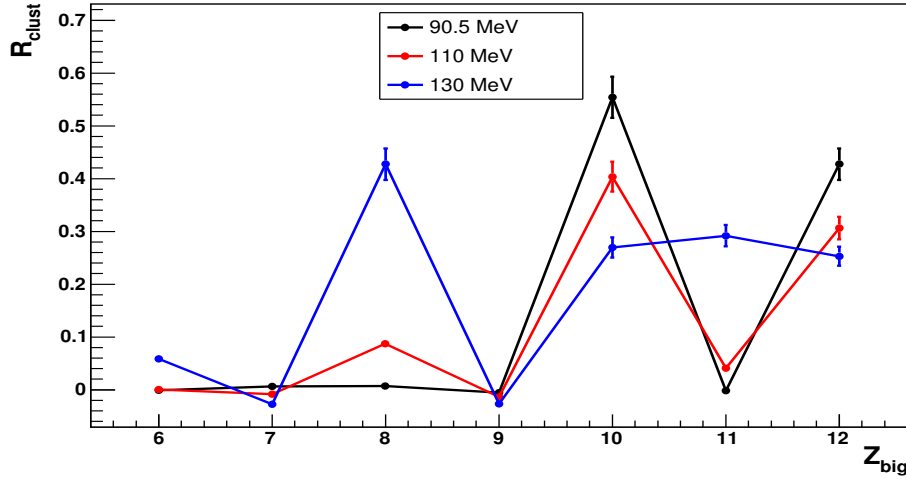


Figure 5.26: Branching ratio excess for  $\alpha$  particles decay as a function of the charge of the final residue. The different colored lines represent the three energies of the reaction, as illustrated in the legend.

notice from Figure 5.26 and from Table 5.2, the Oxygen exhibits a different dependence with respect to the other two even- $Z$  residues. Indeed, as the energy increases the BR excess seems to increase as well, while for the Neon and Magnesium the opposite behaviour is observed. This can indicate that the clustering properties of the  $^{28}\text{Si}$  vary with the excitation energy. In particular, larger mass clusters seem to be present at low energies with increasing importance of smaller clusters like  $^{16}\text{O}$  with increasing energies. This hypothesis will require a more detailed characterization using kinematic and Jacobi energy-angular correlations as it was done in the past for the  $^{12}\text{C} + ^{12}\text{C}$  reaction [3].

# Conclusions and Perspectives

This thesis has been devoted to a first preliminary study of the  $^{16}\text{O}+^{12}\text{C}$  reaction performed at three different incident energies, namely 90.5, 110 and 130 MeV. The goal was to highlight possible cluster effects in the  $^{28}\text{Si}$ , formed in the case of a complete fusion between the reaction partners, by comparing the obtained results with a statistical decay code. The  $^{16}\text{O}+^{12}\text{C}$  reaction is part of an experimental campaign started by the NUCL-EX collaboration which regards the investigation of light nuclear systems with  $A < 40$ . For this purpose, a very detailed Hauser-Feshbach statistical decay Monte-Carlo was developed by the collaboration with the intent of reproducing at best the experimental data for fusion-evaporation reactions. In fact, the model compared to other event simulation such as GEMIN++ [53] includes also discrete energy levels which can be populated in the last stages of the decays. The only free parameter of this model was highly constrained by the results of previous experiments.

The first part of this work was mainly focused on preliminary operations such as energy calibration of the experimental apparatus and identification of the incident particles. The latter were detected by coupling two detectors (GARFIELD and Ring Counter), installed at the Legnaro National Laboratories of INFN. This apparatus is particularly suited for measuring nuclear reactions at the low and intermediate energies due to its low detection thresholds and high geometrical efficiency, as described in Chapter 2. With this detector, charged particles can be identified both in charge and mass by using the  $\Delta E - E$  correlations and the Pulse Shape Analysis (PSA) technique.

As far as the analysis is concerned, a first selection of the experimental data was done by selecting the reaction mechanism from the total detected charge *vs* total longitudinal detected momentum correlation. Two different cuts have been employed. In the first case, a loose condition on the aforementioned correlation has been imposed. In this way, the reaction mechanism could be checked to correspond to mainly fusion-evaporation ones. In particular, the charge, energy and angular distribution have been investigated. In the second case, we required the complete detection of the charge in the entrance channel ( $Z_{tot}=14$ ) and a more stringent condition on the momentum as well. Global inclusive observables (energy and charge distribution) were compared for the two selections. The results indicated only small variations mainly due to the removing of contamination from peripheral reactions. Therefore, the experimental data with the latter cut could be

used for a more exclusive analysis since our selection did not bias the characteristics of the selected events but just reduced the available statistics. The previous analysis was conducted in the same way on all the three incident energies and the considerations are referred to all energies.

With the complete charge detection condition, we proceeded in studying the reaction by operating a selection of the decay channels based on the evaporation residue (ER) detected at the end of a decay chain. The comparison with the HF $\ell$  can indicate if the presence of cluster effects are evidenced already at this point. For this purpose, the energy distribution of the detected ER and the energy and angular distributions of the protons and  $\alpha$ -particles detected in coincidence with the former, were plotted for the three incident energies. We noticed that generally the distributions of protons were well described by the HF $\ell$  predictions with the exception of the Aluminium ( $Z_{big}=13$ ) case. On the other hand, the distributions of alpha particles showed some clear discrepancies in coincidence with particular even- $Z$  residues, namely  $Z_{big}=10$  (Neon) and  $Z_{big}=12$  (Magnesium). Similarly, also the energy distribution of the ER for the same  $Z_{big}$  values showed a disagreement between the data and the model calculations. Moreover, the differences seemed to become more obvious as the excitation energy of the system increased. Since these distributions represent the contribution of many possible decay channels of the same ER, in the next step of the analysis we focused on specific decay channels in order to understand the origin of the observed differences between the data and the model calculations.

Indeed, we selected the most probable decay channel in the experimental sample for the considered ERs and the Branching Ratio (BR) of these channels were calculated for both experimental and simulated data for the three energies. A first observation was that these most probable channels turned out to be the ones which involve the highest number of  $\alpha$ -particles with the obvious exception of  $Z_{big}=13$ . The comparison with the model has evidenced that the HF $\ell$  underestimates the experimental BR, in particular for even- $Z$  residues. These differences were then used to explain the previous disagreements. In fact, we compared the  $^{20-xn}\text{Ne}+xn+2\alpha$  experimental energy distribution of the alpha particles with the HF $\ell$  predictions and noticed that these showed a good agreement. This meant that the kinematics of the reaction is well described by a fusion-evaporation model if one selects specific decay channels. Therefore, we concluded that the differences in the inclusive distributions were due to the different evaluation of the BR by the experimental data and by the model predictions.

The exclusive decay channels were also studied using a Q-value like variable reconstructed from the kinetic energy of the detected particles. The Q-value distribution allowed us to separate, for the most probable channels, the more dissipative events involving neutrons from the less dissipative events without the emission of neutrons. This selection, made possible the interpretation of the results observed for the Aluminium case. Indeed the differences in the shape of the proton spectra, at the three incident energies, were determined by the different population of the multiple neutron channels

by the HF $\ell$  model and experimental data, respectively. Lastly, we introduced a visual representation of the BR excess in the data sample with respect to the model predictions. In this way, the indication of possible alpha structure correlations was made more obvious and also the dependence with the excitation energy was highlighted.

The results described in these conclusions indicate that nuclear structure effects, in particular  $\alpha$ -clustering, may persist even at high excitation energy (for this reaction: 55, 63 and 72 MeV) in the  $^{28}\text{Si}$  formed in the case of a fusion reaction. To safely confirm this hypothesis, the collaboration will need to perform further detailed studies which mainly will involve the following points underlined by this thesis:

- Detailed studies based on particle correlation functions as shown in Chapter 4.
- Investigate a way to overcome the  $^3\text{He}$  contamination.
- Further studies for  $^{23-xn}\text{Na}+x\text{n}+\text{p}+\alpha$  channel at 130 MeV, which presents an abnormal BR excess with respect to the other odd-Z residues and its previous energy cases.
- Estimation of cross-sections of the different observed reaction channels, including the total cross-section for the formation and decay of an equilibrated source.
- Investigate if other observables can better describe the energy dependence of the cluster effects.
- Comparison with models including deformation of the  $^{28}\text{Si}$  system.

Another possible interesting topic is represented by the study of the Oxygen projectile excited in peripheral collisions as briefly illustrated in Chapter 1. In fact, one of the excited states of  $^{16}\text{O}$  nucleus is supposed to be similar to the Hoyle state for the  $^{12}\text{C}$ . This state should be at 14.4 MeV, located above the  $4\alpha$  decay threshold. Therefore, the investigation and precise characterization of this state is important.



# Bibliography

- [1] NUCL-EX Collaboration INFN: [www.bo.infn.it/nucle-ex/](http://www.bo.infn.it/nucle-ex/)
- [2] G. Baiocco, **PhD Thesis: Towards a reconstruction of thermal properties of light nuclei from fusion-evaporation reaction**, University of Bologna (2010).
- [3] L. Morelli *et. al.*, **J. Phys. G: Nucl. Part. Phys.** **41**, **075107** (2014).  
L. Morelli *et. al.*, **J. Phys. G: Nucl. Part. Phys.** **41**, **075108** (2014).
- [4] K. Adler *et. al.*, **Coulomb Excitation** , Academic Press, New York (1966).
- [5] C. Manaiescu, **Romanian Reports in Phys. Vol 68 No. 1, 169-176** (2016).
- [6] D. Durand E. Suraud and B. Tamain, **Nuclear Dynamics in the Nucleonic Regime**, ed. IoP, London (2001).
- [7] N. Bohr, **Nature** **137**, **344** (1936).
- [8] P. Fröbrich and L.Lipperheide, **Theory of Nuclear Reaction**, ed. Oxford Science Publications (1996).
- [9] H.A. Bethe, **Revs. Mod. Physc.** **2**, **72** (1937).
- [10] V.F. Weisskopf *et. al.*, **Phys. Rev.** **57**, **472** (1940).
- [11] L. Wolfenstein *et. al.*, **Phys. Rev.** **82**, **690** (1951).
- [12] W. Hauser *et. al.*, **Phys. Rev.** **87**, **366** (1952).
- [13] K.S. Krane, **Introductory nuclear physics**, ed. John Wiley and Sons (1988).
- [14] C. Beck, **Clusters in Nuclei, Vol.1** , ed. Springer Verlag Berlin Heidelberg (2010).
- [15] C. Beck, **Clusters in Nuclei, Vol.2** , ed. Springer Verlag Berlin Heidelberg (2012).
- [16] C. Beck, **Clusters in Nuclei, Vol.3** , ed. Springer Verlag Berlin Heidelberg (2013).
- [17] M. Brenner, **Cluster Structure of Atomic Nuclei**, ed. Research Signpost (2010).

- [18] W. Greiner *et. al.*, **Nuclear Molecules**, ed. World Scientific (1995).
- [19] W. Catford, **Clustering in Nuclei from N/Z=1 to N/Z=2**, arXiv:1302.3849 (2013).
- [20] H. Horiuchi and K. Ikeda, **Prog. Theor. Phys.** **40**, **277** (1968).
- [21] W. von Oertzen, **Eur. Phys. J A** **11**, **403** (2001).
- [22] F. Hoyle, **Astrophys. J. Suppl. Ser.** **1**, **12** (1954).
- [23] H. Morinaga, **Phys. Rev.** **101**, **254** (1956).
- [24] A. Tohsaki *et. al.*, **Phys. Rev. Lett.** **87**, **192501** (2001).
- [25] Ad.R. Raduta *et. al.*, **Phys. Lett. B** **705**, **65** (2011).
- [26] L. Morelli *et. al.*, **J. Phys. G: Nucl. Part. Phys.** **43**, **045110** (2016).
- [27] M. Freer *et. al.*, **Phys. Rev. C** **85**, **0376603** (1994).
- [28] T. K. Rana *et. al.*, **Phys. Rev. C** **88**, **021601** (2013).
- [29] P. Chevalier *et. al.*, **Phys. Rev.** **160**, **827** (1967).
- [30] M. Freer *et. al.*, **Phys. Rev. C** **51**, **1682** (1995).
- [31] N. Curtis *et. al.*, **Phys. Rev. C** **88**, **064309** (2013).
- [32] Y. Funaki *et. al.*, **Journal of Phys.: Conference Series** **436**, **012004** (2013).
- [33] J. Vadas *et. al.*, arXiv:1508.07824v1 (2015).
- [34] M. Bruno *et. al.*, **Eur. Phys. J.A** **49**, **128** (2013).
- [35] FAZIA Collaboration: *fazia.in2p3.fr*
- [36] L. Morelli, **PhD Thesis: Competition between evaporation and fragmentation in nuclear reaction at 15-20MeV AMeV energy**, pag. **36** (2011).
- [37] N. Le Neindre *et. al.*, **Nucl. Instr. and Meth. A** **701**, **145** (2013).
- [38] G. Pasquali *et. al.*, **Nucl. Instr. and Meth. A** **570**, **126** (2007).
- [39] L. Bardelli, **A ROOT-based data-monitor software for the GARFIELD experiment**, LNL Ann. Report (2007).

- [40] G. F. Knoll, **Radiation Detection and measurements**, ed. John Wiley and Sons, New York (1989).
- [41] N. Le Neindre *et. al.*, **Nucl. Instr. and Meth. A** **490**, **251** (2002).
- [42] L. Morelli *et. al.*, **Nucl. Instr. and Meth. A** **620**, **305** (2010).
- [43] ROOT Data Analysis Framework: *root.cern.ch*
- [44] V. Avdeichikov *et. al.*, **Nucl. Instr. and Meth. A** **501**, **505** (2003).
- [45] A. Boschi, **Bachelor Thesis: Misure di reazioni di fusione-evaporazione  $^{16}\text{O} + ^{12}\text{C}$ . Risultati Preliminari**, University of Bologna (2016).
- [46] Z. Chen and C.K. Gelbke, **Phys. Rev. C** **38**, **2630** (1988).
- [47] The AME2012 Atomic Mass Evaluation: *www.nndc.bnl.gov/masses/*
- [48] NUDAT2 online database *www.nndc.bnl.gov/nudat2/*
- [49] T. Von Egidy and D. Bucurescu, **Phys. Rev. C** **72**, **044311** (2005).  
T. Von Egidy and D. Bucurescu, **Phys. Rev. C** **73**, **049901** (2006).
- [50] A. V. Ignatyuk *et. al.*, **Sov. J. Nucl. Phys.** **21**, **255** (1975).
- [51] J. Töke and W. J. Swiatecki, **Nucl. Phys. A** **372**, **141** (1981).
- [52] M. V. Ricciardi *et. al.*, **Nucl. Phys. A** **733**, **299** (2004).
- [53] R. J. Charity, **Phys. Rev. C** **82**, **014610** (2010).
- [54] J. Pochodzalla *et. al.*, **Phys. Rev. C** **35**, **1695** (1987).
- [55] O. B. Tarasov and D. Bazin, **NIM B204**, **174-178** (2003).
- [56] R. Bass, **Nucl. Phys. A** **231**, **45** (1974).
- [57] A. Camaiani, **Master Thesis: Study and decays reconstruction of  $^{25}$  system formed in  $^{12}\text{C} + ^{13}\text{C}$  reaction at 95 MeV as a way to highlight possible structural effects**, University of Florence (2016).